Transient Analysis of an Air-conditioning System for Electric Vehicles Using Carbon Dioxide

高, 在德

Transient Analysis of an Air-conditioning System for Electric Vehicles Using Carbon Dioxide

September, 2021

Department of Energy and Environmental Engineering
Interdisciplinary Graduate School of Engineering Sciences
Kyushu University

Jaedeok Ko

Transient Analysis of an Air-conditioning System for Electric Vehicles Using Carbon Dioxide

By
Jaedeok Ko

Dissertation submitted to the Interdisciplinary Graduate School of Engineering Sciences of Kyushu University in partial fulfillment of the requirements for the degree of Doctor of Philosophy in Engineering

2021

Committee

Prof. Takahiko Miyazaki, Chair

Assoc. Prof. Kyaw Thu

Assoc. Prof. Keishi Kariya

Declaration

I declare that this dissertation was composed by myself, that the work contained herein is my own except where explicitly stated otherwise in the text, and that this work has not been submitted for any other degree or professional qualification except as specified. Parts of this work were published as follows:

Ko, J., Takata, N., Thu, K., & Miyazaki, T. (2020). Dynamic modeling and validation of a carbon dioxide heat pump system. *Evergreen*, *7*(2), 172-194.

Ko, J., Thu, K., & Miyazaki, T. (2021a). Investigation of a cascaded CO_2 refrigeration system using phase change materials for energy-saving potentials. *Applied Thermal Engineering*, *182*, Article 116104.

Ko, J., Thu, K., & Miyazaki, T. (2021b). Transient analysis of an electric vehicle air-conditioning system using CO_2 for start-up and cabin pull-down operations. *Applied Thermal Engineering*, *190*, Article 116825.

This dissertation has been reorganized using the contents of the publications listed above as it is, and in this regard, the author states as follows:

- The fourth, eighth, and ninth paragraphs of Chapter 1, almost all text in Section 2.1.2 and 2.2, all text in Section 3.1, 3.2, and 3.3, the second paragraph of Chapter 4, the appendix B, and the appendix C are from Ko et al. (2021b).
- The tenth paragraph of Chapter 1, almost all text in Section 2.1.1, and the appendix A are from Ko et al. (2020).
- Some parts in Section 2.1.1 are from Ko et al. (2021a).

Except for that, other contents were not published in any other journals nor conferences.

Jaedeok Ko

March 2021

Abstract

This work addresses a transient analysis of an air-conditioning system (AC) for electric vehicles. The entire AC model consisting of a vapor compression system, an air handling unit, and a cabin was established using commercial software which offers acausal, equation-based, and object-oriented modeling approaches. R-744, one of the environmental-friendly refrigerants, was selected for the working medium. The model was validated by the in-house experimental data set and three different research articles. Validation results showed that the model predicts an actual system operation and performance adequately and demonstrates reliability. Transient characteristics and performance of an AC for electric vehicles were investigated using the model in various operating conditions. The results provide dynamic behavior of the AC according to operating parameters and performance comprehensively.

In this investigation, it is observed that the AC consumes tremendous energy during the start-up and cabin pull-down operation to achieve a target cabin temperature, and the coefficient of performance (COP) degrades during that period. The outdoor and indoor thermal conditions influence the energy consumption and pull-down time in the order of initial cabin temperature, cabin target temperature, number of occupants, initial cabin relative humidity, and solar irradiance. Concerning ventilation operation, intake of relatively high-temperature and high-humidity outdoor air results in a cooling load increase; thus, the compressor consumes more energy. Also, an increase in air temperature supplying to the cabin increases the cooling load on AC, under the same cabin set temperature.

The effect of system operating parameters on the COP was also investigated. The results showed that heat rejection pressure and refrigerant temperature at the main gas cooler's outlet affect the COP markedly. The optimum heat rejection pressure ensuring the maximum COP was clearly observed, and the results are well-matched with the model in the literature. The optimum heat rejection pressure highly depends on the refrigerant temperature at the outdoor heat exchanger (OHX) outlet while the evaporator operating condition has a relatively tiny effect on the optimum heat rejection pressure. The COP of the AC controlled for optimal heat removal pressure was compared to the COP of the AC otherwise. The comparison results showed that the COP operating under control is superior to that without control.

Considering that the average duration of a single driving for business and personal is about

30 minutes, the average operation time of the automobile AC is less than 30 minutes; meanwhile, it is known that electric vehicles suffer energy shortage, so have relatively shorter mileage than conventional vehicles. Given those, therefore, the amount of energy consumption in the start-up and pull-down period is worth considering in the preliminary designing phase for an electric vehicle AC. Also, a proper control strategy to the heat rejection pressure can improve the COP of an R-744 AC, significantly. It is expected that an electric vehicle can achieve additional energy-saving potential with real-time control on heat rejection pressure, thereby it can secure further mileage.

Table of Contents

List of Tables

List of Figures

Nomenclature

A	heat transfer area, m^2
A_c	cross-sectional area, m^2
C	coefficient
C_D	flow coefficient of a valve
C_P	specific heat at constant pressure, kJ kg^{-1} K^{-1}
D_h	hydraulic diameter, m
f_D	Darcy friction factor
G	mass flux, kg m^{-2} s^{-1}
G_s	Solar irradiation, W m^{-2} K^{-1}
g	gravitational acceleration, m s^{-2}
h	heat transfer coefficient, W m^{-2} K^{-1}
h^*	specific enthalpy, kJ kg^{-1}
Δh^*_{vap}	specific enthalpy of vaporization of water, kJ kg^{-1}
j	Colburn j-factor
k	thermal conductivity, W m^{-1} K^{-1}
$\dot{m}$	mass flow rate, kg s^{-1}
N_{occ}	the number of occupants
N_{res}	respiratory rate per second, s^{-1}
Nu	Nusselt number
P	pressure, MPa
p_l	louver pitch, m
Pr	Prandtl number
$\dot{Q}$	heat transfer rate, W
Re	Reynolds number
s	specific entropy, kJ kg^{-1} K^{-1}
S_{comp}	compressor rotational speed, rev s^{-1}
T	temperature, K or ^oC
ΔT_{sup}	degree of suction superheating, K or ^oC
t	time, second
$t_{pull-down}$	pull-down time, second
$\bar{t}_{pull-down}$	normalized pull-down time

th	thickness, m
U	uncertainty
u	specific internal energy, kJ kg^{-1}
$\bar{u}$	normalized specific internal energy
$\dot{V}$	volumetric flow rate, m^3 s^{-1}
v	specific volume, m^3 kg^{-1}
V_{cabin}	cabin volume, m^3
V_{comp}	compressor swept volume, m^3
V_{core}	the core volume of an air-to-refrigerant HX, m^3
V_s	segment volume, m^3
V_{tidal}	tidal volume, m^3
$\dot{W}$	power, W
$\bar{W}$	normalized energy consumption
x	vapor quality
x^+	mass fraction of a component based on moist-air mass
z	length, m

Greek letters

α	void fraction
α^*	absorptivity
Δ	difference
ε^*	emissivity
ζ	property
η	efficiency
ρ	density, kg m^{-3}
σ_{SB}	Stefan-Boltzmann constant, 5.67×10^{-8} W m^{-2} K^{-4}
τ	transmissivity
τ_{con}	condensation time constant, s
Ψ	reduced data
ψ	measured data
ω	humidity ratio, kg kg^{-1}

Subscripts

1	single-phase
2	two-phase
a	dry air
abs	absorption
$body$	vehicle body
c	cooling
cen	center
ch	channel
$co2$	carbon dioxide in exhaled air
con	condensation
$cond$	conduction
$conv$	convection
emi	emission
$evap$	evaporator
ex	expansion valve
exh	exhaled
ext	exterior
fan	fan
fin	fin
gc	gas cooler
gen	generation
h	heating
i	inlet
in	inner surface
inh	inner half
ins	insulation
L	saturated liquid
lam	laminar flow
lat	latent
m	moisture
ma	moist-air
max	maximum
min	minimum

o	outlet
od	outdoor
opt	optimum
ori	orifice
out	outer surface
$outh$	outer half
r	roof
ref	refrigerant
rw	rear window
s	isentropic
sen	sensible
sw	side-windows
tur	turbulent flow
V	saturated vapor
v	volumetric
w	water
$wall$	channel wall
win	window
ws	windshield

Abbreviations

AC	air-conditioning system
AHU	air handling unit
EEV	electric expansion valve
HX	heat exchanger
IHX	indoor heat exchanger
IntHX	internal heat exchanger
OHX	outdoor heat exchanger
R-744	carbon dioxide
RH	relative humidity
VCS	vapor compression system

Chapter 1 Introduction

The number of electric vehicles[1] has been increasing in the last decade (IEA, 2020). The performance of such vehicles highly depends on the equipped battery performance; therefore, the fundamental challenge in electric vehicles is to find out suitable and sustainable material for the battery that can provide long mileage and fast charging (Budde-Meiwes et al., 2013; Dunn et al., 2011; Lukic et al., 2008). Rechargeable lithium-ion batteries are regarded as the proper material since they have a higher energy density, higher specific power, lighter weight, lower self-discharge rates, higher recyclability, and longer cycle life than other rechargeable batteries[2] (Bukhari et al., 2015; Lowe et al., 2010; Tarascon & Armand, 2011). Besides, lithium-ion batteries do not accompany the memory effect[3] (Etacheri et al., 2011; Sasaki et al., 2013). However, the critical problem of lithium-ion batteries is their performance, lifetime, and safety depend on the surrounding thermal environment (Bandhauer et al., 2011) so, they should be within a suitable operating temperature range[4] at all time (Persaran, 2001, 2002; Pesaran et al., 2013). While conventional vehicles[5] consume most fuel energy for driving, engine cooling, and managing thermal comfort in the cabin, electric vehicles consume additional energy to manage the battery temperature. Thus, the usable energy for driving decreases, consequently, the mileage shortens. Electric vehicles should save overall energy consumption to take reliability on a certain level of mileage. For that, they need an air-conditioning system (AC) with high efficiency and sophisticated control functions.

Vapor compression systems (VCSs) have been used as a subsystem of an AC in conventional vehicles for a long time, and they are still prevailing for electric vehicles since the related industry desires a direct transition from conventional vehicles to electric vehicles considering convenient replacement, low cost, and easy maintenance (Qi, 2014). Figure 1.1 shows a schematic of an AC used in conventional vehicles, consisting of a VCS and an air handling unit (AHU). The VCS consists of a compressor, an expansion device, and two heat exchangers (HXs): an evaporator, and an outdoor heat exchanger (OHX). In the evaporator,

[1] Electric vehicles herein mean battery electric vehicles only.
[2] Lead-acid, nickel-cadmium, and nickel-metal hydride batteries
[3] The phenomenon is that batteries gradually lose their maximum energy capacity if they are repeatedly recharged after being partially discharged.
[4] 15 °C to 35 °C
[5] Internal combustion engine-driven vehicle

heat transfers from the air to the refrigerant, and in the OHX, vice versa. In the compressor, refrigerant vapor with low-temperature and low-pressure is compressed to become high-temperature and high-pressure vapor, and it flows into the OHX. In the OHX, the refrigerant cools down into a low-temperature refrigerant by rejecting its heat to the outdoor airflow. The refrigerant then flows into the expansion device and becomes a low-temperature and low-pressure refrigerant by expansion process; then it enters the evaporator. The refrigerant in the evaporator absorbs heat from the airflow then flows into the compressor again. In the AHU, return air, fresh air, or mixed air passes through the evaporator core volume and cools down; in this process, moisture in the air is condensed depending on operating conditions. This low-temperature air leaves the evaporator, and then it directly flows into the cabin. Alternatively, part of that leaving air flows into the electric heater[6] and undergoes reheating, then supplies to the cabin blending with the cool air.

[6] Positive temperature coefficient (PTC) heater

Figure 1.1. Schematic of an automobile AC.

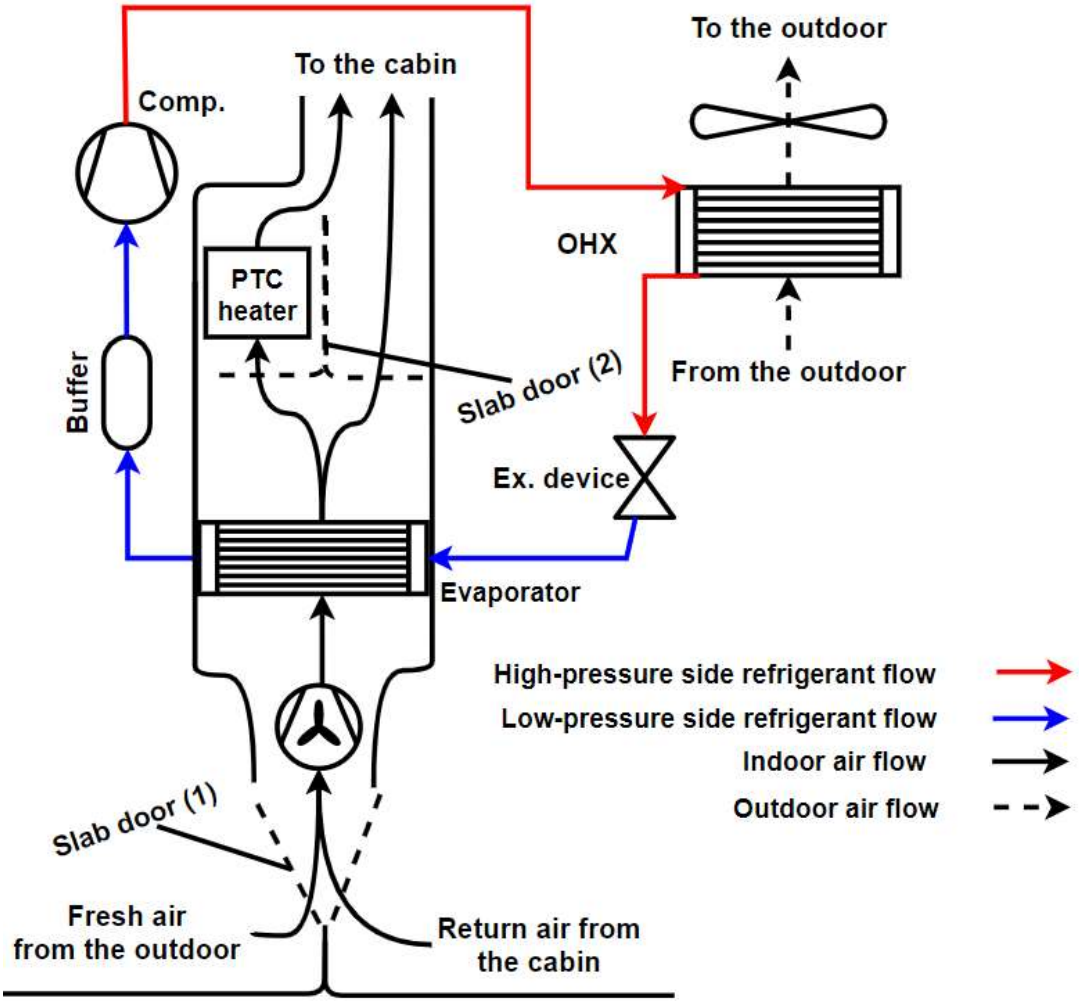

AC of electric vehicles has almost the same configuration as AC in conventional vehicles, except for the compressor. Conventional vehicles adopt a belt-driven compressor that connects with the crank pulley of the internal combustion engine by a belt so, the compressor rotational speed depends on the engine stroke. The compressor cannot change its rotational speed to respond to a partial cooling load change. Thus a variable-displacement compressor has been used in most cases. On the other hand, electric vehicles use an electrical-driven compressor with an independent power source, batteries. Hence it can respond to a partial cooling load change by adjusting the rotational speed. The variable-displacement compressor is not essential in this case, so a fixed-displacement compressor is typically used. Those characteristics of electric compressors have the advantages as follows: Even when vehicles are stopped or running at a low speed, the compressor rotational speed can be adjusted according to the cooling load to secure a comfortable indoor thermal environment by providing rapid cooling capacity responses. Besides, electrical-driven compressors are more comfortable to design because they are relatively free to positioning in the hood. Also, there is no mechanically moving part of receiving power from the electric motor, so they have superior airtightness (Ap et al., 2000; Makino et al., 2003).

The operating condition of automobile ACs differs from residential ACs; outdoor climate and driving conditions significantly affect systems' behavior and performance. Thus, they are typically regarded as a transient system (Qi et al., 2007). Such AC is a considerably energy-consuming subsystem in vehicles; it consumes about 12-17% of a mid-size automobile's total energy consumption (Lambert & Jones, 2006). The importance of AC is emphasized in electric vehicles rather than conventional vehicles; since AC is the second most energy-consuming subsystem after the electric motor, a cooling operation for cabin thermal comfort can shorten the mileage by 35-50% (Farrington et al., 1999; Farrington & Rugh, 2000). Automobile ACs aim to achieve and manage the cabin thermal comfort to the setpoint level that occupants desire. During the cabin pull-down period, the energy consumption is rather significant in vehicles, especially when vehicles are parked under the sun in summer. In the pull-down phase, AC's cooling load is higher than that of the optimally designed capacity (Gado et al., 2008), and the compressor often consumes considerable energy to distribute the refrigerant into each HX (Peuker & Hrnjak, 2008). Hence, the coefficient of performance (COP) of AC during the start-up and pull-down operation is often low compared to the nominal COP (Gado et al., 2008). That initial load gradually decreases with time until the system reaches a steady-state. After the cabin temperature reaches the setpoint, the system operates to maintain indoor thermal comfort against thermal impacts.

Refrigerants for automotive ACs and their characteristics are summarized in Table 1.1. R-12[7] has been widely used since the 1930s. It has nontoxicity and superior thermodynamic characteristics, but because of the high ODP[8], it has been replaced with R-134a[9] from the early 1990s. R-134a has zero ODP; however, it has a high GWP[10]. In this regard, international society has continuously strengthened the relevant regulations[11], which has sparked competition for refrigerant manufacturers to develop alternative refrigerants to preoccupy the global refrigerant market. In this circumstance today, related industry regards R-152a[12], R-1234yf[13], and R-744[14] as promising alternative refrigerants (Lee & Hwang, 2019). R-152a, as an HFC[15]-type refrigerant, has a much higher GWP than the other two refrigerants, and it is a flammable matter. R-1234yf was developed to replace R-134a, and it has a much lower GWP value than the R-152a. Although the flammability level of R-1234yf is low enough to be used for automotive (Moforte & Caretto, 2009; Seybold et al., 2014), but it does not mean that R-1234yf can guarantee safety. R-744 started getting attention from the early 1990s when Lorentzen and Pettersen (1992) reported its possibility as an alternative refrigerant. R-744, as a natural refrigerant, is one of the environmental-friendly (ODP of 0 and GWP of 1) and a safe refrigerant (non-flammable matter).

---

[7] Dichlorodifluoromethane
[8] Ozone depletion potential, i.e., ODP
[9] 1,1,1,2-tetrafluoroethane
[10] Global warming potential for 100 years, i.e., GWP
[11] e.g. Montreal Protocol, Kyoto Protocol, Kigali Amendment, EU F-gas Regulation, and Significant New Alternatives Policy Regulations
[12] 1,1-difluoroethane
[13] 2,3,3,3-tetrafluoropropene
[14] Carbon dioxide
[15] Hydrofluorocarbon

Table 1.1. Characteristics of refrigerants.

Refrigerant	**R-12**	**R-134a**	**R-152a**	**R-1234yf**	**R-744**
Type	CFC	HFC	HFC	HFO [a]	Natural
Structure	CCl_2F_2	CH_2FCF_3	CF_3CHF_2	$CF_3CF=CH_2$	CO_2
ODP	1	0	0	0	0
GWP	10890	1430	140	4	1
Safety classification [b]	A1	A1	A2	A2L [c]	A1
Molecular mass, kg $kmol^{-1}$	120.91	102.03	66.05	114.04	44.01
Critical pressure, MPa	4.136	4.059	4.517	3.382	7.377
Critical temperature, ^oC	112.0	101.1	113.3	94.7	31.0
Normal boiling point, ^oC	-29.8	-26.1	-24.0	-29.5	-78.4
Latent heat [d], kJ kg^{-1}	152.8	198.6	307.1	163.3	230.9

[a] Hydrofluoroolefin

[b] ANSI/ASHRAE Standard 34

[c] ASHRAE classified the flammability of refrigerants into three groups, but later, 2L was additionally adopted with regard to if the maximum burning capacity of no more than 100 mm s^{-1} at 23 oC and 101.325 kPa; meanwhile, this measure was done with the purpose to approve R-1234yf use for automotive ACs (Lee & Hwang, 2019).

[d] at 0 ^oC saturation condition.

R- 744 has unique thermophysical characteristics. It has a much higher saturation pressure than the other refrigerants at a given temperature, as shown in Figure 1.2a; this implies that R-744 systems operate at higher pressure conditions than other systems. Also, R-744 has a larger vapor density than other refrigerants; this makes R-744 have a large volumetric cooling capacity, as shown in Figure 1.2b. Thus, R-744 enables building a smaller size system with the same cooling capacity as the systems operated by other refrigerants; this is a significant advantage regarding automotive applications. R-744 has a low critical temperature of 31 ^{o}C so, R-744 VCSs are operated by transcritical cycle in most cases. Figure 1.3 describes R-744 subcritical and transcritical cycles. The difference between the subcritical cycle and the transcritical cycle is the phenomenon that the refrigerant undergoes when it rejects the heat at an HX at the high-pressure side of a system. In the subcritical cycle (1-2-3-4), the high-temperature vapor phase refrigerant (2) flows into the HX and rejects the heat through condensation, and this HX is called a condenser. In the transcritical cycle (1-2'-3'-4), however, the high-temperature supercritical refrigerant (2') rejects the heat through gas cooling. In this case, the HX is regarded as a gas cooler, and the refrigerant's temperature and pressure are independent of each other during this process. Supercritical R-744 has superior thermophysical properties; however, the heat rejection rate is sensitive to the operating pressure and the second-side working medium's temperature (Kim et al., 2004). Besides, properties change near the pseudocritical line suddenly, as shown in Figure 1.4.

Figure 1.2. (a) pressure-temperature diagram and (b) volumetric cooling capacity.

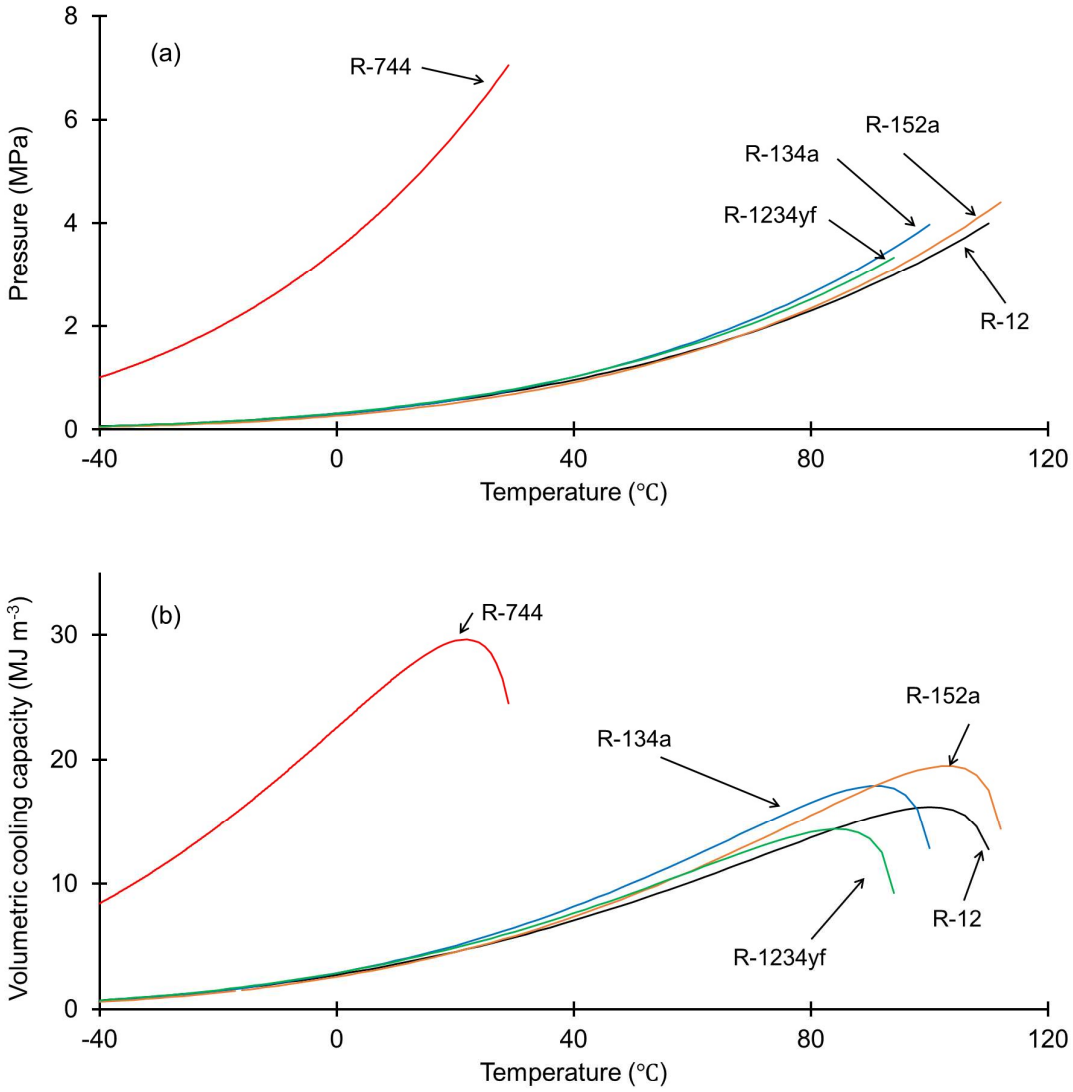

Figure 1.3. R-744 subcritical and transcritical cycles.

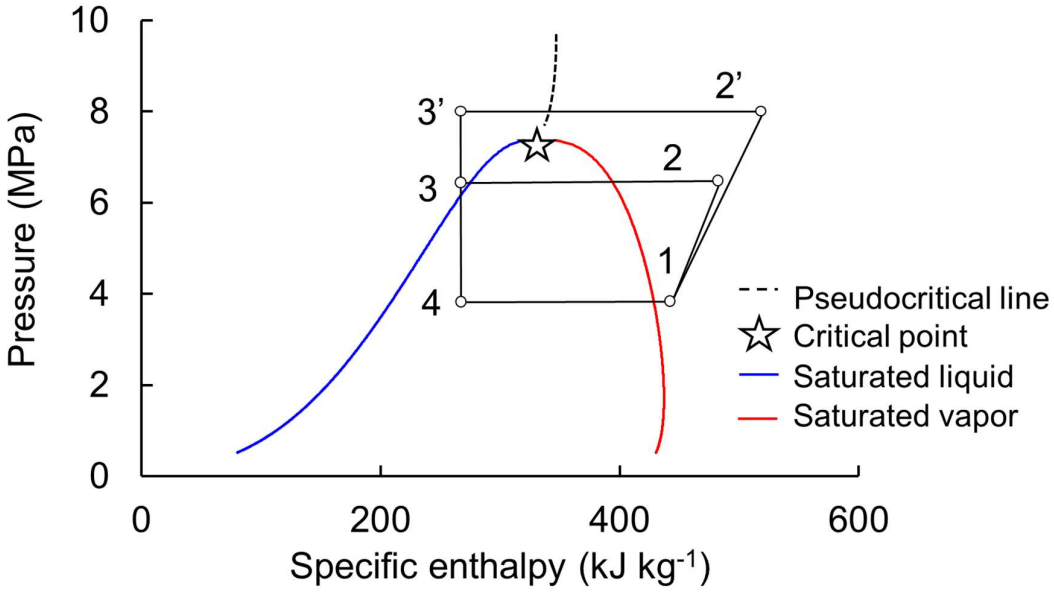

Figure 1.4. Properties of R-744 near pseudocritical line; (a) thermal conductivity, (b) density, (c) dynamic viscosity, (d) Prandtl number, and (e) specific heat.

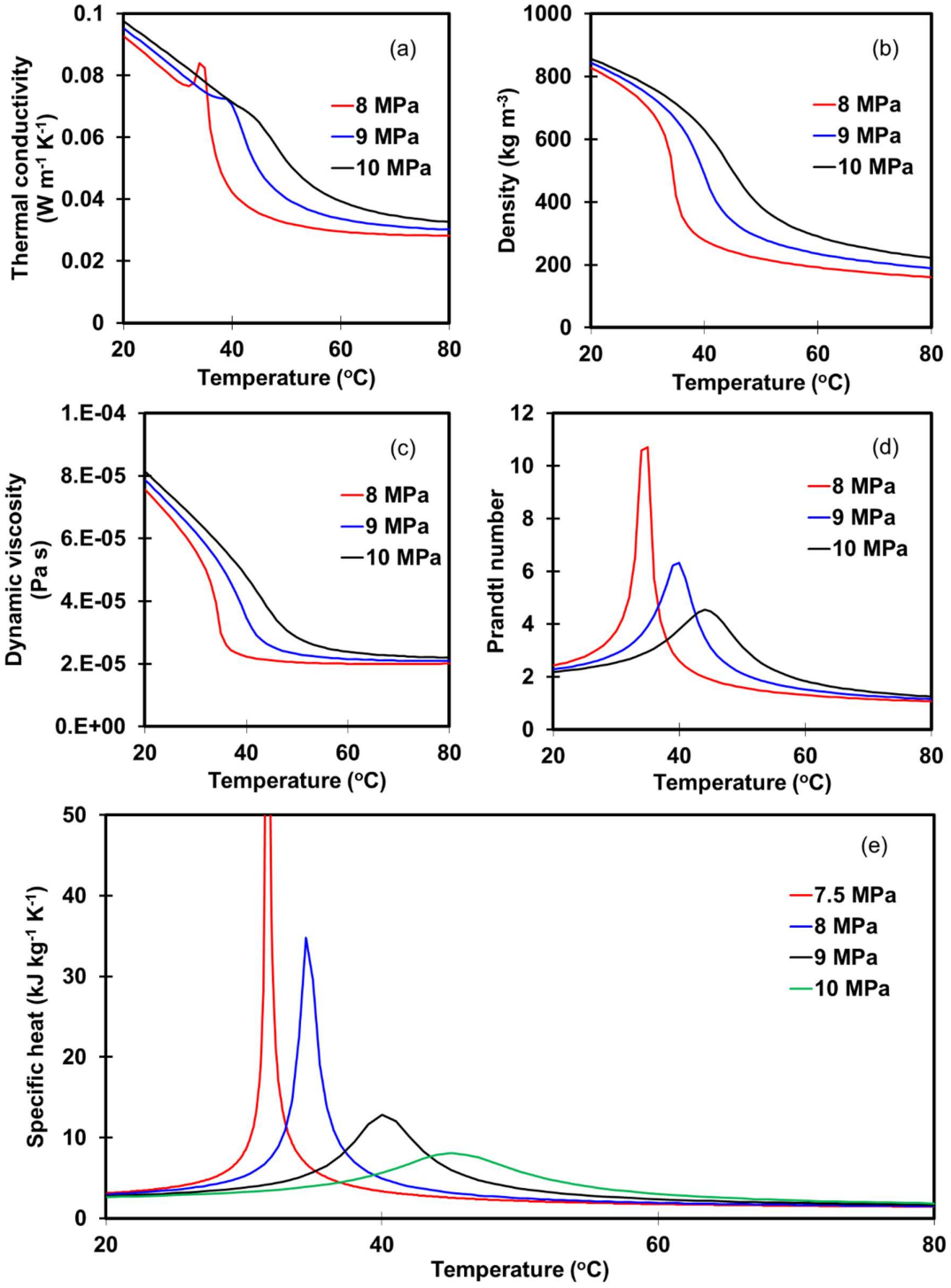

Engineers have studied R-744 ACs for many years considering the possibility of application to automotive. Table 1.2 summarizes previous studies on R-744 AC for conventional and electric vehicles. From the literature reviews, the followings can be derived:

- The cooling performance of R-744 systems is lower than that of conventional R-134a systems; however, it can be improved and reach a similar level to that of R-134a systems, utilizing IntHX and optimizing the components.
- Overall, R-744 systems provide superior heating performance than R-134a systems.
- The cooling and heating performance of R-744 systems can be improved by proper system layout involving adjacent devices that can play a role as a heat source or sink.
- In R-744 transcritical systems, heat rejection pressure and refrigerant temperature at the gas cooler outlet have a critical effect on the performance; a proper strategy is necessary to control the pressure during operation.

When it comes to heat rejection pressure, researchers investigated the optimum pressure for the maximum COP and provided correlations with related parameters (Chen & Gu, 2005; Kauf, 1999; Lioa et al., 2000; Sarkar et al., 2004). Cecchinato et al. (2010) evaluated the correlations in the four mentioned articles and revealed that the two correlations (Liao et al., 2000; Sarkar et al., 2004) which treat the gas cooler outlet temperature as an independent variable show a better precision than the other correlations (Chen & Gu, 2005; Kauf, 1999) which take the temperature of the gas cooler second-side medium as an independent variable. As another approach without using such correlations, Zhang and Zhang (2011) and Kim et al. (2014) proposed a real-time control method that compares system COP according to heat rejection pressure (i.e., gas cooler operating pressure) in real-time and yields the optimum operating pressure for the maximum COP. Also, Cecchinato et al. (2012) proposed a real-time algorithm using an artificial neural network. Those algorithm-based control methods have broad applicability, however, it is unavoidable that the control logic becomes complicated. A correlation-based control method requires lots of time and effort to obtain a correlation since many experimental data points need. Also, the limited range of applicability is another disadvantage of it. However, this approach ensures the reliability of control for a specific system.

Table 1.2. R-744 AC for conventional and electric vehicles.

Literature	Features
Lorentzen and Pettersen (1993); Pettersen (1994)	• R-744 system can be an alternative to R-12 system, but it requires a larger heat transfer area on the evaporator and gas cooler's airside than the R-12 system.
McEnaney et al. (1998)	• R-744 system can be a promising alternative to the R-134a system, but it has a 10% inferior COP in 54.4 ^{o}C outdoor temperature and 40% superior COP in the outdoor condition below 40 ^{o}C.
Boewe et al. (1999, 2001)	• An R-744 system with IntHX shows improved performance by up to 25% than an R-744 system without IntHX.
Brown et al. (2002)	• R-744 has better thermophysical properties in the gas cooling process than the R-134a condensation process, and the approach temperature of R-744 is lower than R-134a. • The isentropic efficiency of R-744 compression is lower than that of R-134a. • Under the same operating conditions, the COP of the R-744 system is 21% to 34% lower than that of the R-134a system. • In the same compressor rotational speed and the lower outdoor temperatures, the COP gap between the two systems decreases; however, the gap increases under higher rotational speed and outdoor temperatures. • If both systems use the same HX for the gas cooler (or condenser) and evaporator, the R-744 system has lower performance than the R-134a system, even though the R-744 system equips an IntHX.
Liu et al. (2005)	• The under-estimated charge causes low cooling capacity so that the COP is degraded whiles the over-estimated charge brings down the COP due to the over-loaded compression work. • The performance of a transcritical R-744 system highly depends on the high-pressure side's operating pressure; it is necessary to control for the pressure.

Table 1.2. continued.

Literature	Features
Kim et al. (2007a, 2007b)	• The arrangement of air-cooled HXs affects the performance of an R-744 system for electric vehicles; even the same arrangement can increase or decrease the performance depending on operating modes. • The heating capacity of the waste-heat recovery system increases by up to 100% than that of the system without recovery.
Wang et al. (2018a, 2018b, 2019)	• A dual-series of indoor gas coolers (IGCs) can improve the heating performance of an R-744 system. • Under cold climate conditions, the dual-series IGCs R-744 heat pump shows better performance than vapor injection heat pumps using conventional refrigerant. • R-744 systems can show better heating performance because R-744 rejects the heat by the gas cooling process with a large amount of temperature gliding.
Wang et al. (2021)	• R-744 system shows a superior heating performance than the R-134a system. • In cooling mode, the R-744 system can provide a similar COP performance compared to the R-134a system.
Dong et al. (2021)	• R-744 system provides a similar cooling capacity and COP with those of the R-134a system. • R-744 system shows a better heating capacity and COP than the R-134a system in cold outdoor conditions, from -10 ^{o}C to -25 ^{o}C.
Song et al. (2021)	• Experimental investigation on R-744 heat pump system for an electric bus • Comprehensive parameters' effects on the heating performance are provided with a new equation for the optimum heat rejection pressure.

Meanwhile, computer simulation is an effective way to understand a system's dynamic behavior and estimate energy consumption under a given operating condition, with a relatively cheap cost than experimental approaches. Most previous studies have developed transient models paying their attention to tracking refrigerant migration considering the system characteristics of start-up and pull-down operations (Hermes & Melo, 2008; Li & Alleyne, 2010; Li et al., 2011; Murphy & Goildschmidt, 1985; Rajendran & Pate, 1986). On the other hand, the investigation of the transient behavior and energy consumption of mobile AC should be carried out in the entire system integrated with the cabin (Li & Sun, 2013); this is because individual treatment for AC and cabin ignore the interactions between them and it is difficult to capture the dynamic response of the entire system to cooling demands that change over time. Table 1.3 shows recent studies on the transient modeling and simulations of AC and passenger cabin. The models presented in Khayyam et al. (2011a, 2011b, 2012) and Khayyam (2013) consider only the AHU and passenger cabin, while other studies (Marcos et al., 2014; Sanaye & Dehghandokht, 2011; Torregrosa-Jaime et al., 2015; Wu et al., 2017) treated the cabin only. In contrast, the three research articles (Gado, 2006; Kiss et al., 2013; Singh & Abbassi, 2018) consider the entire system, coupling with the cabin.

Humidity is the fundamental factor affecting thermal comfort in the cabin with air temperature (ASHRAE Handbook, 2001; Alahmer et al., 2011). Maintaining comfortable levels of dry-bulb temperature and relative humidity (RH) can improve occupants' thermal comfort (Olesen & Parsons, 2002). Also, rapid response and sophisticated control for AC against the air conditioning target space's RH and temperature provide energy-saving potential (Lim et al., 2018). Nevertheless, indoor air humidity has often been neglected in modeling, so latent heat load has not been considered for energy consumption estimation in most cases. The dehumidification process controls this indoor humidity at the evaporator during the cooling operation. When moist air passing through the evaporator, moisture condensation has a considerable effect on the temperature and RH of the moist air, leaving the evaporator (Kiss et al., 2013); then, this leaving air supplies to the cabin. Thereby, it significantly affects cabin humidity levels. Thus the moisture condensation should be considered for modeling (Kiss et al., 2013). However, models considering the latent heat load, the humidity of the indoor air, and the moisture condensation comprehensively are somewhat limited.

Table 1.3. Studies on modeling and simulations of automobile ACs and cabin (Ko et al., 2021b).

Reference	Coverage of modeling and simulations					
	A	**B**	**C**	**D**	**E**	**F**
Gado (2006)	Yes	Yes	Yes	Yes	Yes	Yes
Khayyam et al. (2011a)	No	Yes	Yes	No	Yes	No
Khayyam et al. (2011b)	No	Yes	Yes	No	Yes	No
Khayyam et al. (2012)	No	Yes	Yes	No	Yes	No
Khayyam (2013)	No	Yes	Yes	No	Yes	No
Marcos et al. (2014)	No	No	Yes	No	No	No
Kiss et al. (2013)	Yes	Yes	Yes	Yes	Yes	Yes
Sanaye and Dehghandokht (2011)	No	No	Yes	Yes	Yes	No
Torregrosa-Jaime et al. (2015)	No	No	Yes	Yes	Yes	No
Wu et al. (2017)	No	No	Yes	No	No	No
Singh and Abbassi (2018)	Yes	Yes	Yes	Yes	Yes	Yes

A, VCS.

B, AHU.

C, Cabin.

D, Latent heat load by occupants.

E, Humidity of indoor air.

F, Dehumidification at the evaporator.

Developing such a transient simulation model for complex dynamic systems is often a time-consuming and effort-demanding process. Knowledge of building up a network connection and integration of all physical parameters in submodels is essential. Additionally, a proper differential equation solver needs to be selected to avoid some numerical hiccups during simulations. These challenging tasks have been resolved with simulation programming tools that offer different paradigms of modeling approaches; therefore, engineers could put more effort into physical modeling. Transient simulation tools, which have been employed for the research on thermal systems and so frequently mentioned in research articles, are provided in Table 1.4. Previous studies (Elsheikh et al., 2013; Giraud et al., 2014; Wetter & Haugstetter, 2006) compared the acausal, equation-based, and object-oriented tool and the causal, non-equation-based, and non-object-oriented tool. They demonstrated that the former is an effective method that offers a much faster process than implementing model components to create user-defined models with the latter. The industry often shuns causal and non-equation-based approach modeling tools due to the tools' inherent disadvantages. Acausal, equation-based, and object-oriented modeling tools that offer a multi-physical domain fill up this void. Modelica, as a well-known and open-source program, has already passed numerous experimental validations. Like Modelica, Simscape Library offers several physical domains. In each physical domain, modeling physical phenomena that occurred in a practical system can be easily possible using proper component block models representing. Simscape has merits in terms of generating fewer equations. Also, it is user-friendly, powerful for control purposes, and provides more flexible and easy ways for users to extend their models into a multi-physical domain by offering an integrated tool platform (Atom, 2017). Nevertheless, the reported research on the modeling and simulation of physical systems using Simscape is considered rare (Jamila & Abdelmjid, 2013; Qiao et al., 2012; Trčka & Hensen, 2010).

Table 1.4. Transient simulation software (Ko et al., 2020).

Tool	Modeling approach
TRNSYS [a]	Causal, Non-equation-based, and Non-object-oriented
Modelica/Dymola [b]	Acausal, Equation-based, and Object-oriented
MATLAB/Simulink [c]	Causal, Non-equation-based, and Object-oriented
MATLAB/Simscape [d]	Acausal, Equation-based, and Object-oriented

[a] Klein et al. (1976)

[b] Modelica Association/Dassault Systemes®

[c] MathWorks (2018a)

[d] MathWorks (2018b)

This work aims to investigate the transient behavior and performance of an R-744 AC for electric vehicles. A transient model of an AC was developed using MATLAB/Simscape offering an acausal, equation-based, object-oriented, and multi-physical domain modeling platform. The entire model consists of a VCS, AHU, and cabin. Before proceeding with the investigation, the VCS model was validated against the in-house experimental data set, and the models of AHU and cabin were compared with the data from three different research articles. Transient behavior, characteristics, and performance of an AC were investigated using the model in various operating conditions such as start-up, pull-down, ventilation, supply air temperature control, and optimum heat rejection pressure control.

Chapter 2 Modeling and Simulations

2.1 Modeling

The AC model consists of three subsystems, a VCS, an AHU, and a cabin. The component models of each subsystem were established utilizing models from Simscape (MathWorks, 2018c), or some were developed by modifying original models.

2.1.1 Vapor Compression System (VCS)

A property table parameterizes a property of the refrigerant with the pressure (P) and the normalized internal energy ($\bar{u}$) using the embedded function of the used software as follows (MathWorks, 2018c):

Liquid phase ($u_{min} < u < u_L(P)$):

$$\bar{u} = \frac{u - u_{min}}{u_L(P) - u_{min}} - 1, \quad (1)$$

Two-phase mixture ($u_L(P) < u < u_V(P)$):

$$\bar{u} = \frac{u - u_L(P)}{u_V(P) - u_L(P)}, \quad (2)$$

Vapor phase ($u_V(P) < u < u_{max}$):

$$\bar{u} = \frac{u - u_{max}}{u_{max} - u_V(P)} + 2. \quad (3)$$

Here, u indicates the internal energy, and the subscripts, min, max, L, and V, represent the minimum, the maximum, the saturated liquid, and the saturated vapor, respectively. This treatment transforms the pressure-internal energy domain to the pressure-normalized internal energy domain, as shown in Figure 2.1. Properties of the refrigerant specified in the table are obtained from REFPROP ver. 10.0 (Lemmon et al., 2018). The established table consists of 20,000 segments, 100 by 200 (Ko et al., 2021a). The pressure domain consists of 100 segments, from 0.6 MPa to 100 MPa. The internal energy domain consists of 200 segments, from 81 kJ kg^{-1} to 800 kJ kg^{-1}; 100 segments are for the liquid phase and the other 100

segments for the vapor phase. The supercritical fluid is divided into two arbitrary phases: supercritical liquid and supercritical vapor. A property (ζ) at a given pressure and normalized internal energy is decided from this table as follows:

$$\zeta = \zeta(P, \bar{u}). \quad (4)$$

Properties that are not specified in the table are determined by curve-fitted interpolation during the simulation. A property of a two-phase mixture (ζ_2) is decided as follows:

$$\zeta_2 = (1 - x)\zeta_L + x\zeta_V. \quad (5)$$

Here, x represents the vapor quality. The normalized internal energy in the two-phase mixture lies in 0 to 1; hence it is treated as the vapor quality.

Figure 2.1. (a) pressure-internal energy domain and (b) pressure-normalized internal energy domain (Ko et al., 2021a).

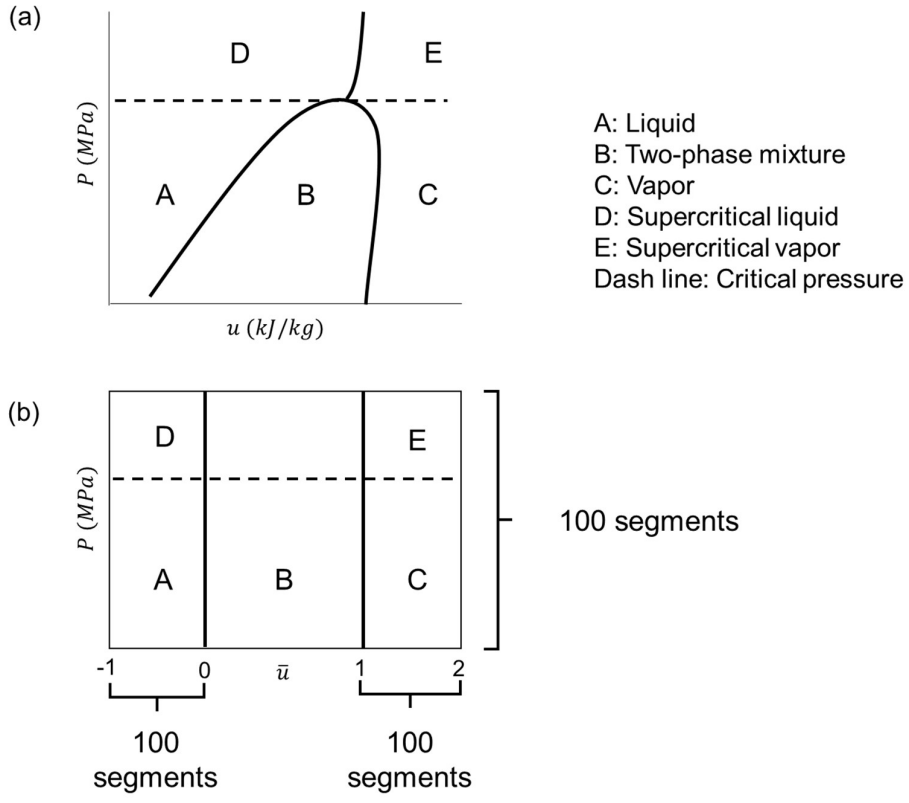

Compressor

Winkler (2009) notes that:

> *In the transient simulation of a vapor compression system, the compressor is often treated as a quasi steady state component; meaning the calculated mass flow rate and discharge temperature instantaneously update based on the current suction conditions and discharge pressure. This is a valid assumption since the timescales associated with the variation of the compressor mass flow rate are very small compared to timescales associated with heat exchanger performance and charge distribution. Dynamic compressor models that capture valve dynamics and mass flow rate variation for each cycle of the compressor motor are too computationally expensive and require too small of time steps to be included in a system level simulation (Ding, 2007). Compressor models utilized in a system simulation generally fall into one of two categories: map-based models and efficiency-based models. (p. 9-10)*
>
> *Map-based models are based on manufacturer data and therefore the performance will most likely match the experimental results. However, the published data provided by compressor manufacturers is valid only over a specific range, which is likely to be violated during a transient simulation. Most manufacturer data has been taken under steady state operation, and thus all the transient phenomena likely to effect the compressor performance during transient time periods will not be taken into account. (p. 10)*
>
> *Efficiency-based models can capture the trends and can match experimental results after the model has been tuned accordingly. However, this approach requires more effort than using a map-based model. Efficiency-based models can make use of either the compressor isentropic efficiency or the refrigerant polytropic coefficient. The refrigerant polytropic coefficient is typically not constant under varying conditions and attaining a value for the polytropic coefficient for a variety of refrigerants is often difficult. (p. 10)*

From Winkler (2009), a compressor model was established using the efficiency-based modeling method with the assumptions as follows (Ko et al., 2020; Ko et al., 2021a):

1. The compressor is treated as a quasi-steady-state component.
2. The pressure drops of the refrigerant flow in the connecting tubes at the suction and discharge are negligible.
3. Heat gain or loss of the compressor's body is neglected.
4. The compression process of the refrigerant is isentropic.
5. Mechanical efficiency is assumed to be 100%.

Mass conservation equation is given as follows:

$$\dot{m}_o = \dot{m}_i = \eta_v \rho_i V_{comp} S_{comp}, \quad (6)$$

where $\dot{m}_o$, $\dot{m}_i$, η_v, V_{comp}, ρ_i, and S_{comp} represent the refrigerant mass flow rate at the compressor outlet (i.e., discharge) and the refrigerant mass flow rate at the compressor inlet (i.e., suction), the volumetric efficiency, the swept volume, refrigerant density at the suction, and the rotational speed, respectively. Compressor power ($\dot{W}_{comp}$) is calculated as follows:

$$\dot{W}_{comp} = \dot{m}_i \sum_i^o \left(h^* + \frac{(Gv)^2}{2} \right), \quad (7)$$

where h^*, G, and v represent the specific enthalpy, the mass flux, and the specific volume, respectively. The specific enthalpy of the refrigerant at the outlet is given by:

$$h_o^* = \left(\frac{h_o^*(P_i, s_i) - h_i^*}{\eta_s} \right) + h_i^*, \quad (8)$$

where η_s represents the isentropic efficiency. The isentropic efficiency (η_s) and volumetric efficiency (η_v) models are adopted from Petter et al. (2004).

Refrigerant Flow in HXs

The key to modeling refrigerant flow in HXs is determining the proper size of a computational segment (i.e., control volume) and treatment of working fluid phases. When a single control volume is assigned to a single HX, the HX is analyzed based on the lumped parameters. The heat transfer between the refrigerant and secondary fluid is evaluated based on an average heat transfer coefficient in the entire HX. This approach offers simplicity and

computation efficiency. However, since the model does not consider the spatial variation in refrigerant properties and the distinct differences of the heat transfer mechanisms between single-phase and two-phase fluids, they result in relatively inaccurate predictions. Multi control volumes are necessary to achieve more satisfactory predictions. Many control volumes guarantee superior predictions; however, it always accompanies more computational costs. Concerning treatment for working fluid's phases, properties are determined based on the known states if in a single-phase flow. However, determining properties is not easy in a two-phase flow. There are several types of two-phase flow models: the homogenous model, separated flow model, drift flux model, two-fluid model, and three-fluid model. The simplest one is the homogeneous equilibrium model, which assumes that the two phases are well-mixed, are in thermodynamic equilibrium, and have the same phase velocity. The homogeneous-equilibrium model is often adopted in the transient modeling of VCSs, while others are rarely used since they are relatively complicated and impose more computation burden, although they can capture physical phenomena better than the homogeneous-equilibrium model (Qiao, 2014).

A model for the refrigerant channel in HXs was established with the assumptions as follows (Ko et al., 2020; Ko et al., 2021a):

1. Refrigerant flow is one-dimensional and fully developed.
2. The gravitational effect is neglected. The pressure drop due to gravity has a relatively minimal contribution to the total pressure drop of the refrigerant flow. The amount of potential energy change is relatively smaller than the enthalpy and kinetic energy.
3. Two phases are well-mixed, are in thermodynamic equilibrium, and have the same phase velocity; thus, a two-phase flow is treated employing the homogeneous equilibrium model.
4. The heat transfer rate is calculated using the refrigerant properties defined at the bulk temperature.

Figure 2.2 shows the segment for the refrigerant flow; (a) is for mass and energy conservation and (b) is for the pressure drop calculation.

Figure 2.2. Segments for the refrigerant flow (Ko et al., 2020).

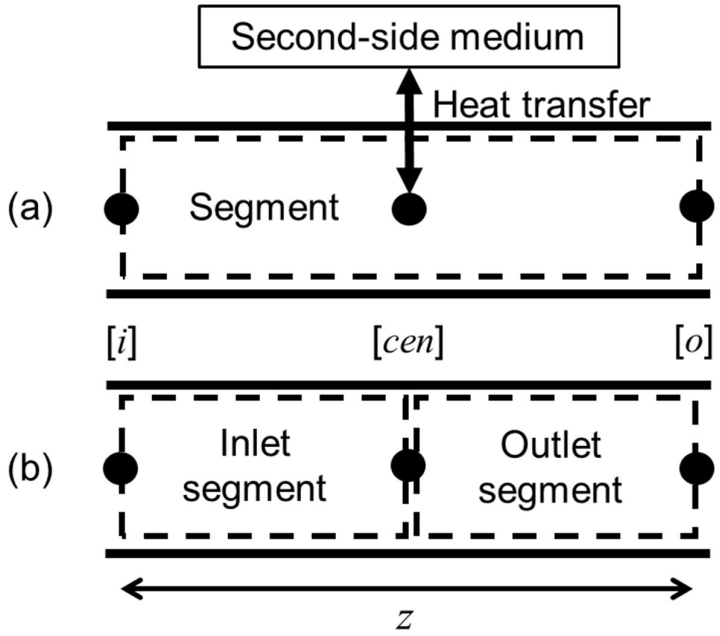

Mass conservation equation is given as follows:

$$\left[\left(\frac{\partial\rho}{\partial P}\right)_u\left(\frac{dP}{dt}\right)+\left(\frac{\partial\rho}{\partial u}\right)_P\left(\frac{du}{dt}\right)\right]_{cen} V_{ch}=\sum_i^o \dot{m}, \tag{9}$$

where t and V_s represent the time and the segment volume, respectively. The subscripts cen, i, and o represent the center, inlet, and outlet of the segment. The energy conservation equation is given as follows:

$$(\dot{m}_i+\dot{m}_o)\left(\frac{du_{cen}}{dt}\right)+u_{cen}\left(\frac{d(\dot{m}_i+\dot{m}_o)}{dt}\right)=\sum_i^o\left[\dot{m}\left(h^*+\frac{(Gv)^2}{2}\right)\right]+\dot{Q}_{ref}. \tag{10}$$

Here, the heat transfer rate of refrigerant flow, $\dot{Q}_{ref}$, is calculated as follows:

$$\dot{Q}_{ref}=hA(T-T_{in.wall}), \tag{11}$$

where h, A, T, and $T_{in.wall}$ represent the heat transfer coefficient, the heat transfer area, the refrigerant temperature, and the inner wall temperature. The heat transfer coefficient of refrigerant flow is calculated as follows:

Single-phase flow (h_1):

$$h_1 = \frac{k_{cen.1} Nu_1}{D_h}, \tag{12}$$

Two-phase flow (h_2):

$$h_2 = \frac{k_{cen.L} Nu_2}{D_h}. \tag{13}$$

where k, Nu, and D_h represent the thermal conductivity and the Nusselt number of the refrigerant flow, respectively, the hydraulic diameter of the channel. The pressure drop equation is given as follows (Ghiaasiaan, 2007):

$$\left(-\frac{dP}{dz}\right)_{total} = \left(-\frac{dP}{dz}\right)_{friction} + \left(-\frac{dP}{dz}\right)_{acceleration} + \left(-\frac{dP}{dz}\right)_{gravitation} + \left(-\frac{dP}{dz}\right)_{minor}, \tag{14}$$

where the z represents the length of a channel. In the right hand of Eq. 14, the last term represents the pressure drop due to the cross-section area change of flow passage, such as inlet or outlet. From the assumptions, Eq. 14 is simplified as follows:

$$\left(-\frac{dP}{dz}\right)_{total} = \left(-\frac{dP}{dz}\right)_{friction} + \left(-\frac{dP}{dz}\right)_{acceleration}. \tag{15}$$

Eq. 15 is assigned to the inlet segment and the outlet segment, respectively, with the following form:

For the inlet segment:

$$P_i - P_{cen} = G_i|G_i(v_{cen} - v_i)| + \left(\frac{f_{D.i}G_i^2 v_{cen}}{2D_h}\right)\left(\frac{z}{2}\right), \quad (16)$$

For the outlet segment:

$$P_o - P_{cen} = G_o|G_i(v_{cen} - v_o)| + \left(\frac{f_{D.o}G_o^2 v_{cen}}{2D_h}\right)\left(\frac{z}{2}\right), \quad (17)$$

where f_D represents the Darcy friction factor. Except for the Darcy friction factor and Nusselt numbers in the three balance equations, the remaining variables are geometric dimensions and refrigerant properties. The friction factor and Nusselt numbers are calculated using the model and correlations summarized in Table 2.1.

Table 2.1. Model and correlations for the friction factor and Nusselt number (Ko et al., 2020; 2021a).

Parameter	Applicable condition	Model and Correlations
Friction factor	Single-phase laminar flow	$64/Re_1$ (Incropera et al., 2007)
	Single-phase turbulent flow	Haaland (1983)
	Two-phase flow	Haaland (1983), using Re_2
Nusselt number	Single-phase laminar flow	3.66 (Incropera et al., 2007)
	Single-phase turbulent flow	Gnielinski (1976)
	Two-phase flow	Fang (2013) and simplified Chen (1966) [a]

[a] Ko et al. (2021a)

The friction factor in the transition regime between the laminar and turbulent flow ($f_{D.trans}$) is calculated as follows:

$$f_{D.trans} = (1 - C)f_{D.lam} + Cf_{D.tur}, \quad (18)$$

where the coefficient, C, is obtained by the polynomial function as follows:

$$C = 3\left[\frac{(Re-2000)}{(4000-2000)}\right]^2 - 2\left[\frac{(Re-20\quad)}{(4000-2000)}\right]^3. \quad (19)$$

Here, Reynolds numbers for the flow regime criteria are as follows:

Laminar:

$$Re < 2000, \quad (20)$$

Transition:

$$2000 \leq Re \leq 4000, \quad (21)$$

Turbulent:

$$4000 < Re. \quad (22)$$

Nu_{trans} is calculated employing Gnielinski (1976). If the calculated value is greater than $Nu_{lam.1}$, h_{trans} is evaluated based on Nu_{trans}. If not, h_{trans} is decided based on $Nu_{lam.1}$. A working medium undergoes phase change between liquid, two-phase, and vapor phase at HXs in an actual VCS. In the phase boundary, the refrigerant properties and thermo-fluidic parameters change discontinuously, and the corresponding numerical processes become unstable; thus, proper treatment requires avoiding that.

For the smooth transition of the density partial derivatives near phase boundary, the following buffer layers are used:

For $0 < x < 0.1$:

$$\left(\frac{\partial \rho}{\partial P}\right)_u = (1 - C)\left(\frac{\partial \rho_L}{\partial P_L}\right)_{u_L} + C\left(\frac{\partial \rho_2}{\partial P_2}\right)_{u_2}, \quad (23)$$

$$\left(\frac{\partial \rho}{\partial u}\right)_P = (1 - C)\left(\frac{\partial \rho_L}{\partial u_L}\right)_{P_L} + C\left(\frac{\partial \rho_2}{\partial u_2}\right)_{P_2}, \quad (24)$$

$$C = 3\left[\frac{(x-0)}{(0.1-0)}\right]^2 - 2\left[\frac{(x-0)}{(0.1-0)}\right]^3. \quad (25)$$

For $0.9 < x < 1$:

$$\left(\frac{\partial \rho}{\partial P}\right)_u = (1 - C)\left(\frac{\partial \rho_2}{\partial P_2}\right)_{u_2} + C\left(\frac{\partial \rho_V}{\partial P_V}\right)_{u_V}, \quad (26)$$

$$\left(\frac{\partial \rho}{\partial u}\right)_P = (1 - C)\left(\frac{\partial \rho_2}{\partial u_2}\right)_{P_2} + C\left(\frac{\partial \rho_V}{\partial u_V}\right)_{P_V}, \quad (27)$$

$$C = 3\left[\frac{(x-0.9)}{(1-0.9)}\right]^2 - 2\left[\frac{(x-0.9)}{(1-0.9)}\right]^3. \quad (28)$$

For the smooth transition of heat transfer coefficient near phase boundary, the buffer layers are defined employing void fraction (α) and quality as follows:

For $0 < \alpha < 0.1$:

$$h = (1 - C)h_L + Ch_2, \quad (29)$$

$$C = 3\left[\frac{(\alpha-0)}{(0.1-0)}\right]^2 - 2\left[\frac{(\alpha-0)}{(0.1-0)}\right]^3, \quad (30)$$

For $0.9 < x < 1$:

$$h = (1 - C)h_2 + Ch_V \quad (31)$$

$$C = 3\left[\frac{(x-0.9)}{(1-0.9)}\right]^2 - 2\left[\frac{(x-0.9)}{(1-0.9)}\right]^3. \quad (32)$$

Expansion Device

An expansion device regulates the system pressure, refrigerant mass flow rate entering the evaporator, and the degree of suction superheating. Expansion valves, orifices, and capillary tubes are used as an expansion device. A refrigerant passing through those expansion devices undergoes a rapid change in thermophysical properties, and this thermo-hydraulic mechanism is very complicated. Capillary tubes are typically used for small-size systems, which face a relatively small variation on cooling load, for example, household refrigerator-freezers. For automobile ACs, an expansion valve or a short orifice tube is typically adopted, depending on the system layout. When modeling the refrigerant flowing through those throttling devices, it is generally assumed that no heat transfer occurs, so the isenthalpic process is regarded, except in some particular applications.

The modeling approach of expansion devices can be categorized into empirical and theoretical approaches. The empirical method calculates the mass flow rate given operating conditions based on the correlation obtained from experimental data. This method uses empirical equations and shows good accuracy. However, this accuracy is only valid in the operating range where the experimental data sources. However, theoretical models can be used much wider compared to correlation-based models; thus, the current expansion device modeling adopted a simple theoretical approach.

Figure 2.3 shows a schematic of an expansion valve as an example. Various methods control the displacement of the needle, the type of expansion valves is categorized with the control methods. On the other hand, the physical phenomenon that refrigerant undergoes at the orifice section is identical regardless of the type of valves, also even in a short orifice tube. Thus, the present expansion device model was established considering the orifice part only. Figure 2.4 shows a schematic of the model. The model controls the cross-sectional area of the orifice part and thereby regulates the refrigerant mass flow rate. The model was established with the assumptions that the orifice is adiabatic and that the expansion process is isenthalpic.

Figure 2.3. Schematic of an expansion valve.

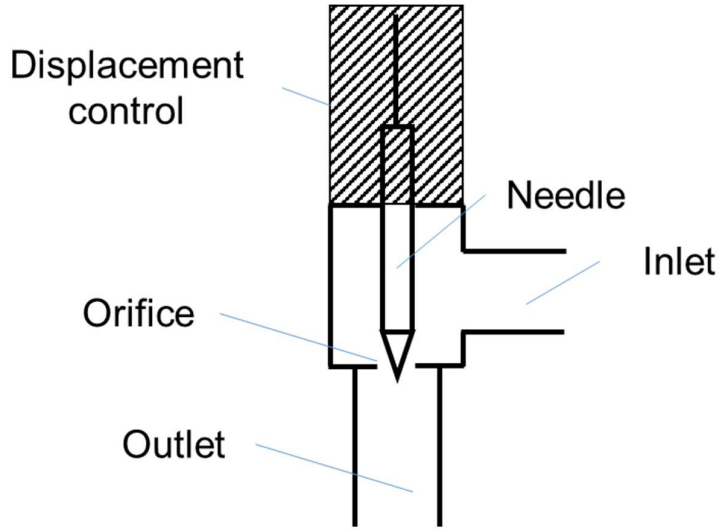

Figure 2.4. Segment for the orifice part.

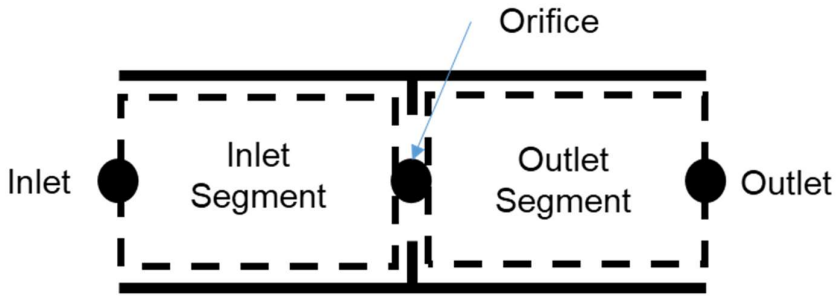

Mass and energy conservation equations are as follows:

$$\dot{m}_{ex.i} = \dot{m}_{ex.o}, \tag{33}$$

$$h^*_{ex.i} = h^*_{ex.o}. \tag{34}$$

where the subscript, ex, represents the expansion device. The refrigerant mass flow rate by irreversible pressure drop (i.e., the momentum change) is calculated as follows:

$$\dot{m}_{ex} = C_D A_{c.ori} \left[\frac{2(P_{ex.i} - P_{ex.o})}{v_{ori} K}\right]^{0.5}. \tag{35}$$

C_D and K represent the flow coefficient and correction factor, respectively. The flow coefficient varies with a given geometric dimension and flow condition, so it is regarded as an empirical factor. In this modeling, it was set to be 0.64, which is provided as a default value from the used software. The correction factor is for a smooth numerical computation between laminar and turbulent transition, which is decided by the default setting of the original Simscape model. Here, the flow regime is determined based on the Simscape embedded logic.

Validation

Figure 2.5 shows a schematic of an experimental apparatus. The apparatus consists of an R-744 VCS, a cooling water loop, and a heating water loop. The VCS consists of a scroll-type compressor, a tube-in-tube type HX as a gas cooler, an electronic expansion valve (EEV), and a plate-type HX as an evaporator. Figure 2.6 shows a schematic of the gas cooler and the evaporator. The gas cooler consists of three inner tubes and a single outer tube. The refrigerant flows inside the three inner tubes while the cooling water flows annular space between the inner tubes and outer tube. The evaporator consists of ten channels of the refrigerant flow and eleven channels of the heating water flow. Specification of the mentioned four main components of the VCS is summarized in Table 2.2. An oil separator at the compressor discharge is utilized to rid the effects of lubricant oil circulation. Sight-glasses are to check the refrigerant phase at the evaporator inlet and the compressor suction. Each water loop consists of a constant temperature water bath, a circulation pump, a gear-type flow meter, and a by-pass valve. During the experiments, the pressure and temperature of

refrigerant flow were measured at each main component's inlet and outlet by pressure sensors and K-type thermocouples, respectively. The refrigerant mass flow rate was measured by a Coriolis mass flow meter installed at the inlet of the EEV. Thermocouples (K-type) measured the water temperatures at the inlet and outlet of each HX. The water flow rate in each water loop was measured by the gear-type flow meter. The feedwater flow in each water loop was regulated by the by-pass valve. Controlling the water temperature at each HX inlet was performed by the constant temperature water bath installed in each water loop. In the gas cooler, the refrigerant heat was rejected to the cooling water, while in the evaporator, the heating water heat was absorbed into the refrigerant. The degree of superheating at the compressor suction was adjusted by the opening of the EEV. Electric signal using a digital panel manually controlled the opening of the EEV. The rotational speed of the compressor was controlled by an inverter. The compressor and inverter are connected to a power meter. Readings of power and speed were indicated in a display window to check its input power and speed. All the measuring instruments are connected to a data acquisition system. Their readings were recorded every second. The experimental range carried out in the present study is provided in Table 2.3.

Figure 2.5. Schematic of the experimental apparatus (Ko et al., 2020).

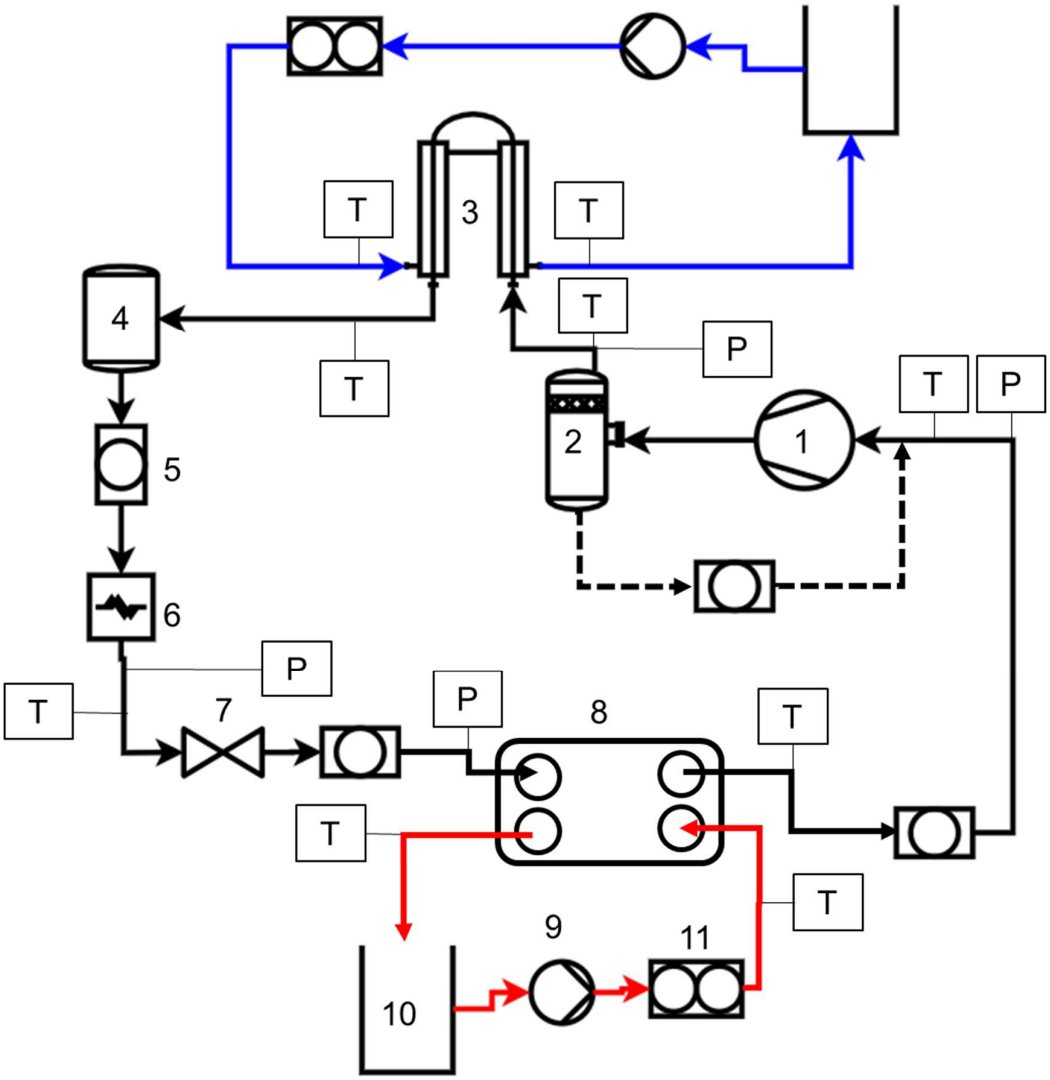

1: Compressor, 2: Oil separator, 3: Gas cooler, 4: Receiver, 5: Sight glass, 6: Coriolis mass flow meter, 7: EEV, 8: Evaporator, 9: Pump, 10: Water bath, 11: Gear flow meter, P: pressure sensor, T: Thermocouple, →: Refrigerant flow, →: Cooling water flow, →: Heating water flow, ⇢: Lubricant oil

Figure 2.6. Schematic of the gas cooler and evaporator (Ko et al., 2020).

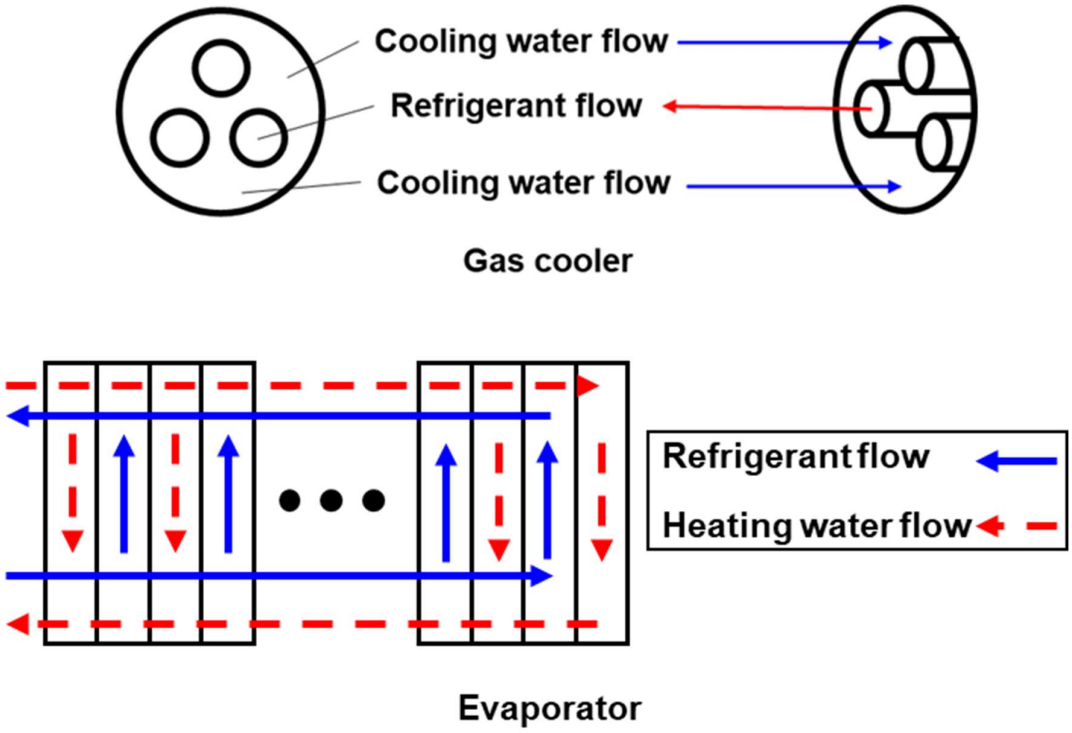

Table 2.2. Components of the experimental VCS (Ko et al., 2020).

Component	Value	Unit
Compressor		
Swept volume	4.0	cm^3
Maximum rotational speed	90	rev s^{-1}
The diameter of suction and discharge tubes	6.53	mm
Gas cooler		
The inner diameter of the inner tubes	2.8	mm
The outer diameter of the inner tubes	4.4	mm
The inner diameter of the outer tube	14.6	mm
The outer diameter of the outer tube	16.0	mm
Tube length	13.6	m
Heat transfer area	0.578	m^2
EEV		
The diameter of the inlet and outlet tubes	6.35	mm
Maximum pressure at the inlet	14	MPa
Maximum differential pressure	10	MPa
Operating range (0 to 500 steps)		
Evaporator		
Width	90	mm
Depth	35	mm
Height	434	mm
Heat transfer area	0.648	m^2

Table 2.3. Experimental range (Ko et al., 2020).

Operating parameter	Range	Unit
Gas cooler		
Water flow rate	45 to 145	L h^{-1}
Water inlet temperature	20 to 30	^{o}C
Evaporator		
Water flow rate	77 to 350	L h^{-1}
Water inlet temperature	15 to 20	^{o}C
Charge amount	1.4 to 1.7	kg
Refrigerant mass flow rate	35 to 55	kg h^{-1}
Suction pressure	3.4 to 4.7	MPa
Discharge pressure	7.8 to 10.5	MPa
Suction superheating	2 to 20	^{o}C
Discharge temperature	70 to 100	^{o}C
Ambient temperature	20 to 26	^{o}C

Heat transfer rates in the refrigerant-side and water-side at each HX were calculated by:

Refrigerant-side:

$$\dot{Q}_{ref} = \dot{m}_{ref}\Delta h^*_{ref}, \quad (36)$$

Water-side:

$$\dot{Q}_w = \dot{V}_w \rho_{w.i} \left(\frac{C_{P.w.i}+C_{P.w.o}}{2}\right) \Delta T_w, \quad (37)$$

where Δh^*_{ref}, $\dot{V}_w$, $\rho_{w.i}$, $C_{P.w.i}$, $C_{P.w.o}$, and ΔT_w represent the refrigerant specific enthalpy difference between the inlet and outlet of each HX, the water flow rate, the water density at the inlet of each HX, the specific heats of water at the inlet and outlet of each HX, and the temperature difference of water between at the inlet and outlet of each HX, respectively. COPs for cooling and heating were assessed as follows:

$$COP_c = \frac{\dot{Q}_{w.evap}}{\dot{W}_{comp}}, \quad (38)$$

$$COP_h = \frac{\dot{Q}_{w.gc}}{\dot{W}_{comp}}. \quad (39)$$

Efficiencies (η_v and η_s) of the compressor were derived from a set of 63 experimental data obtained under each steady-state condition, independently. The obtained fitting equations (Ko et al., 2020) were applied to the compressor model for validation.

Reduced data have a relationship with measured data (i.e., independent variables) as follows:

$$\Psi = f(\psi_1, \psi_2, \dots, \psi_n), \quad (40)$$

where Ψ and ψ represent the reduced data and the measured data, correspondingly. Uncertainty of the reduced data can be calculated approximately by:

$$U_{\Psi} = \left[\sum_{i=1}^{n}\left(\frac{\partial}{\partial\psi_i} f(\psi_1, \psi_2, \ldots, \psi_n)\right) U_{\psi_i}\right]^{0.5}, \quad (41)$$

where U_{Ψ} and U_{ψ_i} represent the uncertainty of the reduced data and the uncertainty of independently measured data, respectively. Uncertainties of measured and reduced data are summarized in Table 2.4.

Table 2.4. Uncertainties of experimental data (Ko et al., 2020).

Content	**Uncertainty**
Temperature, °C	±0.1
Pressure, MPa	
at the gas cooler inlet	±0.044
at the EEV inlet	±0.040
at the EEV outlet	±0.015
at the suction	±0.017
Refrigerant mass flow rate, kg h^{-1}	±1.08% of reading
Water flow rate, L h^{-1}	
at the cooling water loop	±1.0
at the heating water loop	±1.0
Compressor power, kW	±(0.1% of reading+0.002)
Heating capacity of the gas cooler, kW	±5.4% of the value
Cooling capacity of the evaporator, kW	±5.3% of the value
COP for heating	±5.5% of the value
COP for cooling	±5.4% of the value

Figure 2.7a shows the VCS model. The system consists of four subsystems; a compressor, a gas cooler, an expansion device, and an evaporator. Each subsystem, representing the main component of the experimental VCS, consists of the physical block models. In the compressor model, the swept volume and diameters of connecting tubes were set up with the identical values of the experimental compressor. The refrigerant mass flow rate is calculated based on the input rotational speed, the refrigerant density at the suction, the swept volume, and the volumetric efficiency. In the gas cooler model, a single control volume was assigned to each inner-tube of the experimental gas cooler; the hydraulic diameter and the length of the model were set to be the identical values as that of the experimental gas cooler, respectively. The evaporator model consists of ten control volumes representing the ten refrigerant channels in the experimental evaporator. The hydraulic diameter of each channel was assumed 3 mm, so the length was determined to 6.9 m; this setting was decided from the overall heat transfer area and the number of refrigerant channels in the original evaporator. The gas cooler and evaporator models are connected to each temperature setting block representing thermal reservoirs, and the flow is uniformly distributed when the refrigerant flows into each channel. In the expansion device model, the connecting tubes' diameter was set up with the identical value of the experimental EEV. The orifice cross-sectional area of the expansion device is controlled by the control logic illustrated in Figure 2.7b. The target temperature difference between the suction and the expansion device outlet, $\Delta T_{target} = (T_{suc} - T_{ex.o})_{target}$, becomes the control target. A constant value of ΔT_{target} was set for steady-state simulations and time-dependent variable values of ΔT_{targe} were set for transient simulations. A temperature difference at the present time-step, $\Delta T_{present} = (T_{suc} - T_{ex.o})_{present}$, represents the Signal from the system. PI-controller calculates the control variable during simulations; the proportional and integral coefficients were obtained by the linearization approach using 'PID Tuner' supported by the Simulink. The cross-sectional area of the orifice for the next time-step was decided based on the obtained control variable and reference value.

The four components are connected and build up a physical network. A set of physical variables of the refrigerant are computed in each model during simulations; this variable set transfers to the adjacent models by the connecting lines and affects each other. The gas cooler and evaporator models are connected with each thermal reservoir, respectively. In the Thermal domain, the heat transports from high temperature to low temperature based on physical law in given temperature conditions.

Figure 2.7. (a) VCS model and (b) orifice cross-sectional area control logic (Ko et al., 2020).

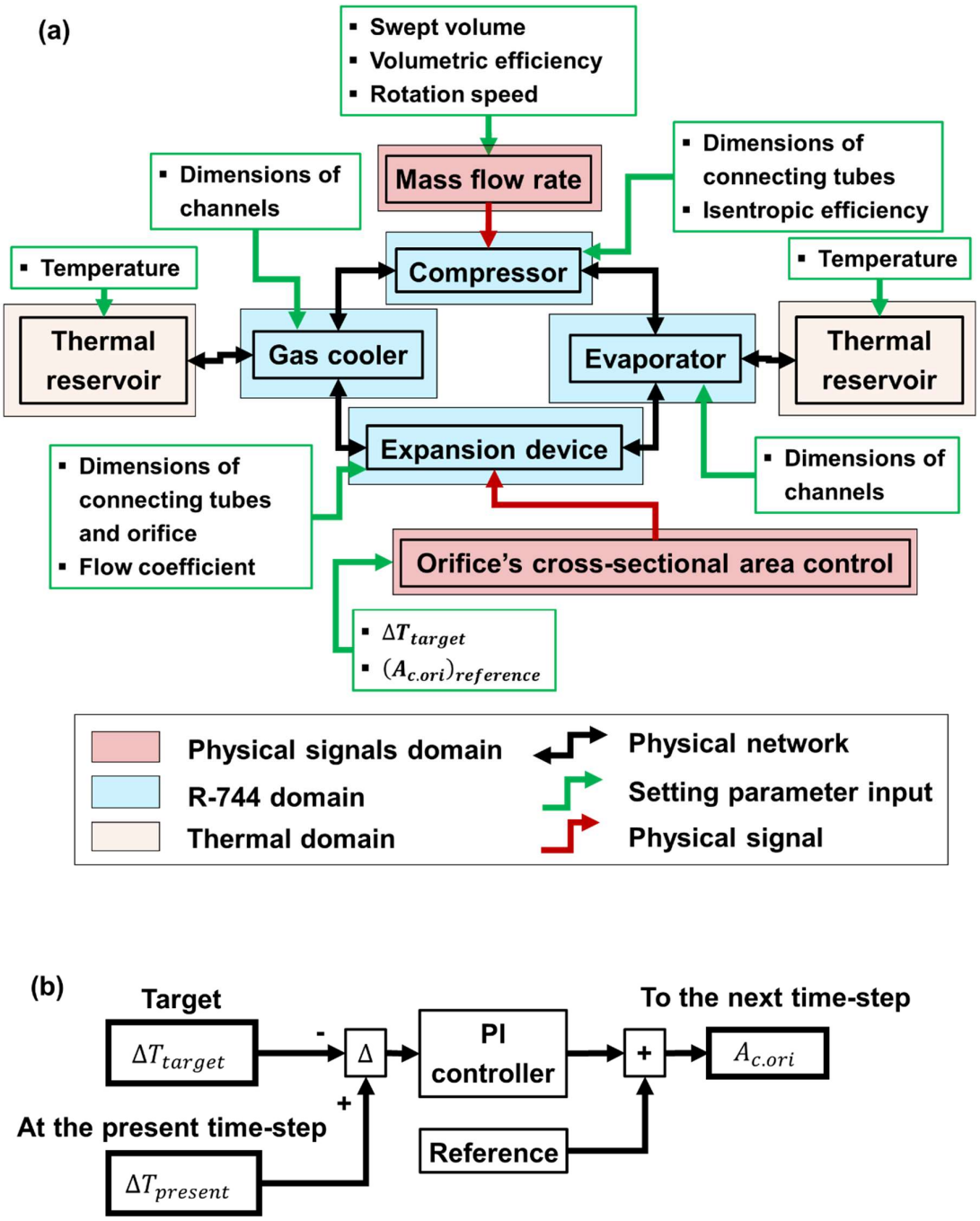

Figure 2.8 describes a simulation flow chart. When a transient simulation starts, a solver builds up a physical network of the VCS based on the setting parameters in each component model and the input values. Then, a system of equations is constructed based on the constructed physical network. The solver analyzes the constructed system of equations and eliminates variables that are not needed to solve the system of equations. Then, the solver computes the initial conditions by finding initial values (at t=0) for all variables in each component model. These initial values must be satisfied with the whole physical conservation equations. When the solver finds the initial values, it starts computing by the end of the set simulation time. After each simulation finished, the result values, such as the refrigerant mass flow rate, thermodynamic states at each point, capacities of each HX, and compressor's power, were obtained in each time-step. One of the variable time-step implicit solvers, ode23t, was selected since it showed the shortest running time compared to other variable time-step implicit solvers. For the steady-state simulations, a long enough time, 3600 seconds, was set for the transient simulation time. After each transient simulation finished, the operating parameters of the VCS model, such as the refrigerant mass flow rate, pressure, and temperature, were checked. When these values lie within the experimental uncertainties without any variation, it was decided that the VCS model reached a steady-state.

Figure 2.8. Flow chart (Ko et al., 2020).

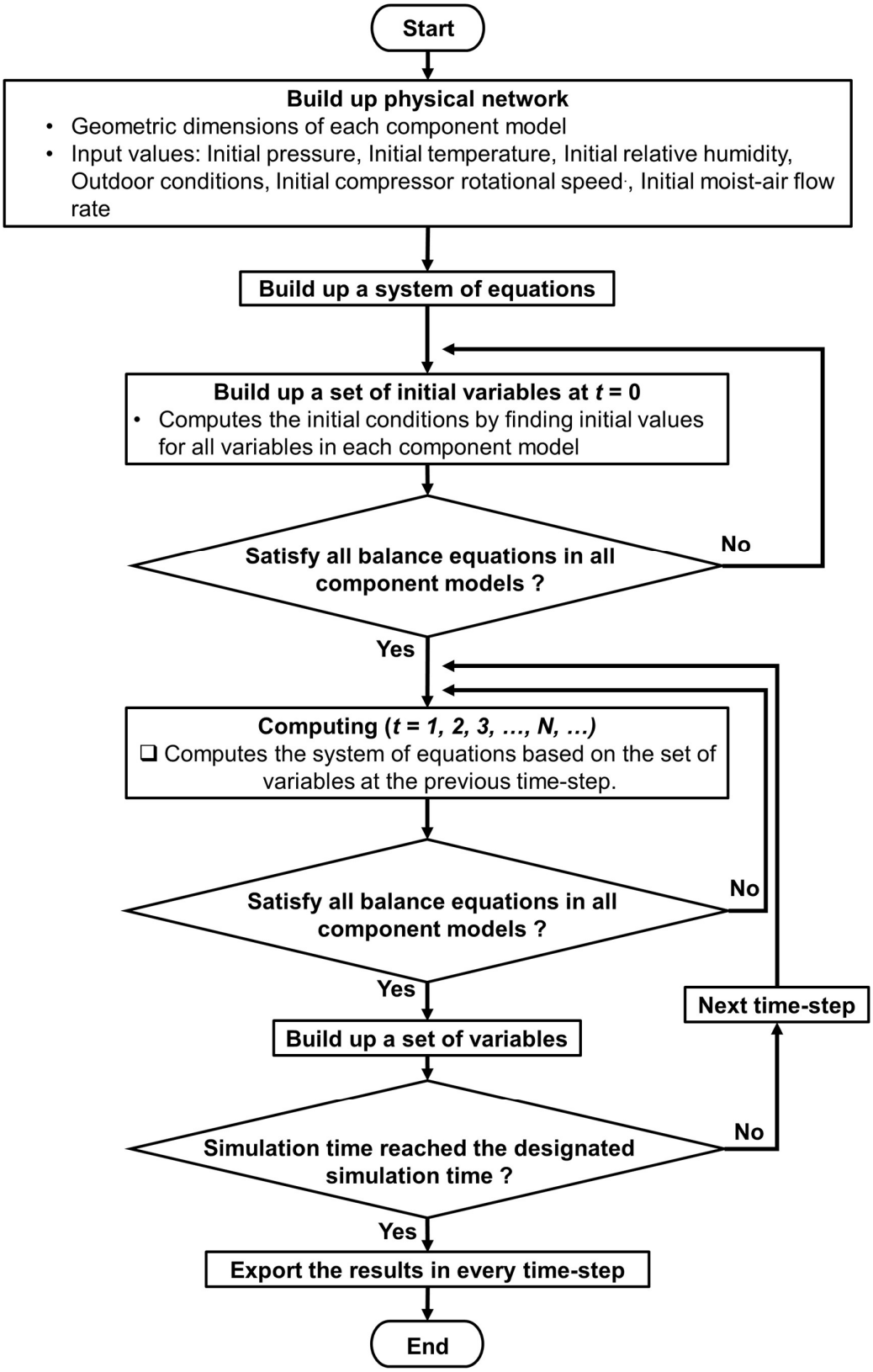

A set of experiments was carried out in steady-state conditions. Each experiment was carried out to achieve the target cooling and heating capacities. The adjusting parameters for the cooling capacity were 1.6 and 1.8 kW for the evaporator. The heating capacity range for the gas cooler was adjusted within 2.4 kW to 3 kW. The compressor rotational speed was selected as the identical value obtained from each experiment. The target temperature difference between the suction and the expansion device outlet (ΔT_{target}) was adjusted to fulfill the experimental mass flow rate of the refrigerant. Figure 2.9 shows the prediction performance of the model. The results show that the model predicts the refrigerant mass flow rate, heating, and cooling capacity of each HX, compressor power, and COPs within the maximum error of ± 7%. (Appendix A provides the experimental conditions, results, simulation conditions, and results, for each case in detail.)

Figure 2.9. Comparison results (Ko et al., 2020).

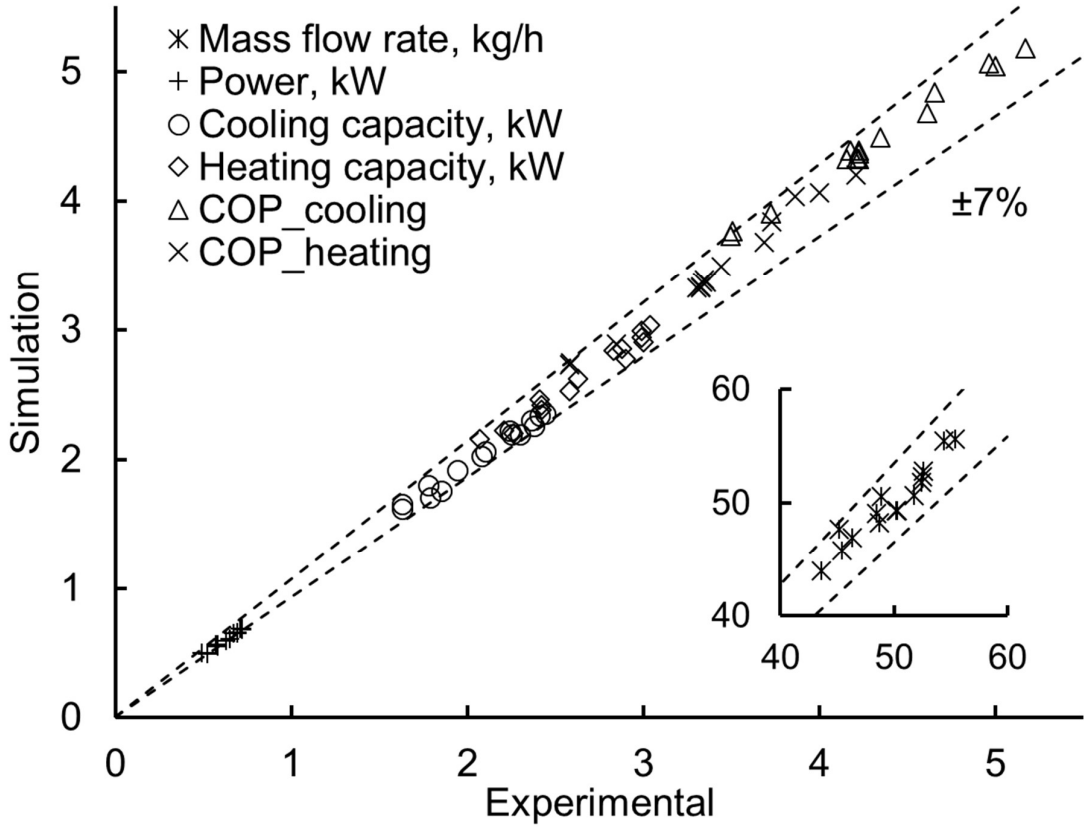

A set of experiments was carried out with changing compressor rotational speed. Figure 2.10a shows the compressor rotational speed and the measured temperature difference between the suction and the EEV outlet, $(T_{suc} - T_{ex.o})$, when the rotational speed was suddenly increased from 60 rev s^{-1} to 87 rev s^{-1}. During the experiment, cooling water was supplied to the gas cooler with a flow rate of 128.7 L h^{-1} and a temperature of 30 ºC. The heating water was supplied to the evaporator with a flow rate of 99.9 L h^{-1} and a temperature of 20 ºC. Those feed water conditions were kept constant during the experiment. For the simulation, the experimental compressor speed provided in Figure 2.10a was used as an input value for the compressor model. The measured temperature difference was also used for the input value to the expansion device model as the target value of the temperature difference. The temperature of the thermal reservoir at the gas cooler model was set to 31 ºC, and the temperature of the thermal reservoir at the evaporator model was set to 8.3 ºC. In the gas cooler, the input values of the refrigerant pressure and temperature were set to 7.7 MPa and 32 ºC, respectively, while the input values of the refrigerant pressure and temperature were set to 4.5 MPa and 11 ºC, respectively, in the evaporator.

Figure 2.10b shows the compressor rotational speed and the measured temperature difference between the suction and the EEV outlet when the rotational speed was suddenly decreased from 80 rev s^{-1} to 60 rev s^{-1}. In this experiment, the cooling water temperature at the gas cooler inlet was fixed to 30 ºC, and the heating water temperature at the evaporator inlet was fixed to 20 ºC. The feed pump in the cooling water loop supplied cooling water to the gas cooler with a flow rate of 129.6 L h^{-1}. In the heating water loop, the pump provided heating water with a flow rate of 118.4 L h^{-1}. For the simulation, the measured compressor speed was used for the compressor model's input value; the measured temperature difference was used for the input value as the target temperature difference in the expansion device model. The temperature of the thermal reservoir at the gas cooler model was set to 29 ºC, and the temperature of the thermal reservoir at the evaporator model was set to 8.3 ºC. In the gas cooler, the input values of the refrigerant pressure and temperature were set to be 7.9 MPa and 32 ºC, respectively. The refrigerant pressure of 4.5 MPa and the refrigerant temperature of 11 ºC were input into the evaporator model.

Figure 2.10. Compressor rotational speed and the temperature difference between the suction and the EEV outlet; (a) when the speed increases and (b) when the speed decreases (Ko et al., 2020).

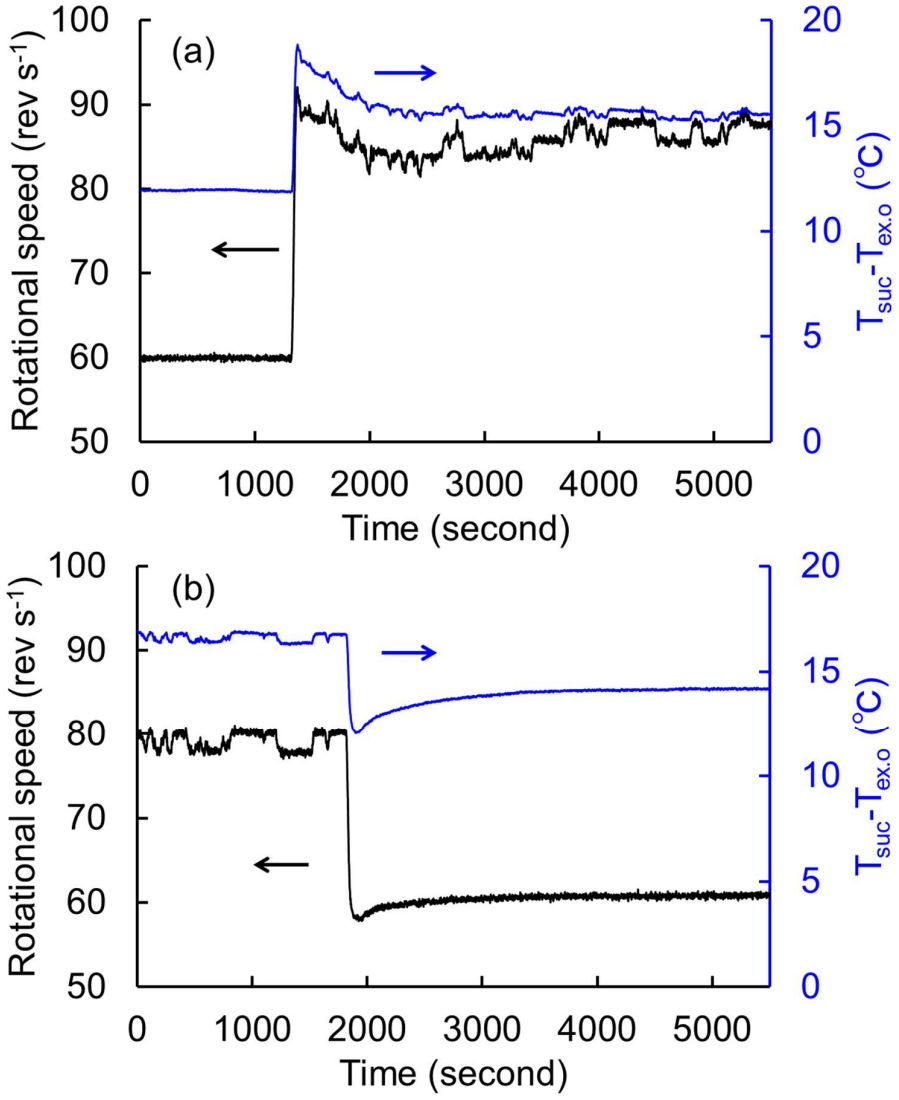

The comparison results between the simulations and the experiments are described in Figure 2.11 and Figure 2.12. The results in Figure 2.11 corresponds to the case when the compressor speed suddenly increases and, the results in Figure 2.12 corresponds to the case when the scroll compressor speed suddenly decreases, respectively. The comparison results show that the simulation model is a good agreement with the dynamic behavior of the experimental system and the corresponding performance change. However, there is a difference between the simulation and the experimental results in the gas cooler pressure and the heating capacity of the gas cooler, right after the compressor speed changes; also, this difference is commonly observed in both figures. The corresponding simulation's results show an immediate response against the change; however, the corresponding experimental results show a gradual response against the change. This difference is mainly due to the compressor model. The present compressor model does not consider heat transfer between the compressor body and the ambient and mechanical losses. The input power does not fully contribute to increasing the refrigerant enthalpy during the compression process in an actual compressor. There is a loss of the input power; therefore, it takes a significant time to supply the refrigerant with enough enthalpy. In Figure 2.11 (c and e) and Figure 2.12 (c and e), the simulation results show that the calculated suction pressure and the cooling capacity at the evaporator are a good agreement with the response of the experimental system even though right after the compressor speed changes. When the compressor speed changes in a real system, the operating parameters in the low-pressure side of the system (such as the suction pressure, the suction temperature, and the suction flow rate) immediately respond to this change; therefore, the cooling capacity of the evaporator also responses this immediate change in an actual case. Meanwhile, it is confirmed again that the model has a prediction error within ± 7% when the system is in stable condition.

Figure 2.11. Comparison results when the rotational speed increases; (a) mass flow rate, (b) gas cooler inlet pressure, (c) suction pressure, (d) heating capacity, and (e) cooling capacity (Ko et al., 2020).

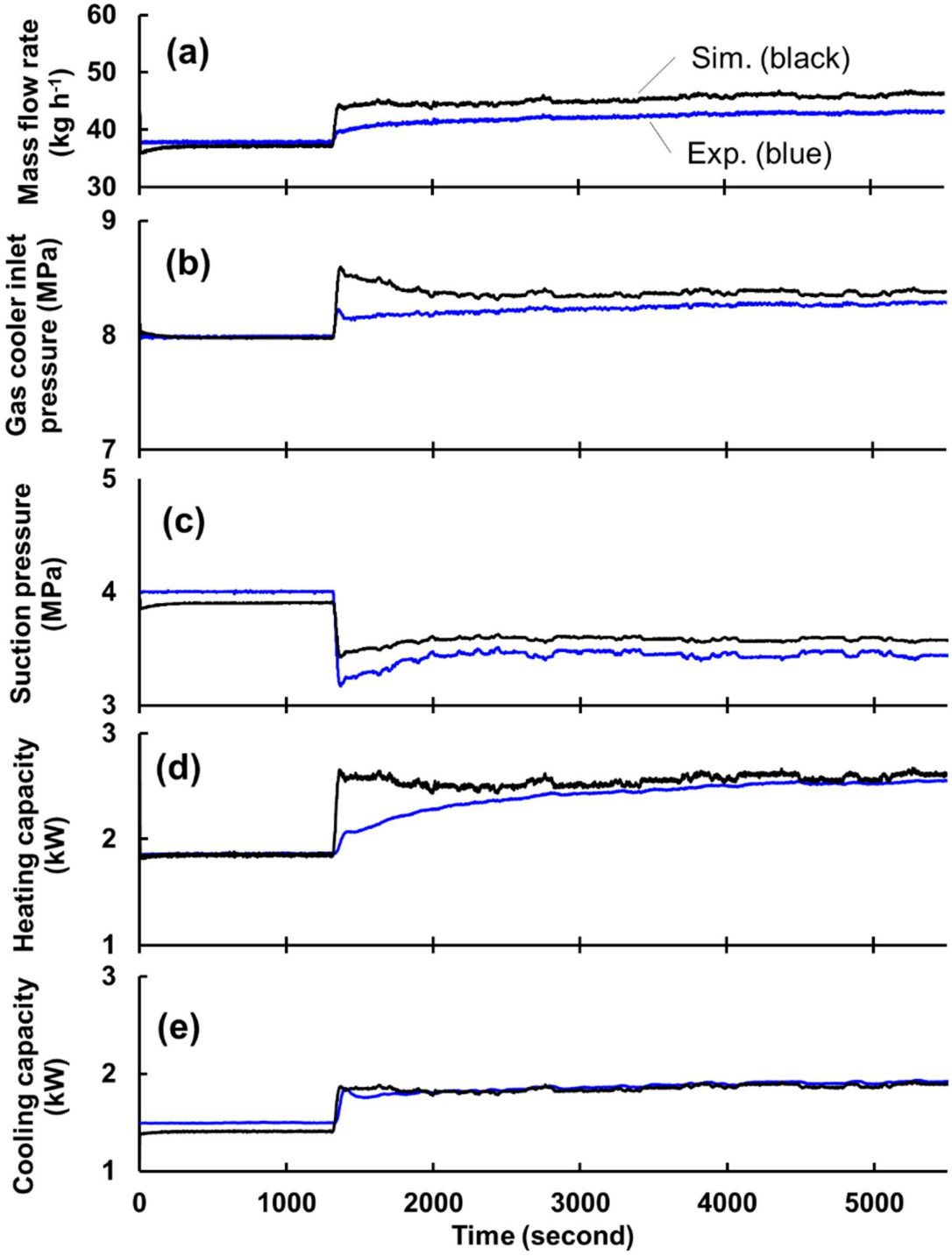

Figure 2.12. Comparison results when the rotational speed decreases; (a) mass flow rate, (b) gas cooler inlet pressure, (c) suction pressure, (d) heating capacity, and (e) cooling capacity (Ko et al., 2020).

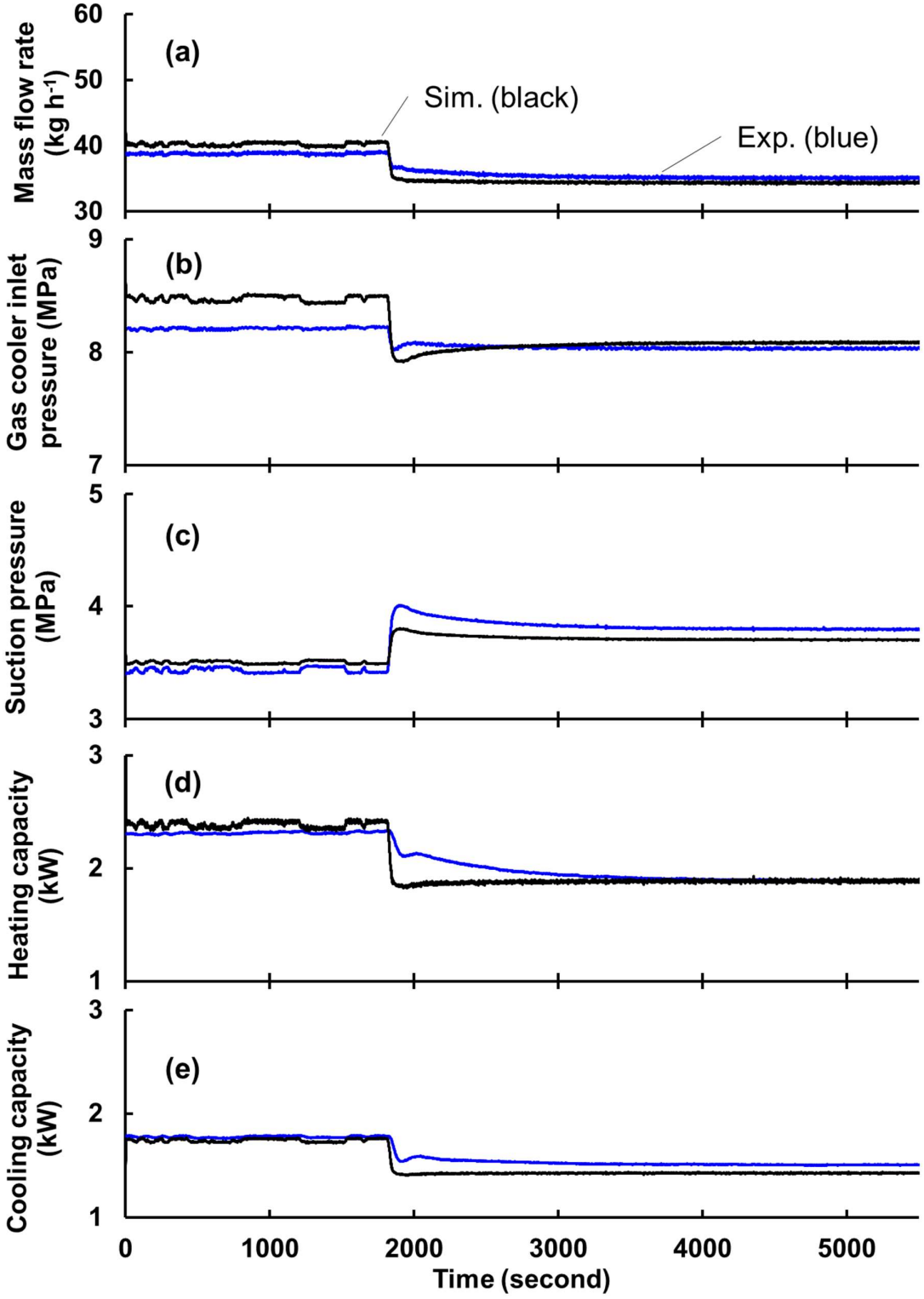

A similar transient experiment was conducted after replacing the scroll-type compressor with a rotary-type compressor (swept volume, 1.28 cm^3; maximum rotational speed, 70 rev s^{-1}). Figure 2.13 shows the rotational speed of the rotary compressor during an experiment. Other experimental conditions were fixed as follows: water flow rate at the gas cooler, 104.5 L h^{-1}; water temperature at the gas cooler inlet, 30 °C; water flow rate at the evaporator, 96.8 L h^{-1}; water temperature at the evaporator inlet, 21 °C; EEV opening step, 135. The refrigerant was charged 1.42 kg, the initial pressure and temperature were 6.6 MPa and 26 °C, respectively. The rotational speed data provided in Figure 2.13 was used for the input value in the simulation. Other simulation conditions are as follows: thermal reservoir temperature at the gas cooler, 31 °C; thermal reservoir temperature at the evaporator, 23.5 °C; orifice cross-sectional area, 0.22 mm^2. The initial pressure and temperature of the refrigerant were set to be the same value as that of the experimental data. Figure 2.14 compares the simulation results with the experimental data. The model well predicts the temporal tendency of the actual system. The simulation results show a faster response of the rotational speed increment than the experimental case, as the same with the comparison results (Figure 2.11 and Figure 2.12). A small jump appears on the system pressure, the temperature at the gas cooler inlet, and compressor power at 50 seconds; this is because the system's high-pressure side is just crossing the critical point during the computation. This small jump causes the fluctuation of the gas cooler heating capacity.

Figure 2.13. The rotational speed of the rotary-type compressor.

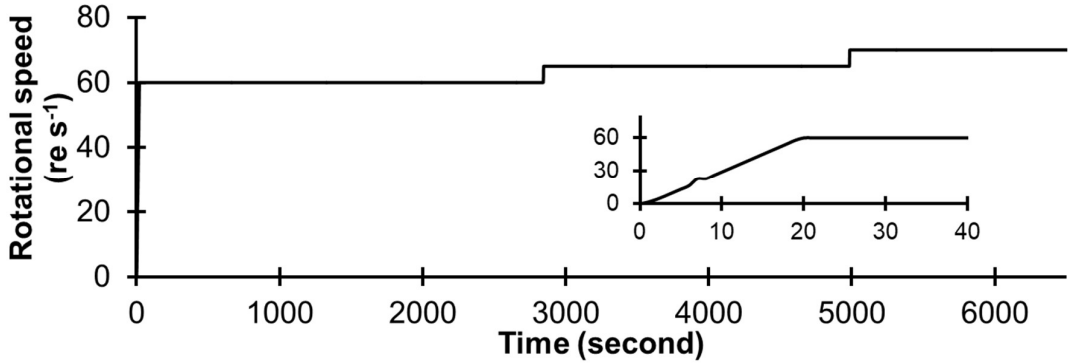

Figure 2.14. Comparison results; (a) pressures, (b) gas cooler inlet temperature, (c) mass flow rate, (d) suction superheating, (e) heating and cooling capacities, and (f) compressor power.

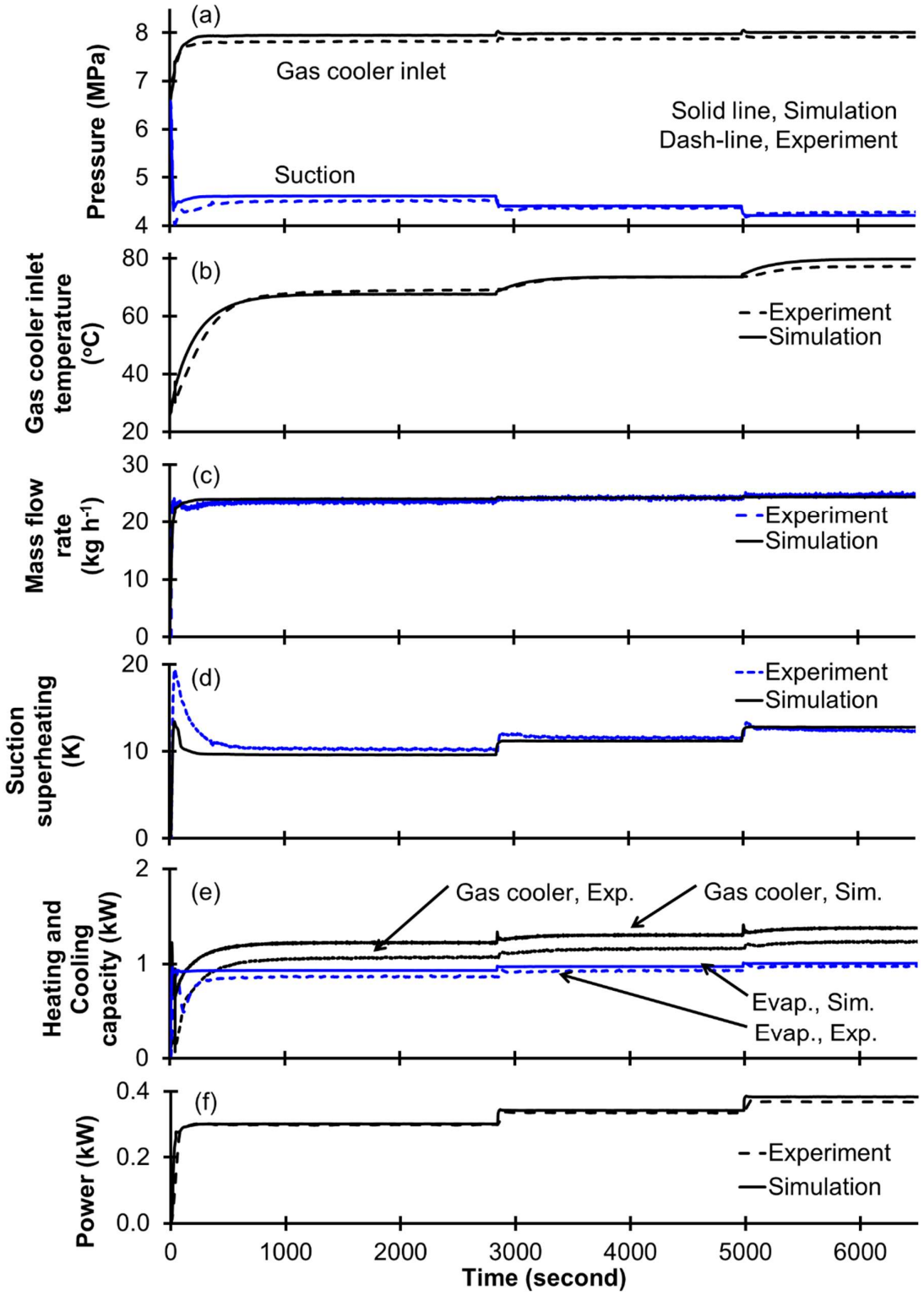

2.1.2 Air Handling Unit (AHU) and Cabin

The AHU and cabin models were established with the following assumptions (Ko et al., 2021b):

1. Moist-air is a homogeneous mixture that consists of moisture, dry air (N_2 of 78.12%, O_2 of 20.96%, and Ar of 0.92%), and carbon dioxide.
2. Moist-air flow is a one-dimensional and fully-developed flow.
3. The component of moist-air obeys the law of ideal gas and Dalton's law of partial pressures.
4. A thermophysical property of a moist-air mixture is uniform in a given control volume spatially.
5. The convective heat transfer coefficient of moist-air flow is calculated considering the properties of dry air only. Appendix A provides further description.
6. Heat gain or loss of the moist-air flow is neglected in this model since typical air supplying units used in passenger cars have a compact size, and the length of the air duct is short.
7. The pressure drop of the moist-air flow is not considered in this model.
8. The infiltration of the outdoor air into the cabin is not considered in this model.

A property of moist-air (ζ_{ma}) is decided by weighting the mass fraction (x^+) of each component as follows:

$$\zeta_{ma} = x_a^+ \zeta_a(T) + x_m^+ \zeta_m(T) + x_{co2}^+ \zeta_{co}\ (T), \tag{42}$$

$$1 = x_a^+ + x_m^+ + x_{co2}^+, \tag{43}$$

where a, m, and $co2$ represent the dry air, the moisture, and the CO_2. Properties of each component were obtained from Lemmon et al. (2018).

AHU

Figure 2.15a is a schematic of AHU. There are two inlets at the fan; one is for the return air from the cabin, and the other is for the fresh air from the outdoor. The opening degree of the first slab door (1) decides the proportion of the return air and the fresh air. If the

first slab door is fully open with direction to the outdoor, the AC operates for ventilation mode; otherwise, the AC operates for recirculation mode. The opening degree of the second slab door (2) regulates air temperature supplying into the cabin. The air departing from the evaporator faces the second slab door (2). When the second door closes the IHX-side passage, the air directly flows into the cabin. If the door is fully open with the IHX-side passage, the air heats up by absorbing thermal energy from the refrigerant in the IHX, and it flows into the cabin. A blend of air can be supplied into the cabin depending on the second slab door's opening degree. Figure 2.15b shows the model. Each HX replaces with a control volume representing the core volume of each HX

Figure 2.15. (a) schematic of AHU and (b) model.

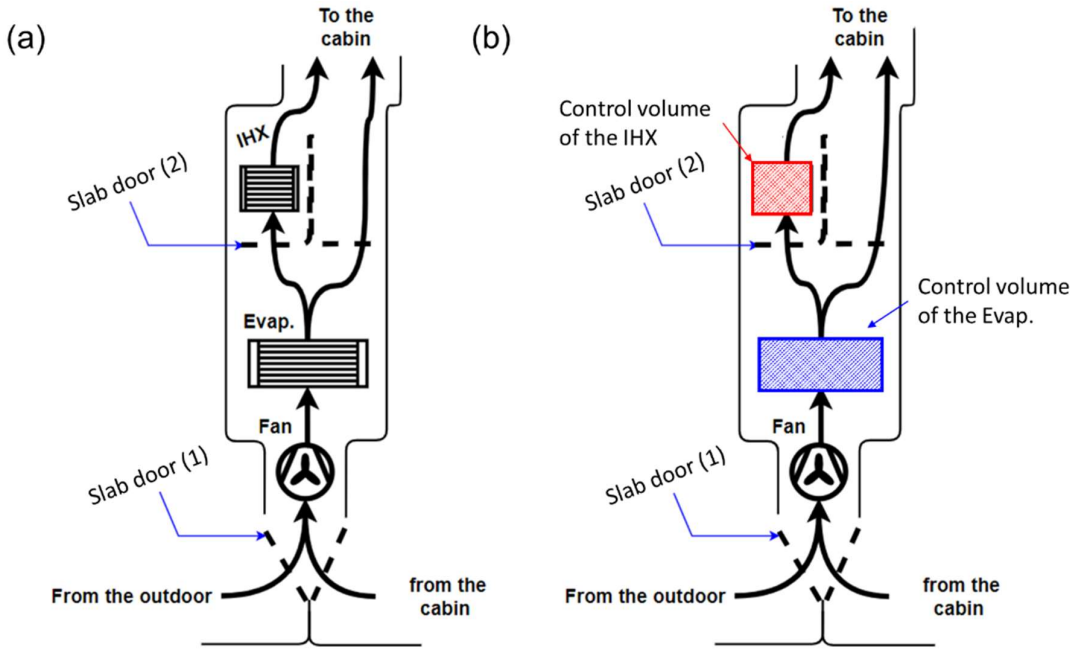

Moist-air Flow in HXs

Figure 2.16 depicts a schematic of the segment for moist-air flow. The model was established with the lumped parameter method with the following assumptions (Ko et al., 2021a; 2021b):

1. The conduction heat transfer by HX's solid body, fin and tubes, is neglected since the effect of this conductive heat transfer is relatively small compared to that of the convective heat transfer by moist-air and refrigerant flow.
2. Frost formation on the exterior surface of HX is ignored.

Figure 2.16. Segment for moist-air flow.

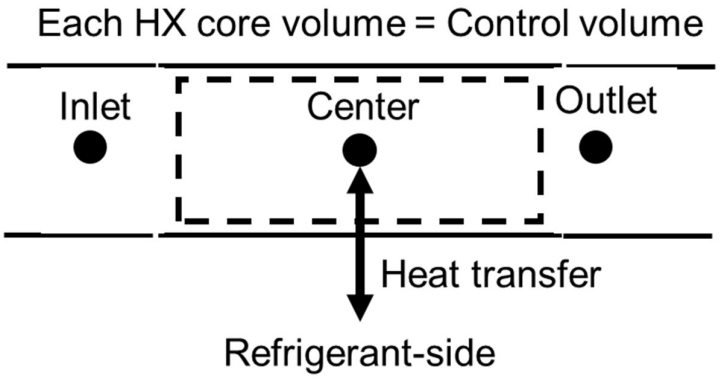

Mass conservation equations for the moist-air and moisture are given as follows:

Moist-air:

$$\frac{d\rho_{cen.ma}}{dt} V_{core} = \sum_i^o \dot{m}_{ma} + \dot{m}_{con.m}, \quad (44)$$

Moisture:

$$\frac{dx^+_{cen.m}}{dt} \rho_{cen.ma} V_{core} = \sum_i^o \dot{m}_m + \dot{m}_{con.m}. \quad (45)$$

Here, $\dot{m}_{con.m}$ represents the condensation rate of the vapor moisture, and it is calculated as follows:

$$\dot{m}_{con.m} = \begin{cases} 0, & if \;\; x^{+}_{cen.m} \le x^{+}_{cen.m.sat} \\ \frac{(x^{+}_{cen.m} - x^{+}_{cen.m.sat})\rho_{ma.cen} V_{core}}{\tau_{con}}, & if \;\; x^{+}_{cen.m} > x^{+}_{cen.m.sat} \end{cases}. \quad (46)$$

where τ_{con} represents the moisture condensation time constant, a constant value, 0.001 s, is used, which is provided in the used software as the default value. Energy conservation equations for the moist-air and moisture are given as follows:

Moist-air:

$$\rho_{cen.ma} C_{P.cen.ma} V_{core} \frac{dT_{cen}}{dt} = \sum_i^o \dot{m} \left(h^* + \frac{(Gv)^2}{2} \right)_{ma} + \dot{Q}_{con} + \dot{Q}_{ma}, \quad (47)$$

Moisture:

$$\rho_{cen.m} C_{P.cen.m} V_{core} \frac{dT_{cen}}{dt} = \sum_i^o \dot{m} \left(h^* + \frac{(Gv)^2}{2} \right)_{m} + \dot{Q}_{con}. \quad (48)$$

Here, $\dot{Q}_{con}$ and $\dot{Q}_{ma}$ are calculated as follows:

$$\dot{Q}_{con} = \dot{m}_{con.m} \left(h^*_{m.cen} - \Delta h^*_{vap} \right), \quad (49)$$

$$\dot{Q}_{ma} = hA \left(T_{cen} - T_{fin} \right) \cong hA (T_{cen} - T_{in.wall}), \quad (50)$$

where Δh^*_{vap} and $T_{in.wall}$ represent the specific enthalpy of vaporization of water and the inner wall temperature of the refrigerant-side. The heat transfer coefficient is decided by using a proper correlation depending on HX's shape. In the present study, a louver-fin flat-tubes HX is considered for the evaporator, OHX, and IHX. The air-side heat transfer coefficient is calculated as follows:

$$h = jRePr^{\frac{1}{3}} \left(\frac{k}{p_l} \right) \quad (51)$$

where j, Pr, and p_l represent Colburn j-factor, Prandtl number, and the louver pitch, respectively. The j-factor is calculated using the model of Park and Jacobi (2009).

Fan

A model of the fan was established with the following assumptions:

1. The fan is treated as a quasi-steady-state component, such as the compressor.
2. Heat gain or loss of the fan's body is neglected.
3. There is no irreversible loss.

Mass and energy conservation equations are given as follows:

$$\dot{m}_i = \dot{m}_o, \tag{52}$$

$$\dot{W}_{fan} = \dot{m}_i \sum_i^o \left(h^* + \frac{(Gv)^2}{2}\right), \tag{53}$$

where $\dot{W}_{fan}$ represents the fan power.

Damper

Figure 2.17 shows a schematic of damper models. Two valves represent a single slab door. The assumptions and governing equations for the valve models are the same as that used in the expansion device modeling; the different thing is that the working medium is moist-air. Thus, the description herein skips.

Figure 2.17. (a) the first slab door and (b) the second slab door models.

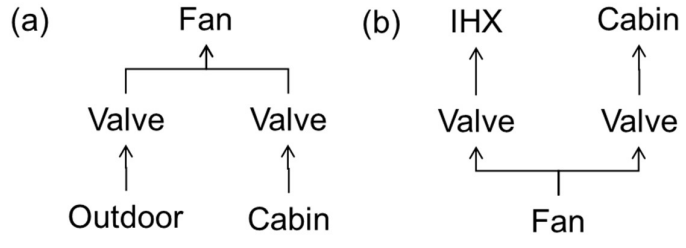

Cabin

Figure 2.18 describes a passenger car's cabin and model. The space and shape of a cabin vary with the type and size of vehicles; in most cases, the cabin consists of very complex geometric objects such as seats and a dashboard. Figure 2.18b depicts the cabin with a simple shape. The cabin space is framed with a roof panel, a windshield, side-windows, a rear window, and a vehicle body. Here, the vehicle body represents other remaining parts excepting the roof and windows, such as seats, dashboard, and frame. Figure 2.18c shows the control volume for the cabin.

Figure 2.18. (a) schematic of the cabin, (b) model, and (c) segment of the cabin (Ko et al., 2021b).

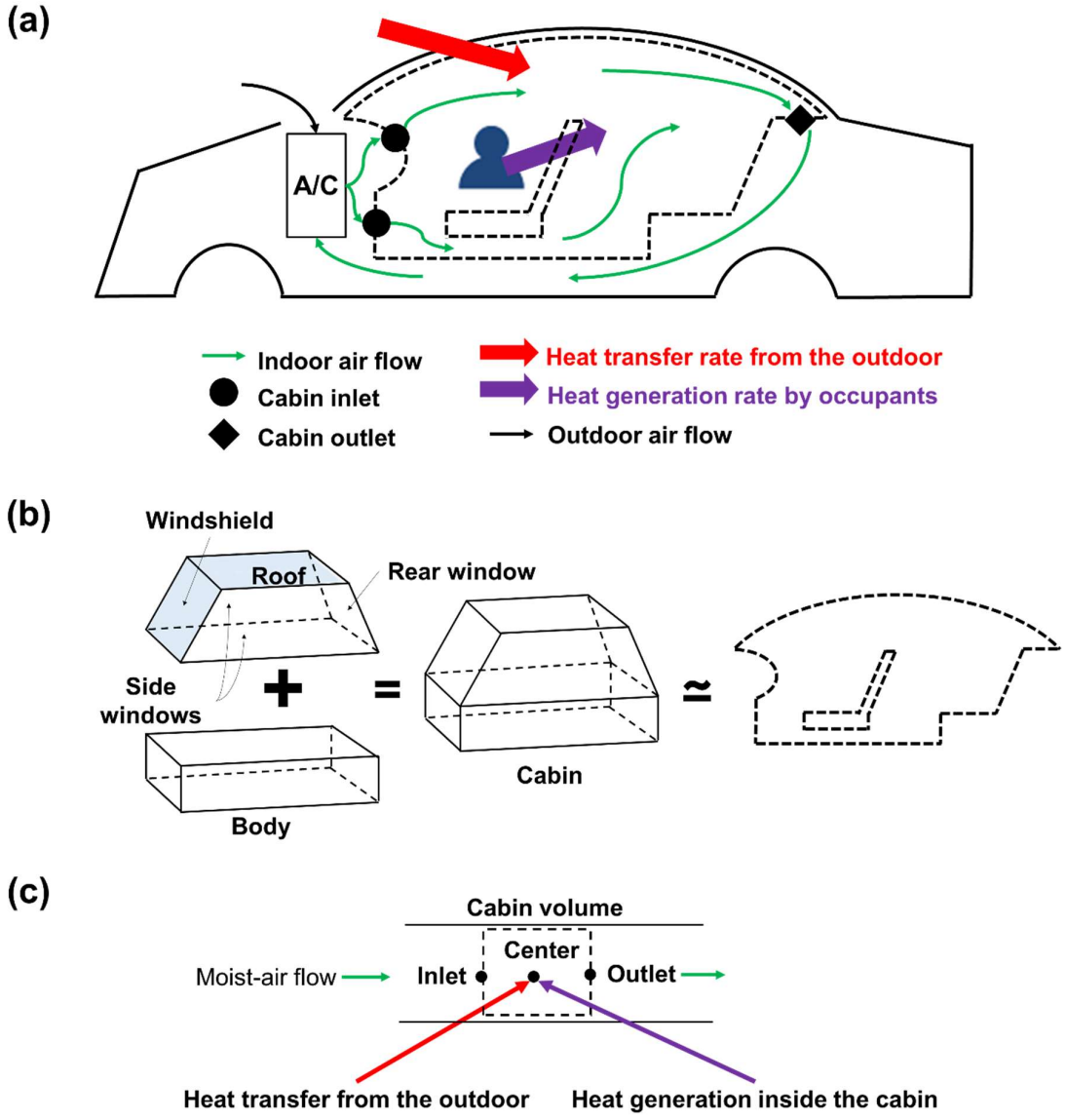

Mass conservation equations are given as follows:

Moist-air:

$$\frac{d\rho_{cen.ma}}{dt}V_{cabin} = \sum_i^o \dot{m}_{ma} + \dot{m}_{gen.m} + \dot{m}_{gen.co2}, \quad (54)$$

Moisture:

$$\frac{dx^+_{cen.m}}{dt}\rho_{cen.ma}V_{cabin} = \sum_i^o \dot{m}_m + \dot{m}_{gen.m}. \quad (55)$$

Carbon dioxide:

$$\frac{dx^+_{cen.co2}}{dt}\rho_{cen.ma}V_{cabin} = \sum_i^o \dot{m}_{co2} + \dot{m}_{gen.co2}, \quad (56)$$

The rate of moisture generation ($\dot{m}_{gen.m}$) and the carbon dioxide generation ($\dot{m}_{gen.co2}$) will be explained later. Energy conservation equations are given as follows:

Moist-air:

$$\rho_{cen.ma}C_{P.cen.ma}V_{cabin}\frac{dT_{cen}}{dt} = \sum_i^o \dot{m}\left(h^* + \frac{(Gv)^2}{2}\right)_{ma} + \dot{Q}_{od} + \dot{Q}_{occ.met} + \dot{Q}_{occ.lat} + \dot{Q}_{occ.co}\ , \quad (57)$$

Moisture:

$$\rho_{cen.m}C_{P.cen.m}V_{cabin}\frac{dT_{cen}}{dt} = \sum_i^o \dot{m}\left(h^* + \frac{(Gv)^2}{2}\right)_{m} + \dot{Q}_{occ.lat}, \quad (58)$$

Carbon dioxide:

$$\rho_{cen.co2}C_{P.cen.co2}V_{cabin}\frac{dT_{cen}}{dt} = \sum_i^o \dot{m}\left(h^* + \frac{(Gv)^2}{2}\right)_{co2} + \dot{Q}_{occ.co2}, \quad (59)$$

where $\dot{Q}_{od}$, $\dot{Q}_{occ.met}$, $\dot{Q}_{occ.lat}$, and $\dot{Q}_{occ.co2}$ represent the heat transfer rate from the outdoor, the heat generation rate by metabolism, the heat generation rate by the moisture in the exhaled gas, and the heat generation rate by the CO_2 in the exhaled gas, respectively.

The heat from the outdoor transfers into the cabin through each structure of a vehicle as follows:

$$\dot{Q}_{od} = \dot{Q}_r + \dot{Q}_{ws} + \dot{Q}_{sw} + \dot{Q}_{rw} + \dot{Q}_{body}, \tag{60}$$

The subscripts r, ws, sw, rw, and $body$ represent the roof, the windshield, the side windows, the rear window, and the vehicle body. Appendix B describes the heat transfer rate through each structure in detail.

In Eq. 57, $\dot{Q}_{occ.met}$, $\dot{Q}_{occ.lat}$, and $\dot{Q}_{occ.co2}$ are calculated as follows:

$$\dot{Q}_{occ.met} = N_{occ} q_{met} A_{occ}, \tag{61}$$

$$\dot{Q}_{occ.lat} = N_{occ} \dot{m}_{exh.m} h^*_{exh.m}(T_{occ}), \tag{62}$$

$$\dot{Q}_{occ.co2} = N_{occ} \dot{m}_{exh.co2} h^*_{exh.co2}(T_{occ}), \tag{63}$$

where N_{occ}, q_{met}, A_{occ}, $\dot{m}_{exh.m}$, $h^*_{exh.m}$, T_{occ}, $\dot{m}_{exh.co2}$, and $h^*_{exh.co2}$ represent the number of occupants, the metabolic rate, the heat transfer area of an occupant body, the rate of the exhaled moisture from the occupant, the specific enthalpy of the moisture, the temperature of the occupant, the rate of the exhaled CO_2 from the occupant, and the specific enthalpy of CO_2, respectively. $\dot{m}_{exh.m}$ and $\dot{m}_{exh.co2}$ are calculated as follows:

$$\dot{m}_{exh.m} = \dot{m}_{exh.a} \omega_{exh} = \left[\left(\frac{V_{tidal} N_{res} (1 - x^+_{exh.m})}{60} \right) \rho_{exh.a} \right] \omega_{exh}, \tag{64}$$

$$\dot{m}_{ex\ .co2} = \rho_{co2} x_{exh.co2} V_{tidal} N_{res}. \tag{65}$$

where $\dot{m}_{exh.a}$, ω_{exh}, $\rho_{exh.a}$, V_{tidal}, N_{res}, and $x^+_{exh.m}$ represent the mass of the exhaled dry air and the humidity ratio of exhaled air, the density of the exhaled dry air, the tidal volume, the respiratory rate (min^{-1}), and the moisture composition in the exhaled moist-air,

respectively. The adopted values for the calculations are provided in Table 2.5.

Table 2.5. Values used for the heat generation rate calculation (Ko et al., 2021b).

Variable	Value or Range	Reference
q_{met}, W m^{-2}	60 to 115 [a]	ANSI/ASHRAE Standard 55
A_{occ}, m^2	1.8	DuBois and DuBois (1945)
ω_{exh}, kg kg^{-1}	0.0316 [b, c]	Berry (1914)
$\rho_{exh.a}$, kg m^{-3}	1.138 [c]	Lemmon et al. (2018)
V_{tidal}, m^3	0.0005	Tortora and Derrickson (2018)
N_{res}, min^{-1}	12 to 18 [a]	Barrett et al. (2012)
$x_{exh.m}$, %	5.0 to 6.3 [a]	Dhami et al. (2015)
$x_{exh.co2}$, %	5	Dhami et al. (2015)

[a] The average value was adopted.

[b] The corresponding reference literature provides that the relative humidity (RH) of exhaled air of an occupant is about 78%, the corresponding humidity ratio is 0.0316 kg kg^{-1}.

[c] at 37 ^{o}C.

Validation

Figure 2.19 shows the AHU model. The air-side control volume in each HX is connected to the refrigerant-side. Heat transfer implements in this connection. Each separate control signal controls the opening degree of the two slab doors and the air flow rate, respectively. This AHU model is connected with the cabin model. Figure 2.20 describes the cabin model. Sky temperature and outdoor air temperature were set, the heat from the outdoor environment transfers to cabin air through the vehicle structures. Global irradiation intensity was set utilizing a signal. The heat generation rate and the carbon dioxide generation rate were also set up; the cabin space was connected with the AHU model.

Figure 2.19. AHU model.

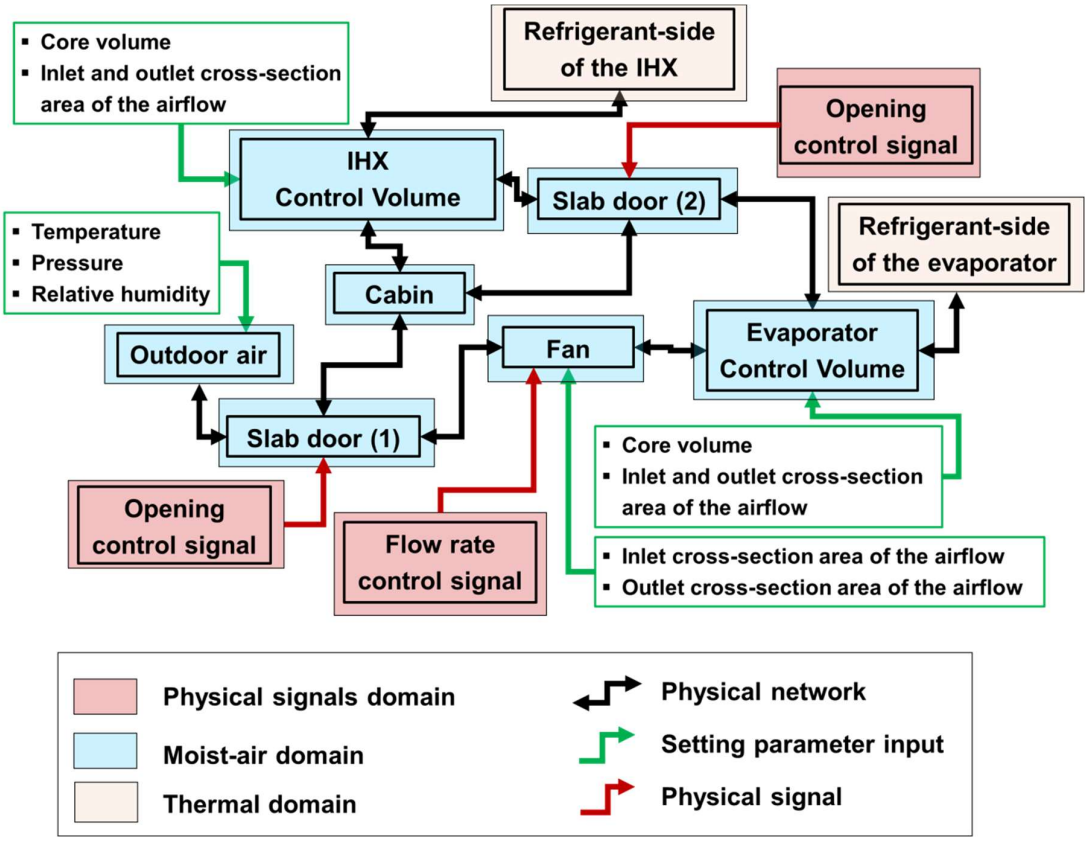

Figure 2.20. Cabin model.

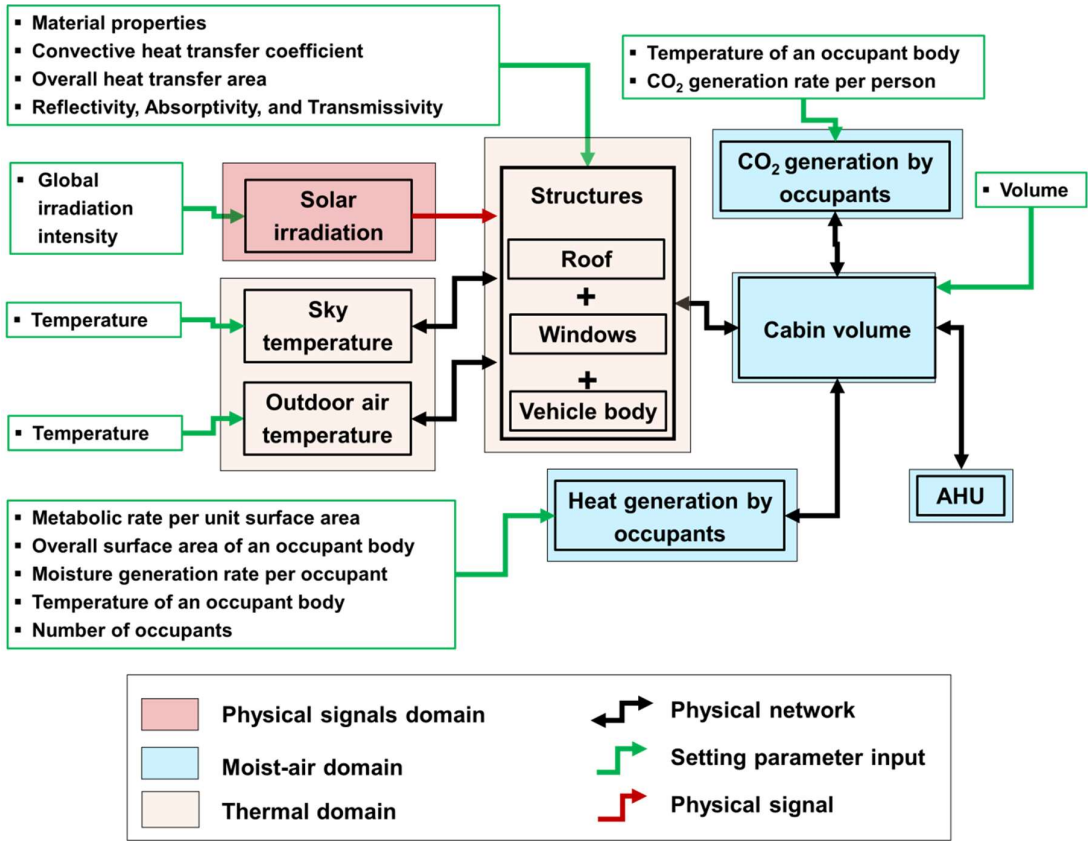

A set of simulations were carried out, and the simulation results were compared with the three different research articles (Marcos et al., 2014; Sanaye & Dehghandokht, 2011; Singh & Abbassi, 2018) to validate the AHU and cabin models.

Marcos et al. (2014) measured the cabin air temperature of a test car in three different conditions: (b) when the test car is parked outdoor, (c) when the test car is parked indoors, and (d) when the test car is driving on the road. These three tests were carried out in the AC being off. The outdoor temperature, solar irradiance intensity, and speed of the test vehicle varied with time during the tests. These three time-dependent variables were input into the present cabin model. The sky temperature was set to be the fixed value, 16.12 ºC (Karn et al., 2019), and this value was determined based on the time and date of each test conducted by Marcos et al. (2014). The RH of the outdoor and cabin air is not provided in the reference literature, and it was assumed to be 50% for the present simulation. Also, the cabin volume was assumed to be 3.2 m^3 (1.8×1.1×1.63 m^3), based on the given dimensions in the literature. The properties of the windows, roof, and vehicle body of the test car (Marcos et al., 2014) were used as input values for the present validation. The equivalent heat transfer area of 6 m^2 (Marcos et al., 2014) and the heat capacity of 144.24 kJ K^{-1} (Marcos et al., 2014) were set for the vehicle body. The initial temperature of the cabin air was set to be the same value as that of each case from the literature. The initial RH of the cabin air was assumed to be 50% since it is not provided in the reference. Figure 2.21a shows the locations of the temperature sensors installed inside the test car cabin (Marcos et al., 2014). Figure 2.21b, c, and d compare the calculated temperature against the measured temperature for each case. Figure 2.21b compares the calculated cabin temperature with the measured data, for the case that the car is parked outdoor. From the experimental data, a temperature distribution inside the test car cabin is observed. The comparison result shows that the present model has a good agreement with the experimental data. The calculated temperature lies within the measured temperature range. For the cases in Figure 2.21c and d, the reference provides the measured temperature at point 5 only. Figure 2.21c compares the cabin temperature when the car is parked indoors (i.e., without the solar irradiation impact). The simulation result shows a fast-declining tendency of the temperature than the measured value; however, it presents that the current model predicts the measured temperature well a maximum deviation (ΔT_{max}) of 1 ºC. Figure 2.21d compares the cabin temperature when the car is driving. The cabin temperature of the test car increases to 20.8 ºC, 2 minutes after the test starts. Then it gradually increases and reaches 23.5 ºC. According to the explanation in the reference, the peak of the measured temperature in the initial stage is due to the occupant's boarding. The present model shows a

similar behavior during the initial 2 minutes. Furthermore, the model well predicts the measured temperature within a maximum deviation of 1.2 ºC throughout the whole simulation time. In these three cases, the simulation results show a faster trend than the measured data (Marcos et al., 2014). The is due to the calculated heat transfer rate of the cabin air on the vehicle body section. The vehicle body (seats and dashboard) has a very complex geometry in an actual vehicle, it is difficult to determine the characteristic length for the convection heat transfer coefficient (h_{body}) calculation. Reynolds number or Rayleigh number varies depending on the decided characteristic length so the evaluated h_{body} also changes greatly. From several simulations, it was confirmed that the temporal tendency of the cabin temperature changes sensitively depending on the value of h_{body} then the coefficient value was adjusted to be 18 W m^{-2} K^{-1} for the best prediction result for satisfying all cases. This type of variable is typically treated as an empirical variable. So, if necessary for a specific purpose, it is possible to obtain a suitable value from experimental data and use it to tune the simulation model. Meanwhile, despite this limitation, the prediction of the present model shows a good agreement with the tendency of the literature data (Marcos et al., 2014).

Figure 2.21. Comparison with the data from Marcos et al. (2014); (a) locations of the temperature sensors inside the test car, (b) when the test car is parked outdoor, (c) parked indoor, and (d) driving (Ko et al., 2021b).

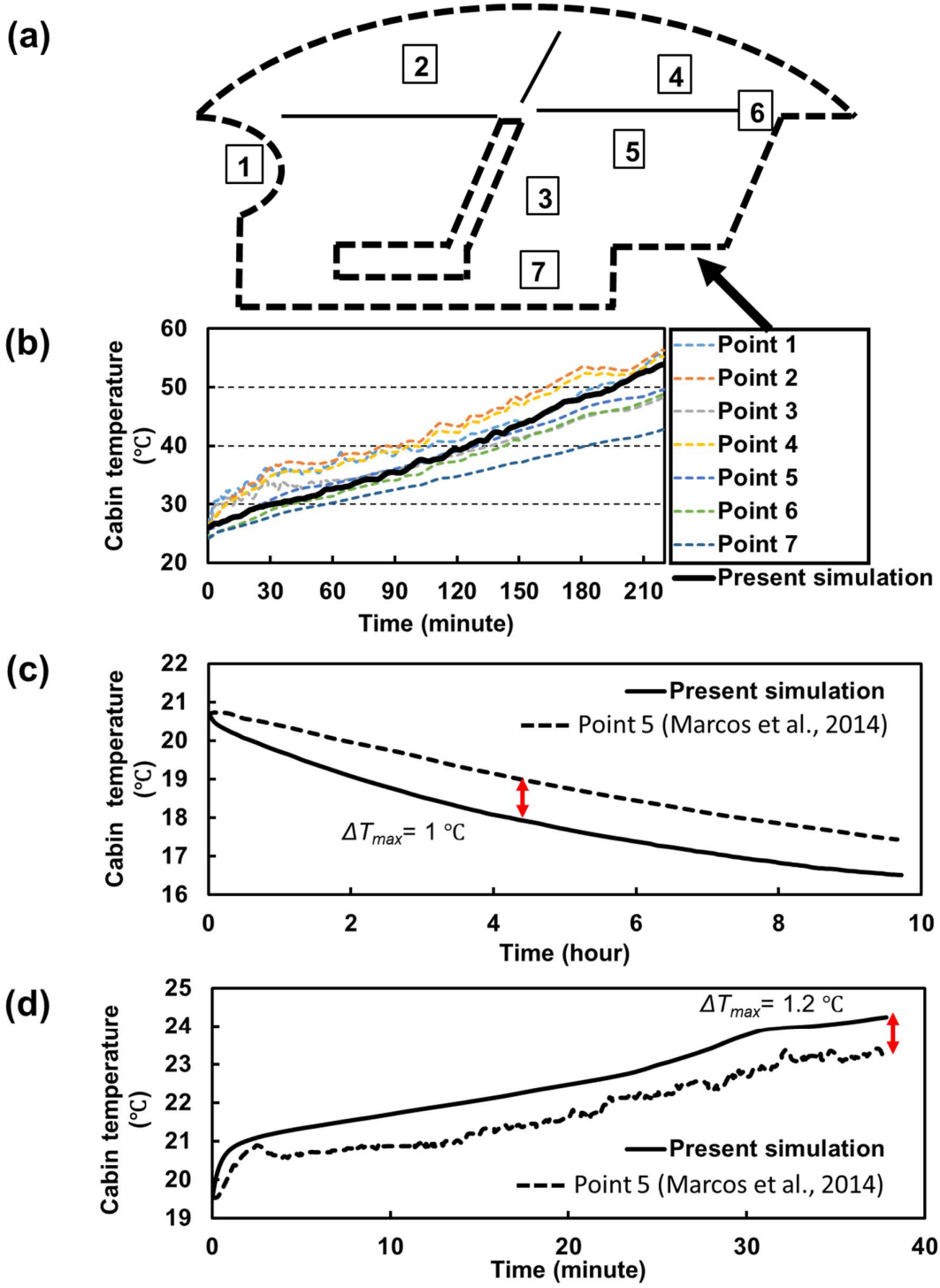

Sanaye and Dehghandokht (2011) measured the cabin air temperature of a test automobile when the AC operates. The test car is located inside a climate test facility and no one is in the vehicle cabin ($2.3\times1.3\times1.19$ m^3). During the test, the ambient air temperature and the radiation heating panel were kept at 43 ^oC and 1.2 kW, respectively, and the mean velocity of the ambient airflow was varied with time. These three values were used as input values to the present model. Figure 2.22 compares the calculated cabin temperature with the measured temperature. The test vehicle cabin's air temperature is cooled down for 15 minutes from the initial temperature, 60 ^oC, reaches 25 ^oC after 30 minutes, then it maintains until 85 minutes. After the AC is off at 85 minutes, the test car cabin temperature gradually increases to 38.7 ^oC. The literature does not provide the specifications of the test vehicle cabin structures, AC, as well as operating conditions; thus, the same specification of the cabin structures as that of Marcos et al. (2014) was adopted for the present simulation. The operating conditions of the AC, the temperature, and flowrate of the supplying air to the cabin were adjusted to meet the cabin temperature, 25 ^oC, at the 85 minutes in the present simulation. From Figure 2.22, the present model shows a similar temporal behavior with the literature data, over 145 minutes. A fast prediction with the time-dependent tendency of the measured cabin temperature is observed again as observed in Figure 2.22, consistently, so a maximum discrepancy of 8 ^oC is observed in the pull-down operation period. This can be explained that the present simulation was conducted using the same properties of the cabin structure of Marcos et al. (2014) since the literature (Sanaye & Dehghandokht, 2011) does not provide. After 10 minutes, the model precisely predicts the cabin temperature in a quasi-steady-state condition. When the AC stops at 85 minutes, the result shows the fast response again then the temperature gradually increases by following the curve of the measured temperature.

Figure 2.22. Comparison with the data from Sanaye and Dehghandokht (2011) (Ko et al., 2021b).

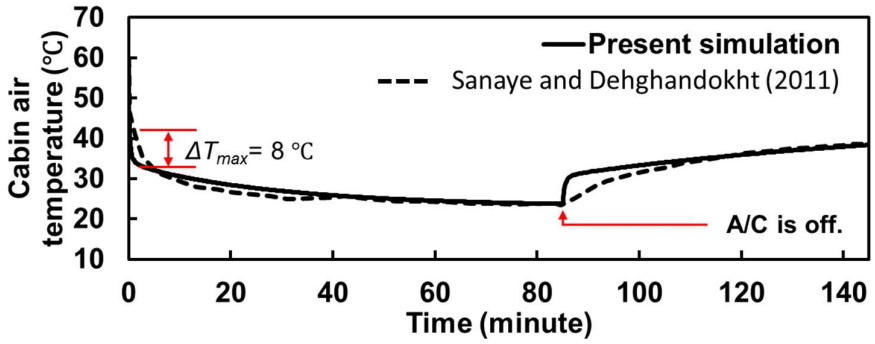

Singh and Abbassi (2018) conducted a 1D/3D-CFD co-simulation of AC (1D) for cooling the cab of off-highway machinery (3D-CFD). The literature provides the humidity ratio of the moist-air at the evaporator inlet and outlet during 1800 seconds of the cabin pull-down operation. The return air from the cabin mixed with the outdoor air, and this blend air supplies into the cabin passing through the evaporator (Singh & Abbassi, 2018). The CFD simulation was carried out at an ambient temperature of 43 °C, an ambient relative humidity of 32%, an ambient convective heat transfer coefficient of 5 W m^{-2} K^{-1}, a solar load of 950 W m^{-2}, and an initial humidity ratio of 18 g kg^{-1} inside the AHU (Singh & Abbassi, 2018). These given conditions were used for the present simulation as input values. On the other hand, the specification AC used, cabin volume, and operating conditions are not provided in the article (Singh & Abbassi, 2018). Thus, the cabin structures and volume from Marcos et al. (2014) were adopted for the present simulation. The evaporator operating temperature and the airflow rate were adjusted to achieve as similar with the transient behavior of humidity at the evaporator inlet from Singh and Abbassi (2018). As a result, the humidity ratio at the evaporator inlet of 1 g kg^{-1} larger value was set. Figure 2.23a compares the humidity ratio at the evaporator inlet and outlet, respectively, with the literature data. The maximum deviation of 5 g kg^{-1} is observed for the initial 80 seconds at the evaporator outlet due to the difference in the size of the cab and evaporator as well as the operating conditions. However, the results show that the present model well predicts the temporal behavior of the humidity ratio of the moist-air. The present model over-estimates the humidity ratio of the results of the original literature at the evaporator outlet within a deviation of 1 g kg^{-1}, except for the initial 80 seconds. This is because the humidity ratio at the evaporator inlet was set to be 1 g kg^{-1} larger value. Figure 2.23b shows the humidity ratio difference between the evaporator inlet and outlet. The present model well predicts the humidity ratio difference between at the inlet and outlet; here, this difference of humidity ratio can be regarded as the amount of moisture condensation at the evaporator where the dehumidification occurs. From Figure 2.23b, the present model well predicts the temporal tendency as well as the value within an error of 1.2 g kg^{-1}. This maximum value of the deviation is observed from 40 seconds to 80 seconds. In that period, the value of the humidity ratio calculated at the evaporator inlet is almost the same as that of the reference (Singh & Abbassi, 2018). However, the value of the humidity ratio calculated at the evaporator outlet is larger than that of the reference (Singh & Abbassi, 2018). Since the difference of the specification used for the cabin and evaporator, the deviation is observed in the initial pull-down period. Also, the moisture condensation at the evaporator is delayed. Despite those discrepancies with the literature data (Singh & Abbassi,

2018), the results show that the present model obeys physical common sense and can implement moisture condensation.

Figure 2.23. Comparison with the CFD simulation data from Singh and Abbassi (2018); (a) humidity ratio at the evaporator inlet and outlet and (b) humidity ratio difference between the evaporator inlet and outlet (Ko et al., 2021b).

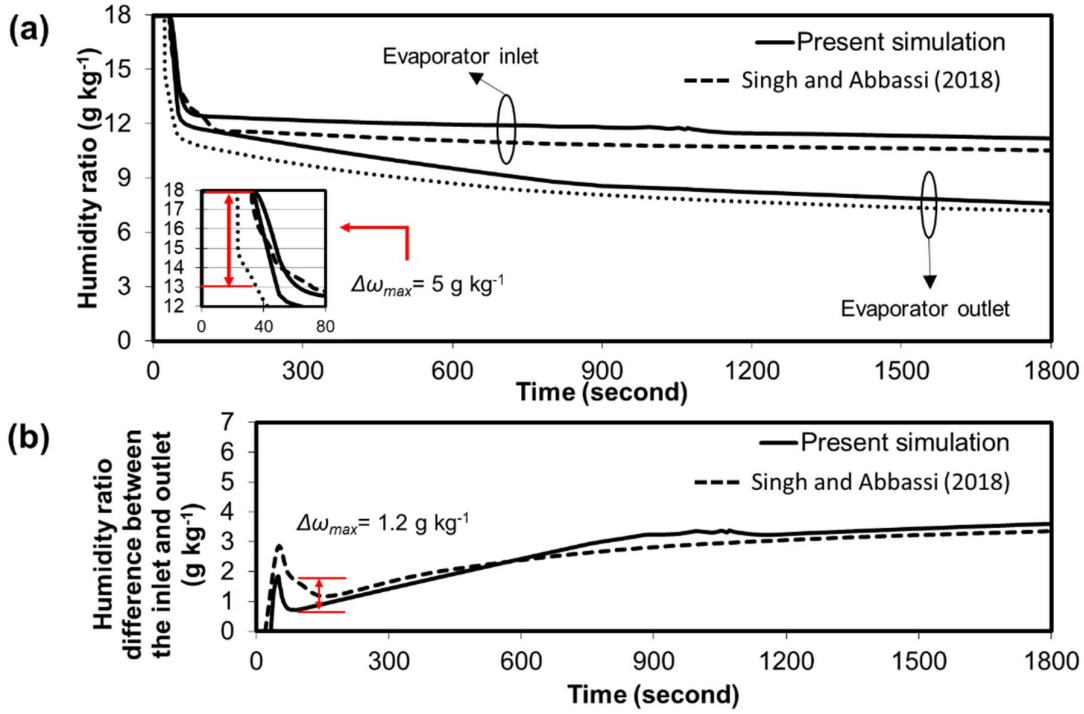

2.2 Simulations

2.2.1 System Description

Figure 2.24 shows a schematic of an AC studied. The VCS consists of a compressor (Comp.), an IHX, an OHX, an expansion valve (Ex. valve), an evaporator (Evap.), and an IntHX. In the IHX and OHX, the refrigerant rejects the heat to the air flow in the AHU and outdoor, respectively. In the IntHX, heat exchanges between the refrigerant at the high-pressure side and the refrigerant at the low-pressure side. In the evaporator, the refrigerant absorbs the heat from the airflow in the AHU. Specifications of the components considered are provided in Table 2.6. The major components (Comp., OHX, Evap., and IHX) were taken from the three research articles (Wang et al., 2018b; Yin et al., 2001; Jin et al., 2011). The literature (Wang et al., 2018b) studied an automobile R-744 VCS, and others (Yin et al., 2001; Jin et al., 2011) investigated a louver-fin HX using R-744 as a working fluid. The research article (Wang et al., 2018b) provides the specification of an electric compressor and buffer, but it does not provide the detailed dimensions of the used air-to-refrigerant HXs; it just provides the information of width, length, and depth of the HXs used. The other two documents (Yin et al., 2001; Jin et al., 2011) provide the detailed dimensions of the HXs used, respectively. A louver-fin HX used as a gas cooler in Yin et al. (2001) has a similar size to the OHX used in Wang et al. (2018b), and a louver-fin HX used as an evaporator in Jin et al. (2011) has a similar size to the evaporator used in Wang et al. (2018b). Hence, each louver-fin HX from Yin et al. (2001) and Jin et al. (2011) was used for the OHX and the evaporator, respectively, in the present study.

The outdoor air, the recirculation air, or the blended air is intake into the AHU depending on the first damper location (Damper 1). The intake air is cooled by rejecting the heat to the refrigerant at the evaporator. Then, this cool-air flowing path is decided by the second damper (Damper 2) position; the cool-air is supplied into the cabin directly, or the air with moderate temperature is supplied to the cabin after the part of the cool-air is reheated passing through the IHX and blended with the remaining cool-air. The indoor air recirculates while the vent is closed, and the indoor air is exhausted to the outdoor when the vent is open.

Figure 2.24. Schematic of the AC (Ko et al., 2021b).

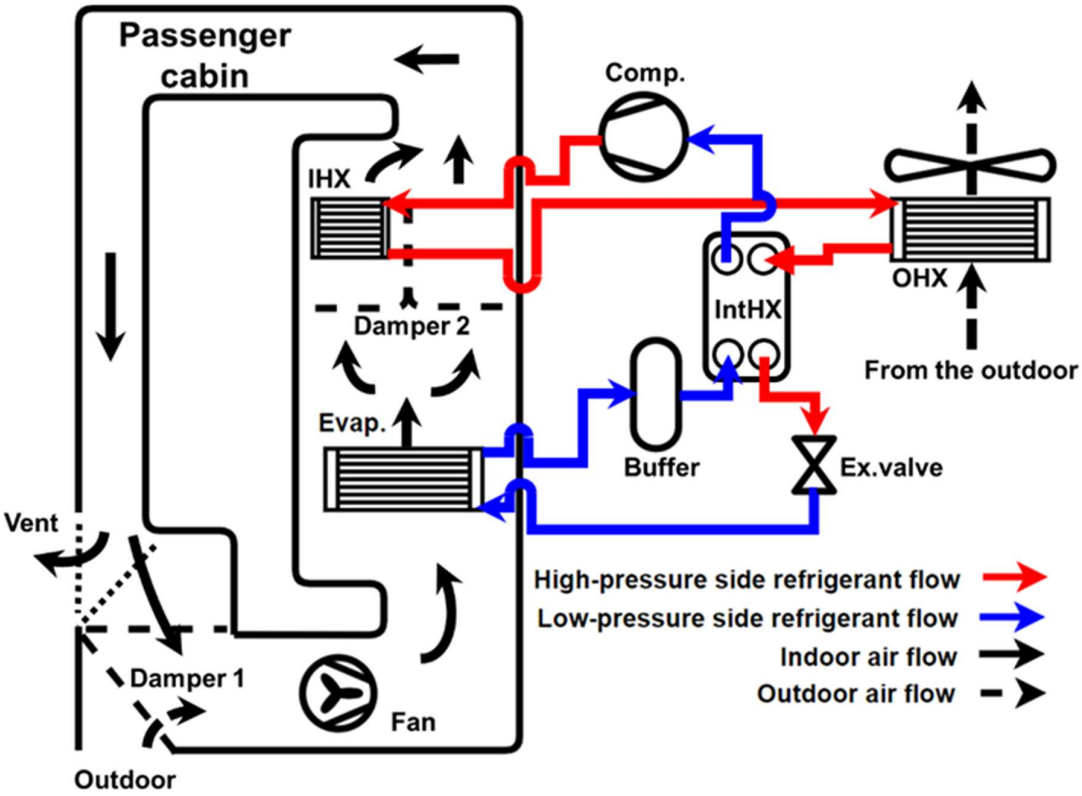

Table 2.6. Specification of the components (Ko et al., 2021b).

Component	Specification
Comp. (Wang et al., 2018b)	Electric-driven; Rotary-type; Swept volume, 6.8 cm^3; Maximum rotational speed, 8000 rev min^{-1}
OHX (Yin et al., 2001)	Louver-fin HX; Refrigerant-side heat transfer area, 0.49 m^2; Air-side heat transfer area, 5.2 m^2; Mass, 2.3 kg; Face area, 1950 cm^2; Core depth, 1.65 cm; Core volume, 3320 cm^3
Evap. (Jin et al., 2011)	Louver-fin HX; Refrigerant-side heat transfer area, 0.2726 m^2; Air-side heat transfer area, 2.47 m^2; Mass, 1.294 kg; Face area, 435 cm^2; Core depth, 4.31 cm; Core volume, 1950 cm^3
IHX	Louver-fin HX (half-size of the used evaporator); Refrigerant-side heat transfer area, 0.136 m^2; Air-side heat transfer area, 1.24 m^2; Mass, 0.647 kg; Face area, 435 cm^2; Core depth, 2.16 cm; Core volume, 975 cm^3
IntHX	Plate-type; Heat transfer area, 0.03 m^2
Ex. valve	Operating range of the degree of openness of the orifice cross-sectional area, 0 to 1.76 cm^2
Buffer (Wang et al., 2018b)	Inner volume, 1 L

Figure 2.25 shows a diagram of the integrated model. The input values are as follows: the geometric dimensions of the cabin and components of the VCS, the heat sources in the cabin, the outdoor environmental conditions, and the initial conditions (pressure, temperature, and RH of air inside the cabin and AHU, and the pressure and temperature of the refrigerant in the VCS).

Figure 2.25. Model diagram (Ko et al., 2021b).

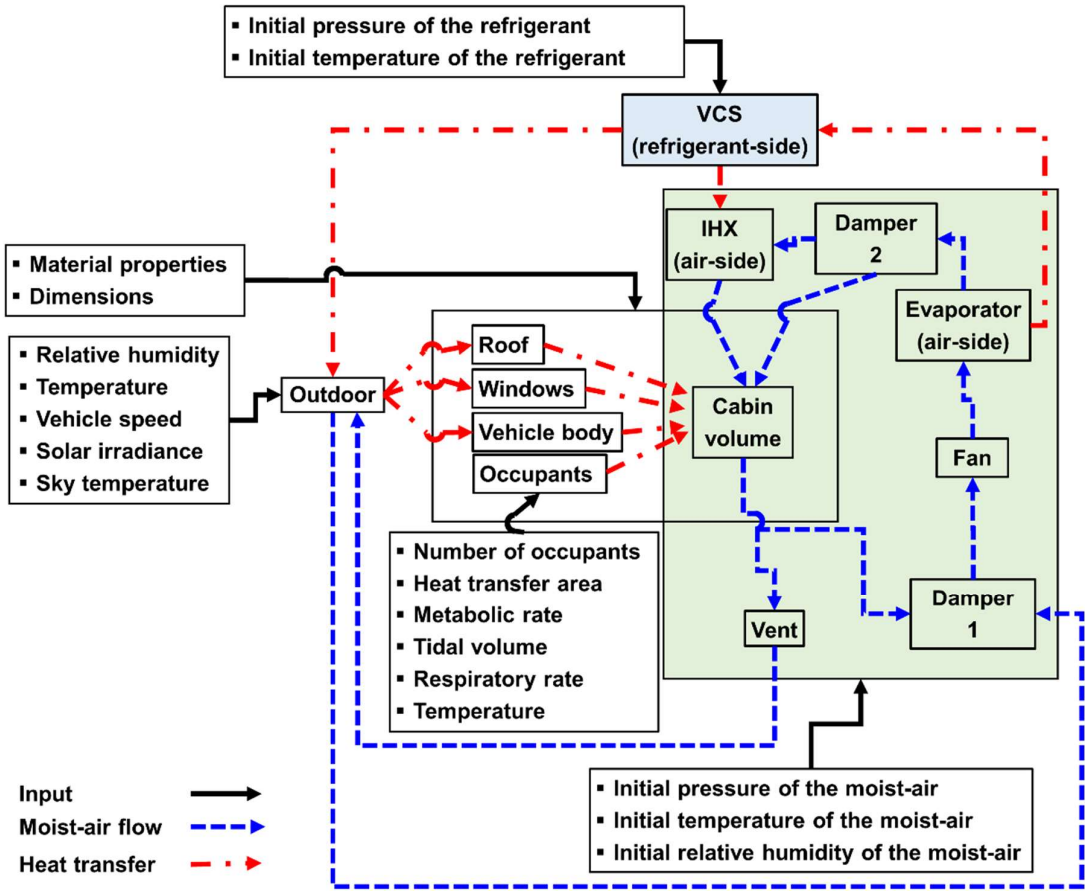

Figure 2.26 shows a schematic of an air-to-refrigerant HX and model. In Figure 2.26a, the refrigerant enters one of the headers and is distributed to each tube, assuming a uniform mass distribution. The louvered-fin is between the tubes, the moist-air and refrigerant flow perpendicularly to each other. Figure 2.26b describes the HX model. A unit segment for the refrigerant flow is assigned to a single flat-tube, and a unit segment for the moist-air flow is assigned to the core volume of the HX for the moist-air flow. The heat transfer coefficient of the refrigerant flow is calculated in the refrigerant side control volumes, the heat transfer coefficient of moist-air flow is calculated in the moist-air side segment, respectively. All the nodes, named the inner wall in the refrigerant side, are connected to the moist-air segment, heat transfer is implemented through that connection. Here, the heat transfer occurs from a higher temperature medium to a lower temperature medium based on given temperatures.

Figure 2.26. (a) schematic of a louvered-fin flat-tubes HX and (b) the model (Ko et al., 2021b).

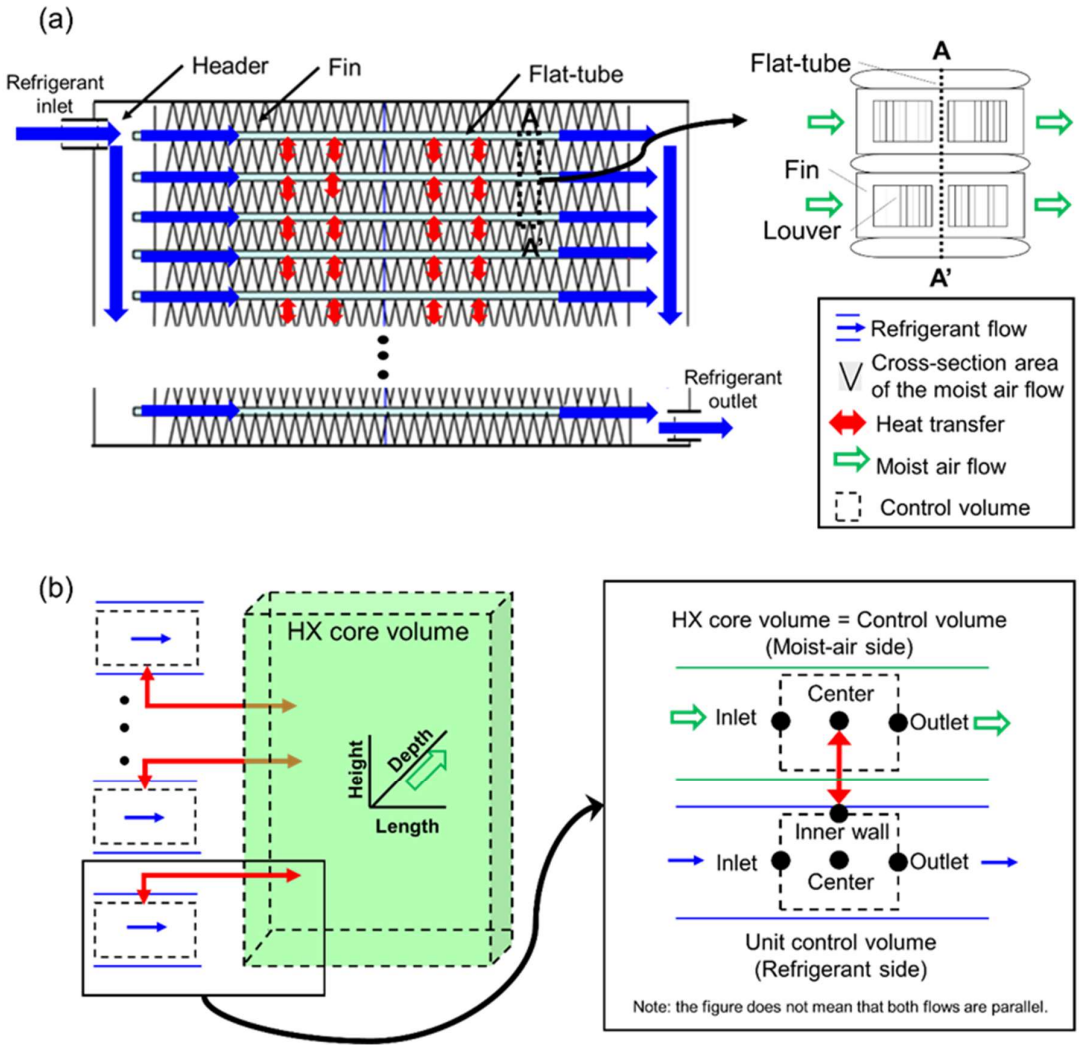

Figure 2.27a shows the local heat transfer coefficient of the transcritical refrigerant flow against the temperature. When the size ratio is less than 0.13, the simulation shows a good agreement of the local heat transfer coefficient tendency. Since the size ratio is over 0.17, the model is hard to capture the local heat transfer coefficient variation along the tube near the pseudocritical temperature. Figure 2.27b shows the average heat transfer coefficient. When the size ratio decreases, the average heat transfer coefficient converges to a specific value; in this case, it reaches 2 kW m^{-2} K^{-1}. It is observed that there is no significant difference in the average heat transfer coefficients. The maximum relative deviation between the average heat transfer coefficients is 17%.

Figure 2.27. (a) local heat transfer coefficient and (b) the average heat transfer coefficient.

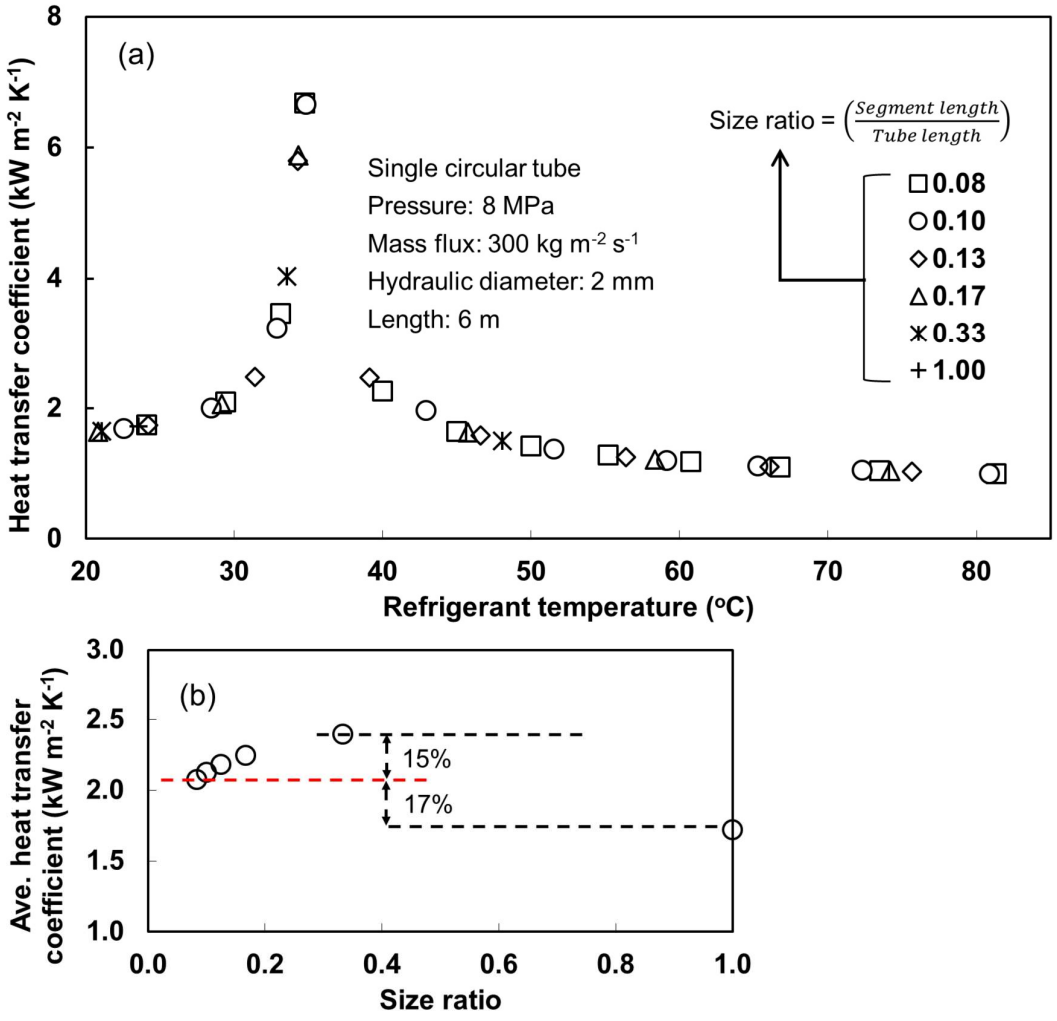

The number of segments for each HX was decided considering that system-level simulations aim to predict behavior and performance, not such specific phenomena in a system's components. For example, the original HX (Yin et al., 2001) used as the OHX in the present study consists of 34 flat-tubes with three refrigerant passages in a single slab, and each flat-tube consists of 11 microchannels. When a single segment assigns to each microchannel, the number of total segments becomes 374 (34 by 11); this number of segments is too many, so it takes too much time for computation. A multi-channels flat-tube was modified to a single-channel circular tube to decrease the time-cost, as shown in Figure 2.28; the hydraulic diameter of the modified tube was assumed to be 2 mm based on the given refrigerant-side heat transfer area of the reference literature. Thus, each tube length was decided to be 2.3 m. Then, a single segment was assigned to the single flat-tube in the modified OHX. This same approach was adopted for the evaporator and IHX. Table 2.7 provides the dimensions of refrigerant channels in each HX model and the number of total segments.

Figure 2.28. Modifying refrigerant channel shape.

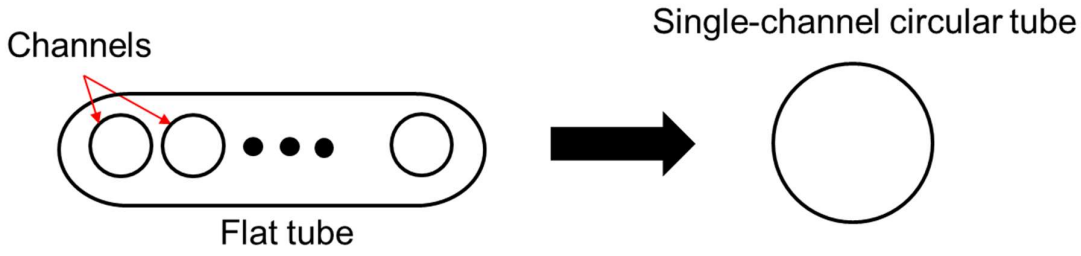

Table 2.7. Dimensions of refrigerant channels in each HX of the model.

HX		Original	Modified
OHX	The number of tubes	34	34
	The number of channels per tube	11	1
	The number of segments	374	34
	Hydraulic diameter of a channel	0.79 mm	2 mm
	Channel length (i.e., segment length)	0.545 m	2.3 m
Evap.	The number of tubes	46	46
	The number of channels per tube	13	1
	The number of segments	598	46
	Hydraulic diameter of a channel	0.79 mm	2 mm
	Channel length (i.e., segment length)	0.192 m	0.94 m
IHX	The number of tubes	23	23
	The number of channels per tube	13	1
	The number of segments	299	23
	Hydraulic diameter of a channel	0.79 mm	2 mm
	Channel length (i.e., segment length)	0.192 m	0.94 m

2.2.2 Conditions

Figure 2.29 shows the control logic for the compressor, expansion valve, and evaporator airflow rate. The compressor, expansion valve, and evaporator airflow rate are controlled respectively to meet each setpoint value during the start-up and cabin pull-down operation. The compressor rotational speed (S_{comp}) was controlled within 0 rev min^{-1} to 8000 rev min^{-1} to meet the set evaporator temperature ($T_{evap.ref}$). The orifice cross-sectional area of the expansion valve ($A_{c.ori}$) was controlled to fulfill the set suction superheating (ΔT_{sup}). To satisfy the target cabin temperature (T_{cabin}), the moist-air flow rate ($\dot{V}_{ma}$) in the AHU was controlled in the range of 0 m^3 s^{-1} to 0.5 m^3 s^{-1}. The rotational speed, cross-sectional area, and airflow rate were controlled using the PI method. The proportional and integral coefficients of each PI-controller were auto-tuned utilizing 'PID Tuner' in Simulink.

Figure 2.29. (a) compressor rotational speed, (b) orifice cross-sectional area of the expansion valve, and (c) moist-air flow rate in the AHU (Ko et al., 2021b).

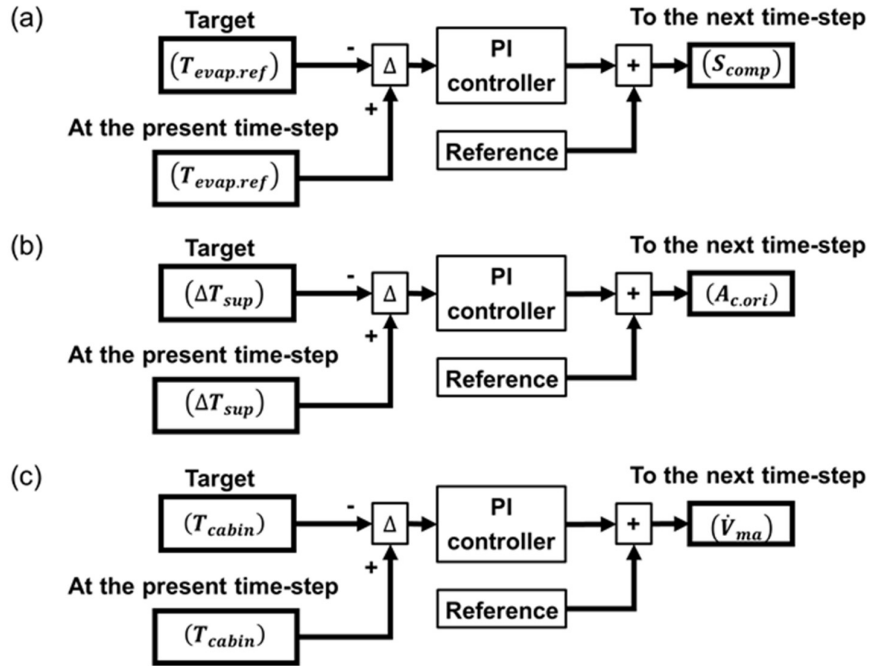

Figure 2.30 shows the compressor rotational speed in the early start-up stage. This time-dependent profile of the speed was used as an input value. After 5 seconds, when simulations start, the compressor starts its operation. The speed rises to 6000 rev min^{-1}, at 10 seconds, the system switches the compressor operation to PI control. As the moisture-air flow source in the AHU, the fan model starts its operation at 5 seconds, and the PI control activates simultaneously. The expansion valve operates under PI control over the simulation time.

Figure 2.30. Compressor rotational speed input (Ko et al., 2021b).

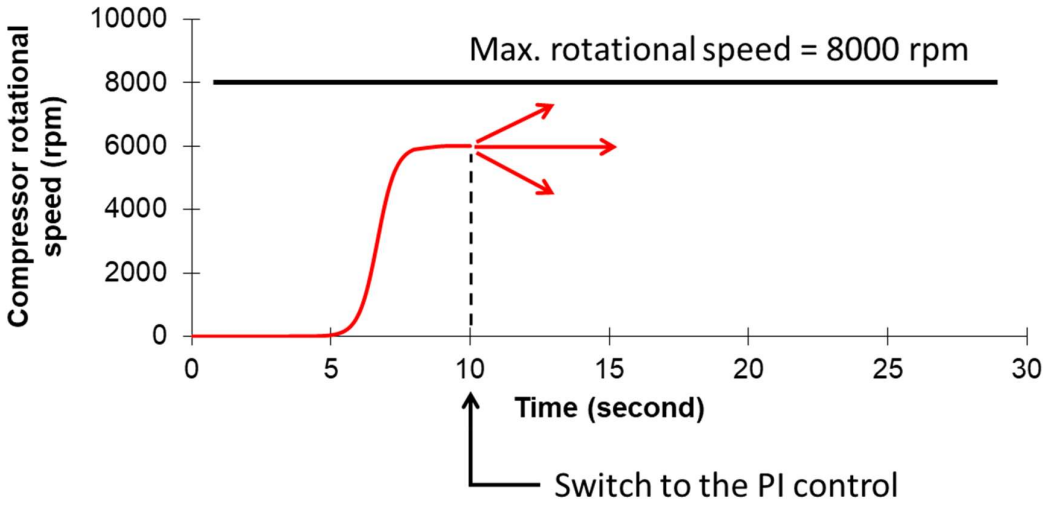

Table 2.8 shows the system operating conditions. The cabin structures provided in Marcos et al. (2014) were adopted in this investigation. It was assumed that the same intensity of global horizontal irradiance applies to all exterior structures of the car regardless of the car location and the direction of the sun. In the present model, the outdoor environment was treated as a thermal reservoir, so it was also assumed that the refrigerant temperature at the OHX outlet approaches the outdoor air temperature. The first damper was positioned to close the fresh air passage, and the vent was kept closed, so the indoor air recirculated during the simulations. The second damper is positioned to close the air passage flowing into the IHX, so all the cooled air bypasses the IHX supplied directly into the cabin during the simulations.

Table 2.8. Simulation condition (Ko et al., 2021b).

Condition	Value
Outdoor air temperature, ^{o}C	35 [a]
Outdoor air RH, %	70 [b]
OHX frontal mean air velocity, km h^{-1}	60
Solar irradiance, W m^{-2}	150
Cabin volume, m^3	3.2 [c]
Initial cabin temperature, ^{o}C	35
Initial cabin RH, %	16.44
Number of occupants	1
Evaporator temperature, ^{o}C	1
Suction superheating, ^{o}C	12
The initial pressure of the refrigerant, MPa	6
The initial temperature of the refrigerant, ^{o}C	35

[a] The average value of the highest temperature of Fukuoka except for rainy days, Aug. 2020 (Japan Meteorological Agency, accessed Jan. 23rd, 2021).

[b] The average value of RH of Fukuoka except for rainy days, Aug. 2020 (Japan Meteorological Agency, accessed Jan. 23rd, 2021).

[c] The value was estimated based on Marcos et al. (2014).

Chapter 3 Results and Discussion

3.1 Effect of the Cabin Set Temperature

A set of simulations was conducted in various cabin target temperatures (T_{cabin}). Figure 3.1a shows the cabin temperature and the supply air temperature (i.e., the evaporator exit). Figure 3.1b and c show the cabin pull-down time ($t_{pull-down}$) and the RH of the cabin air. The air temperature of the cabin decreases from 35 ºC to each setpoint value with the system operation.

Figure 3.1. Effect of the cabin set temperature; (a) temperature of the cabin air and supply air, (b) pull-down time, and (c) RH of the cabin air (Ko et al., 2021b).

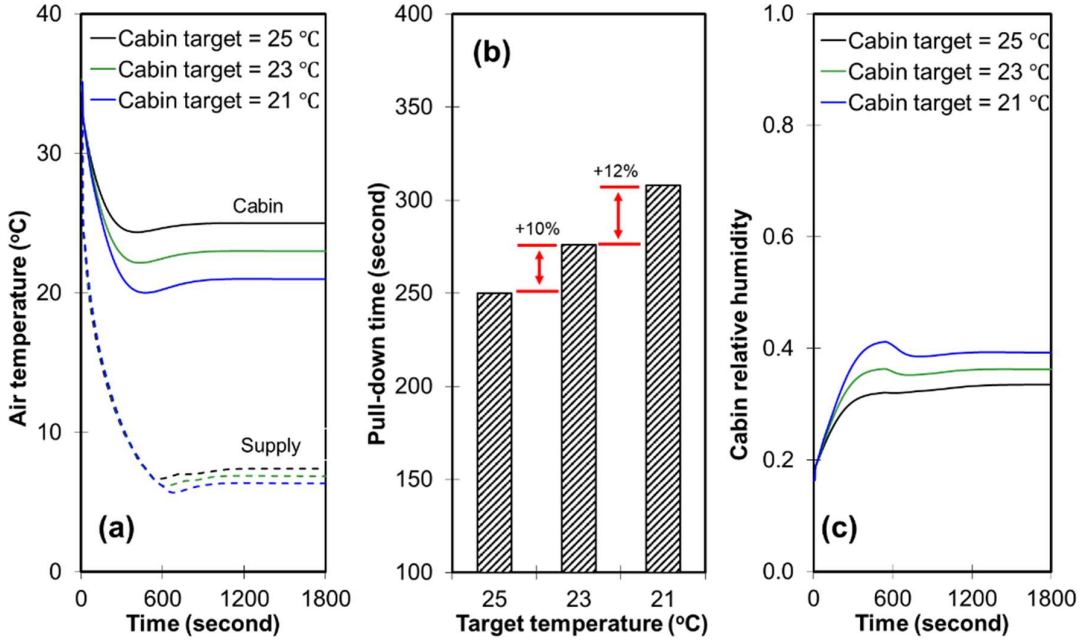

Figure 3.2a shows the moisture condensation rate with time. When the cabin target temperature is set to be a lower value, a large amount of moisture condensation occurs; this is because the system raises the air circulation rate (Figure 3.2b) to decrease the cabin temperature to the setpoint rapidly, so the amount of moisture flowing into the evaporator volume increases. The condensation rate in each case converges the same value after 1400 seconds regardless of the cabin set temperatures since the evaporator operating temperature was set to be the fixed value, 1 ºC, in all cases. However, Figure 3.2b indicates that the cabin RH at 1800 seconds has a larger value when the set temperature is lower; this is because the moist-air with a lower dry-bulb temperature has a higher RH value under the same humidity ratio. Figure 3.2b shows the evaporator air flow rate for 1800 seconds. The air flow rate temporarily increases with the start of the system operation to remove thermal energy from the cabin air. The cabin temperature approaches the setpoint closely; the system gradually decreases the evaporator airflow rate and finds a quasi-steady-state operating condition. After that, the system reaches the steady-state and is stabilized, the flow rate converges to a constant value and keeps it. Also, it is observed that the airflow rate keeps a higher value when the target temperature is set to be a lower value.

Figure 3.2. Effect of the cabin set temperature; moisture condensation rate at the evaporator (Ko et al., 2021b).

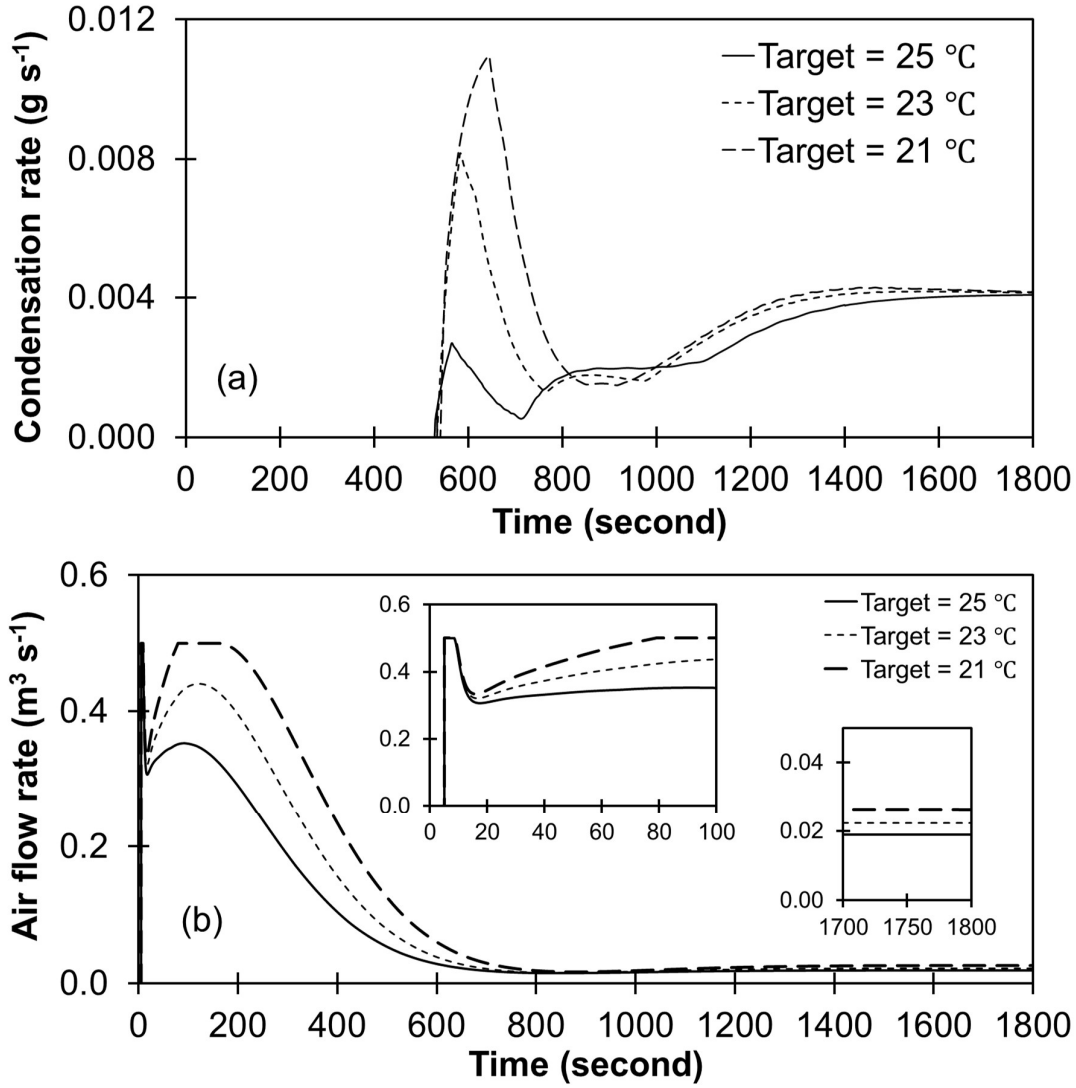

Figure 3.3a and b show the transient responses of the compressor rotational speed and the orifice cross-sectional area of the expansion valve with time, respectively. Figure 3.3c presents the refrigerant mass flow rate at the expansion valve outlet, resulting from the compressor and expansion valve responses. From Figure 3.3a and b, when the cabin temperature is set to be lower value, the rotational speed and the opening degree of the expansion valve increase and keep a higher value; this tendency is observed in the start-up period as well as in the steady-state operation. This can be explained as follows. The evaporator should absorb more heat from the cabin return air to pull the cabin temperature down to a lower temperature and keep it. In the meantime, if more heat transfers from the air to the refrigerant in the evaporator, the suction superheating will be departed from the set value (ΔT_{sup}, 12 °C). To maintain the superheating to the setpoint, more refrigerant needs to be supplied into the evaporator, as shown in Figure 3.3c. For that, the expansion valve increases its opening degree, as shown in Figure 3.3b. Whiles, when the valve opening degree increases, the refrigerant pressure at the high-pressure side decreases, and the refrigerant pressure at the low-pressure side increases; in so doing, the evaporator operating temperature increases and becomes out of the set value ($T_{evap.ref}$, 1 °C). To meet the set evaporator temperature, the compressor speed increases as shown in Figure 3.3a. Meanwhile, from Figure 3.3b and c, it can be confirmed that the transient behavior of the refrigerant mass at the expansion valve outlet highly depends on the response of the expansion valve opening degrees. The temporal variation of the mass flow rate at the expansion valve outlet indicates a very similar trend with the orifice cross-section area change. The literature (Kim et al., 2007b) reported the start-up operation of an R-744 heat pump for a fuel cell vehicle in the cabin heat-up condition, and the refrigerant mass flow rate was measured at the expansion valve inlet. The transient characteristic of the calculated mass flow rate at the expansion valve outlet in the present simulation shows a similar tendency with that of Kim et al. (2007b). The study (Pfafferoott & Schmitz, 2004) developed a transient model of an R-744 refrigeration system and compared the calculated mass flow rate with the measured mass flow rate obtained from their experimental refrigeration system. When comparing with the temporal trend of the calculated and measured data (Pfafferoott & Schmitz, 2004), the present model also shows a similar tendency of the refrigerant mass flow rate at the initial start-up operation.

Figure 3.3. Effect of the cabin set temperature; (a) compressor rotational speed, (b) orifice cross-sectional area of the expansion valve, and (c) refrigerant mass flow rate at the expansion valve outlet (Ko et al., 2021b).

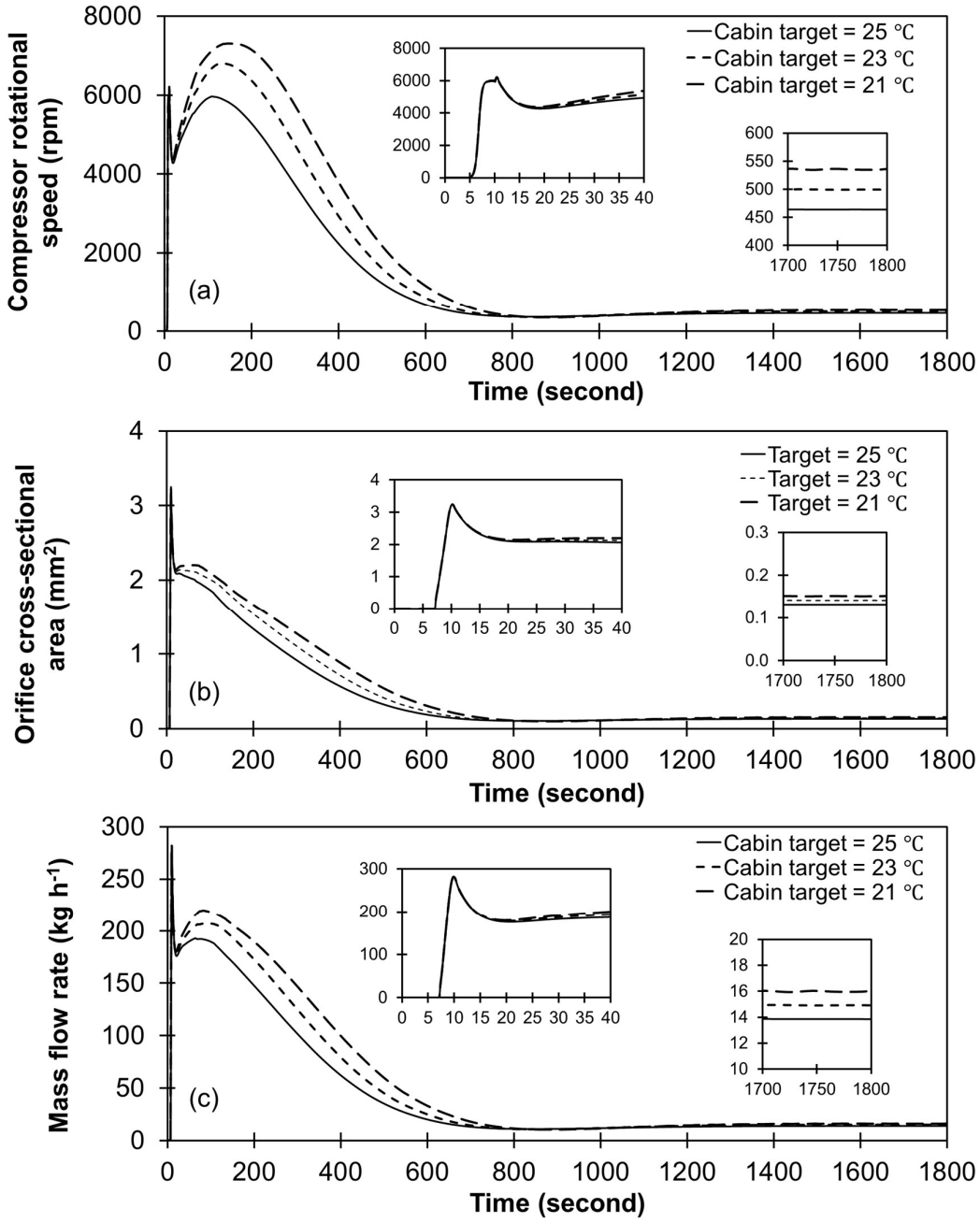

Figure 3.4 compares the refrigerant mass flow rate at the compressor outlet and the expansion valve outlet when the cabin target temperature is 25 ^{o}C. The transient characteristics of the mass flow rate at the discharge highly depend on the compressor response. In Figure 3.3a, the rotational speed rapidly increases at 5 seconds, and then it gradually converges to 6000 rev min^{-1} at 7 seconds; the mass flow rate at the discharge sharply increases with the compressor speed for 2 seconds (5 to 7 seconds). When the rotational speed becomes temporarily steady (Figure 3.3a), the mass flow rate decreases and recovers it for about 3 seconds (7 to 10 seconds). Unlike the transient behavior of the mass flow rate at the discharge port, the mass flow rate at the expansion valve outlet increases from 7 seconds. There is a temporary delay of 2 seconds after the compressor operation; this is because the expansion valve is kept closed for 7 seconds (0 to 7 seconds), it is opened at 7 seconds. Then next for 1.5 seconds, the mass flow rate at the discharge decreases but the mass flow rate at the expansion valve outlet increases. This fluctuation of the discharge flow rate and the time delay of the flow rate at the expansion valve outlet can be explained that the refrigerant migrates from the high-pressure side and the low-pressure side. This refrigerant migrated to the low-pressure side flows into the compressor suction again, the refrigerant mass flow rate at the discharge is recovered. After that, when the PI controller starts to control the compressor speed, the system finds a balance point for the mass flow rates in both the high-pressure and low-pressure sides. Except for the initial 15 seconds, both sides' mass flow rates indicated the same value for all other cases.

Figure 3.4. Comparison of refrigerant mass flow rate at the compressor outlet and the expansion valve outlet (Ko et al., 2021b).

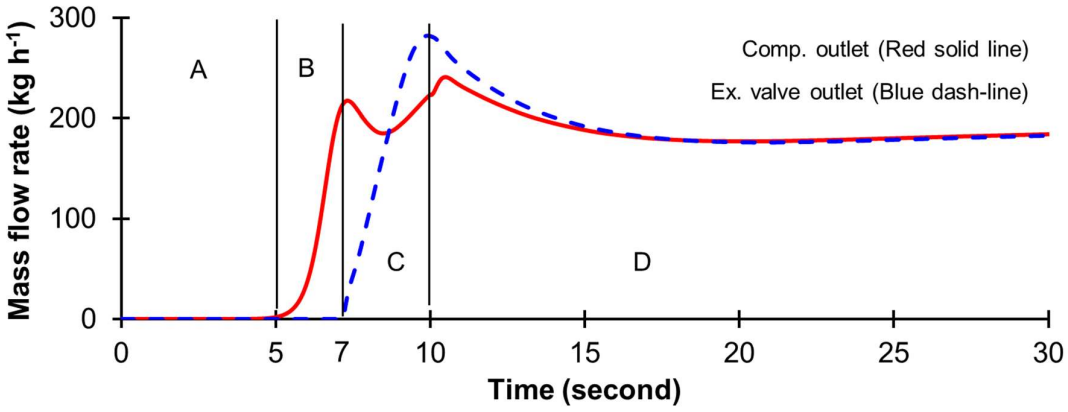

Regime	Compressor	Expansion valve
A	Off	Closed
at 5 seconds	On	Closed (*Start PI control*)
B	On (*Fig. 2.30*)	Closed (*Under PI control*)
at 7 seconds	On (*Fig. 2.30*)	Open (*Under PI control*)
C	On (*Fig. 2.30*)	Open (*Under PI control*)
at 10 seconds	On (*Start PI control*)	Open (*Under PI control*)
D	On (*Under PI control*)	Open (*Under PI control*)

Figure 3.5a and b depict the VCS pressure and temperature, respectively. The solid line and the dashed line represent the values at the discharge and the suction, respectively. Due to the responses of the compressor speed and the expansion valve opening degrees, the discharge pressure and temperature increase for the initial start-up stage, but after the system is stabilized, the discharge pressure and temperature converge to each proper operating condition, respectively. Besides, comparing with experimental results from Kim et al. (2007b), the present simulation results show similar transient behavior characteristics.

Figure 3.5. Effect of the cabin set temperature; (a) VCS pressure and (b) VCS temperature (Ko et al., 2021b).

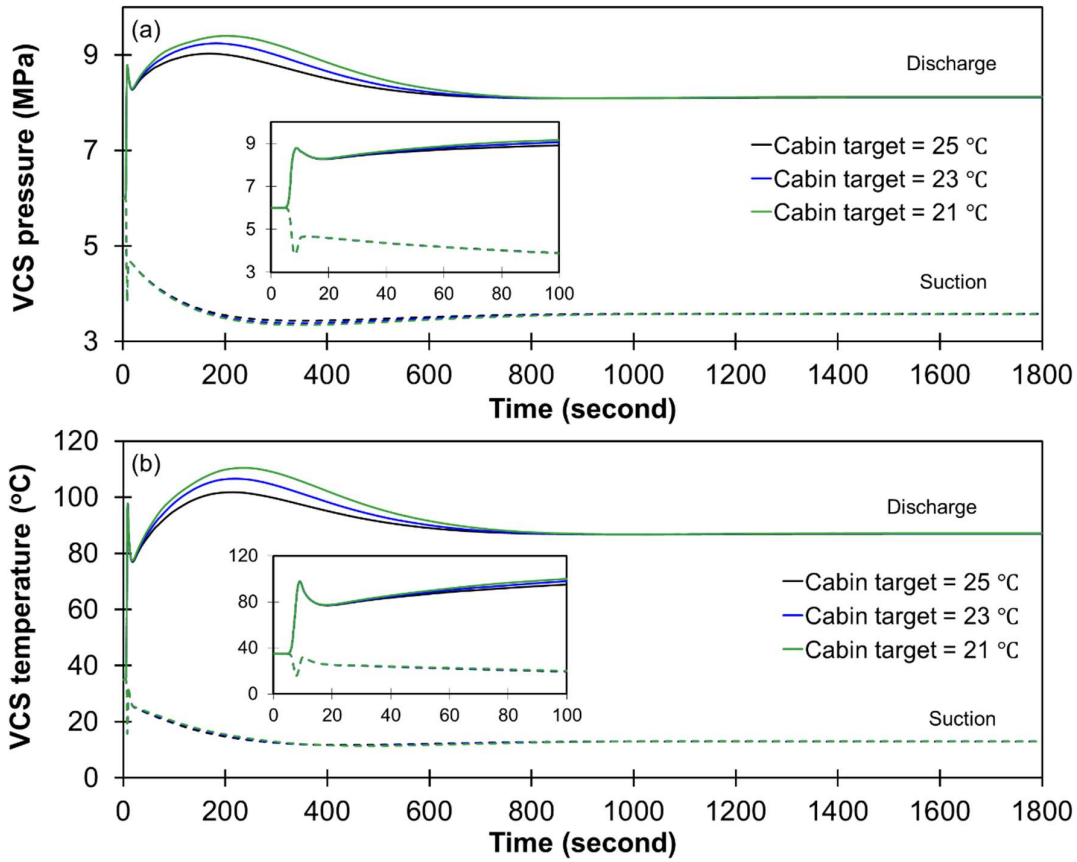

Figure 3.6a depicts system COP and compressor power consumption. The power consumption shows an increasing tendency when the target cabin temperature decreases. The system suffers additional loads during the pull-down operation period, the energy consumption increases during the early transient period and reaches a peak point then it gradually decreases. Thus, the system operates under the low COP condition in the start-up operation. Then the COP recovers gradually with time. This transient behavior of the system coincides with the behavioral characteristics mentioned in the previous study (Gado et al., 2008). Figure 3.6b presents normalized energy consumption ($\bar{W}$) and the normalized cabin pull-down time ($\bar{t}_{pull-down}$). $\bar{W}$ and $\bar{t}_{pull-down}$ were evaluated as follows:

$$\bar{W} = \frac{\left(\int_0^{t_{pull-down}} \dot{W}_{comp} dt\right)_{each\ case}}{\left(\int_0^{t_{pull-down}} \dot{W}_{comp} dt\right)_{Reference\ case}}, \tag{66}$$

$$\bar{t}_{pull-down} = \frac{(t_{pull-down})_{each\ case}}{(t_{pull-down})_{Reference\ case}}. \tag{67}$$

From the simulation results, when the cabin target temperature is set to be 23 ºC, it is observed that the compressor spends 29% more energy to achieve the setpoint than the case of 25 ºC (i.e., the reference case). Besides, when the target temperature decreases to be 21 ºC, the compressor energy consumption increases by about 22% than the case of the cabin target is set to be 23 ºC. On the other hand, when the cabin setpoint decrease in order of 23 ºC and 21 ºC, the cabin pull-down time increases 10% and 23%, respectively, against the case of 25 ºC.

Figure 3.6. Effect of the cabin set temperature; (a) compressor power and COP and (b) normalized energy consumption and normalized cabin pull-down time (Ko et al., 2021b).

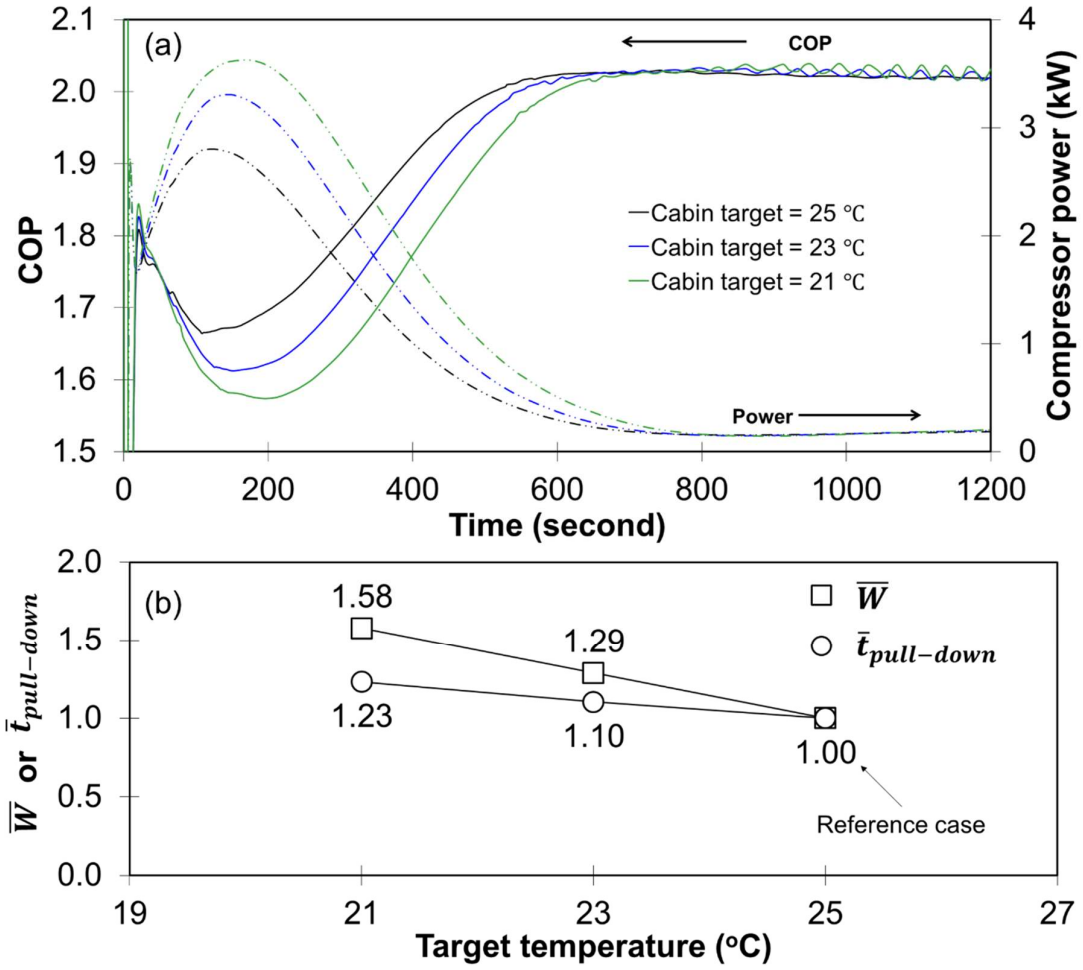

3.2 Effect of the Initial Temperature of the Cabin

Simulations were conducted by increasing the initial dry-bulb temperature from 35 ºC to 55 ºC. The cabin's initial RH was 16.4%, and the cabin set temperature was set to be 25 ºC.

In Figure 3.7, the results state that it takes more time to achieve the cabin's setpoint when the initial dry-bulb temperature is high because the larger amount of sensible heat should be removed during the initial start-up stage. From Figure 3.7b, when the initial temperature increases from 35 ºC to 45 ºC, the pull-down time increases by 62%. If the initial temperature increases by 10 ºC, again (from 45 ºC to 55 ºC), the pull-down time increases by 56%. This rising-rate of the pull-down time corresponds to 6% approximately for a 1 ºC increase. Meanwhile, after the system reaches a steady-state, the supply air temperatures and the RH converge to the same value, respectively, regardless of the initial temperature since the other operating conditions were fixed.

Figure 3.7. Effect of the initial temperature of the cabin; (a) Temperature of the cabin air and supply air, (b) pull-down time, and (c) RH of the cabin air (Ko et al., 2021b).

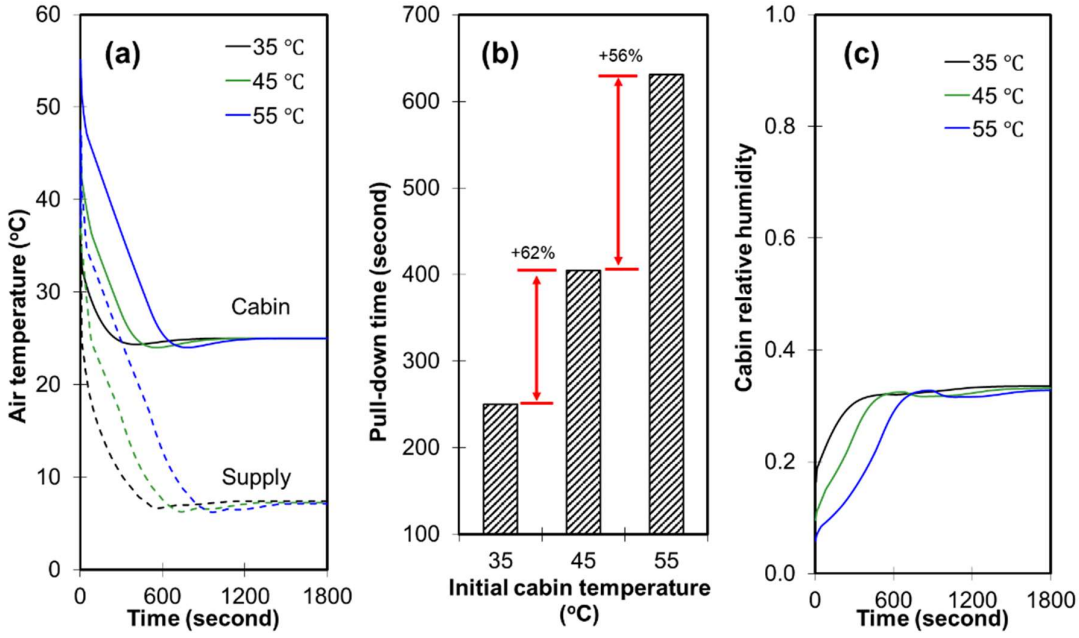

Figure 3.8a and b show the evaporator air flow rate and the moisture condensation rate at the evaporator. When the initial temperature is over 45 ºC, the system supplies air into the evaporator with a maximum flow rate of 0.5 m^3 s^{-1} during the pull-down operation period. After the system reaches a steady-state, the airflow rate in each case converges to the same value regardless of the initial cabin temperature. From Figure 3.8b, when the initial dry-bulb temperature is higher, the starting point of the moisture condensation is delayed; this is because the system should remove more sensible heat to reach the saturation state (RH of 100%) when the initial temperature is higher.

Figure 3.8. Effect of the initial temperature of the cabin; (a) evaporator airflow rate and (b) moisture condensation rate at the evaporator (Ko et al., 2021b).

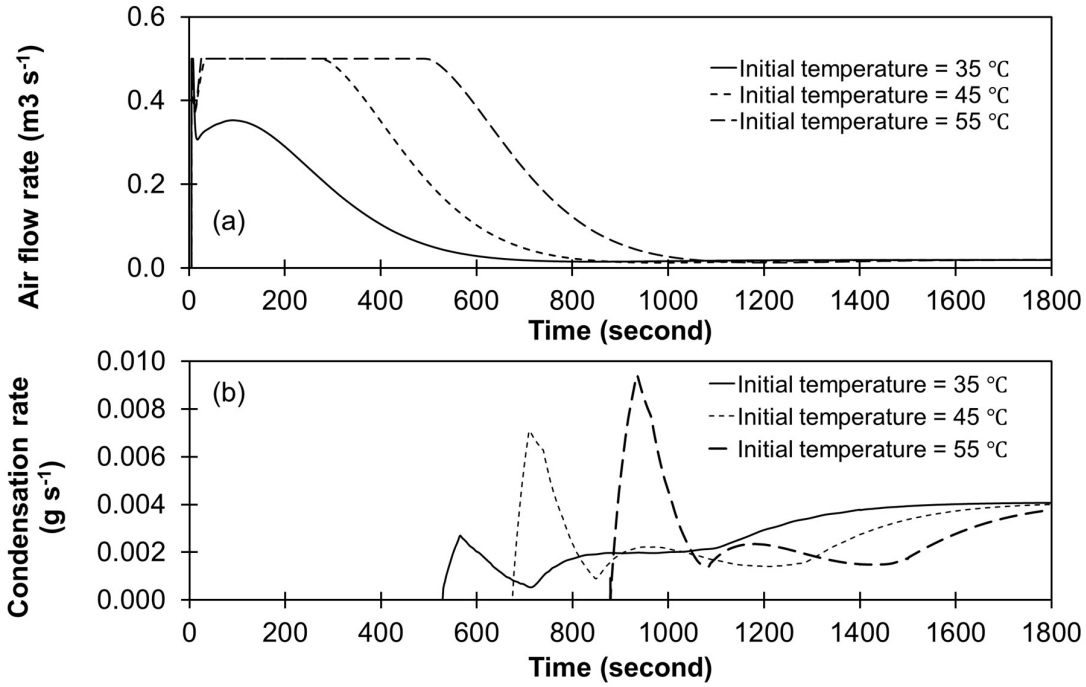

Figure 3.9a and b present the response of the compressor rotational speed and orifice cross-sectional area of the expansion valve with time, respectively. Figure 3.10c depicts the refrigerant mass flow rate at the expansion valve outlet. When the cabin's initial temperature is 45 ºC and 55 ºC, the compressor operates at the maximum speed during the start-up period. The compressor operates with the full speed for 500 seconds (40 to 540 seconds) in the 55 ºC initial temperature condition to decrease the evaporator temperature to the setpoint ($T_{evap.ref}$, 1 ºC). On the other hand, even the evaporator temperature does not reach the setpoint yet in this process, and the evaporator should remove the heat from the indoor recirculating airflow. Hence, the system increases the expansion valve opening degree. As shown in Figure 3.9b, when the initial temperature is 55 ºC, the expansion valve's cross-sectional area maintains a larger value than the 45 ºC initial temperature case. When comparing the case 45 ºC and 55 ºC, the compressor operates with the same maximum speed for the initial 280 seconds (80 to 310 seconds) in both cases (Figure 3.9a). In the case 55 ºC, however, the system keeps a larger expansion valve opening degree for that 280 seconds than that of the case 45 ºC (Figure 3.9b). This difference in the valve opening degree affects the refrigerant mass flow rate. When comparing the mass flow rate of the 45 ºC and the 55 ºC shown in Figure 3.9c, the larger refrigerant mass flow rate is observed for the case 55 ºC, despite both compressors operate with the maximum speed during the 280 seconds initial operation.

Figure 3.9. Effect of the initial temperature of the cabin; (a) compressor rotational speed, (b) orifice cross-sectional area of the expansion valve, and (c) refrigerant mass flow rate at the expansion valve outlet (Ko et al., 2021b).

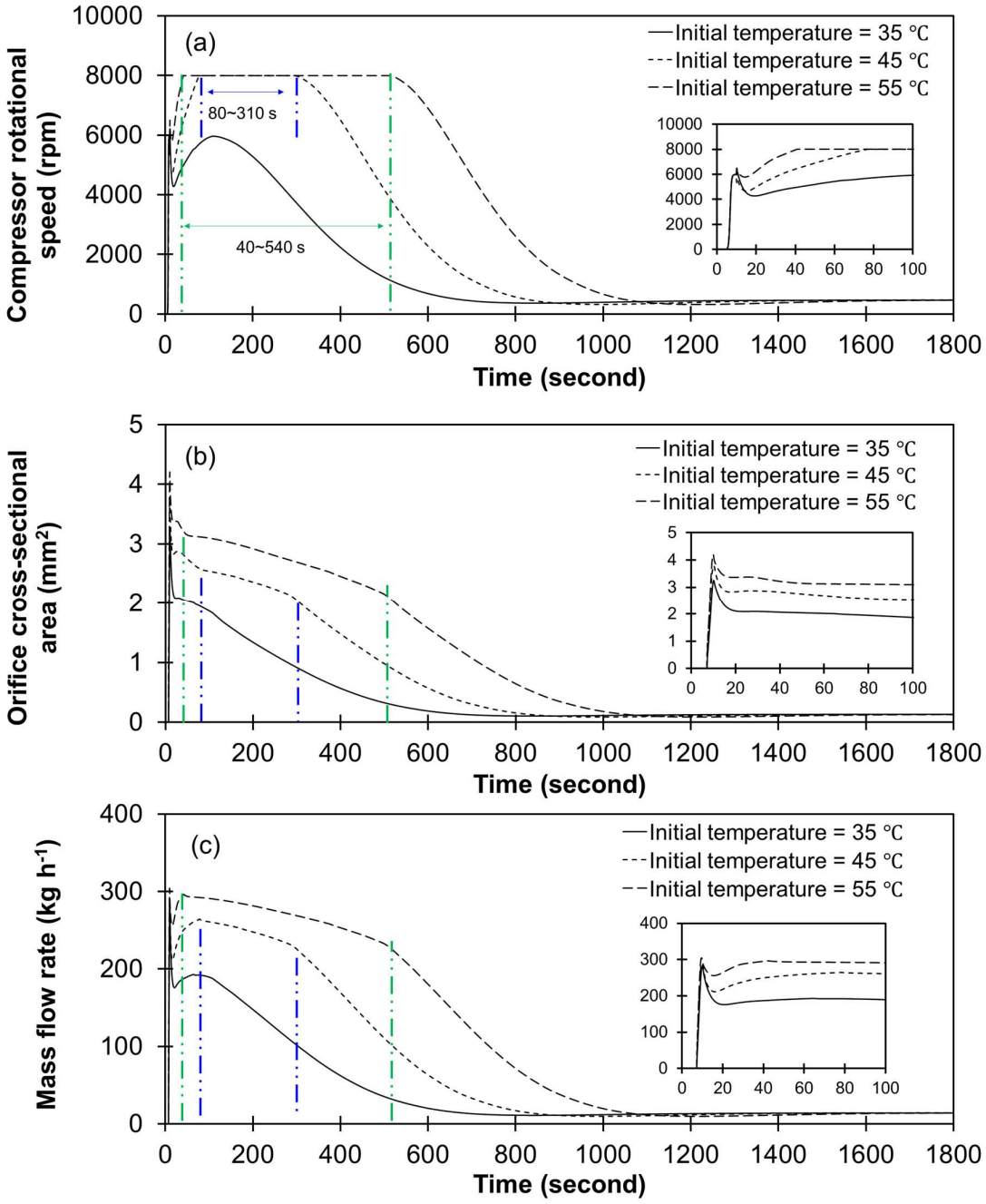

In the meantime, when the expansion valve opening degree becomes larger, the pressure and temperature at the high-pressure side of the system lower, but the pressure and temperature at the low-pressure side rise; this behavior is confirmed in Figure 3.10. It is observed that the discharge pressure and temperature of the case 55 ºC are lower than those of the case 45 ºC, for the 280 seconds. In the case of 55 ºC, however, the system pressure at the low-pressure side is higher than that of the case of 45 ºC during that period. Thus, the compressor operates a lower compression ratio in the case of 55 ºC than that of the 45 ºC for that 320 seconds; therefore, the compressor power consumption of the case 55 ºC is lower than that of the value for the case 45 ºC, during that operation period and this is confirmed in Figure 3.11.

Figure 3.10. Effect of the initial temperature of the cabin; (a) VCS pressure and (b) VCS temperature. (Ko et al., 2021b).

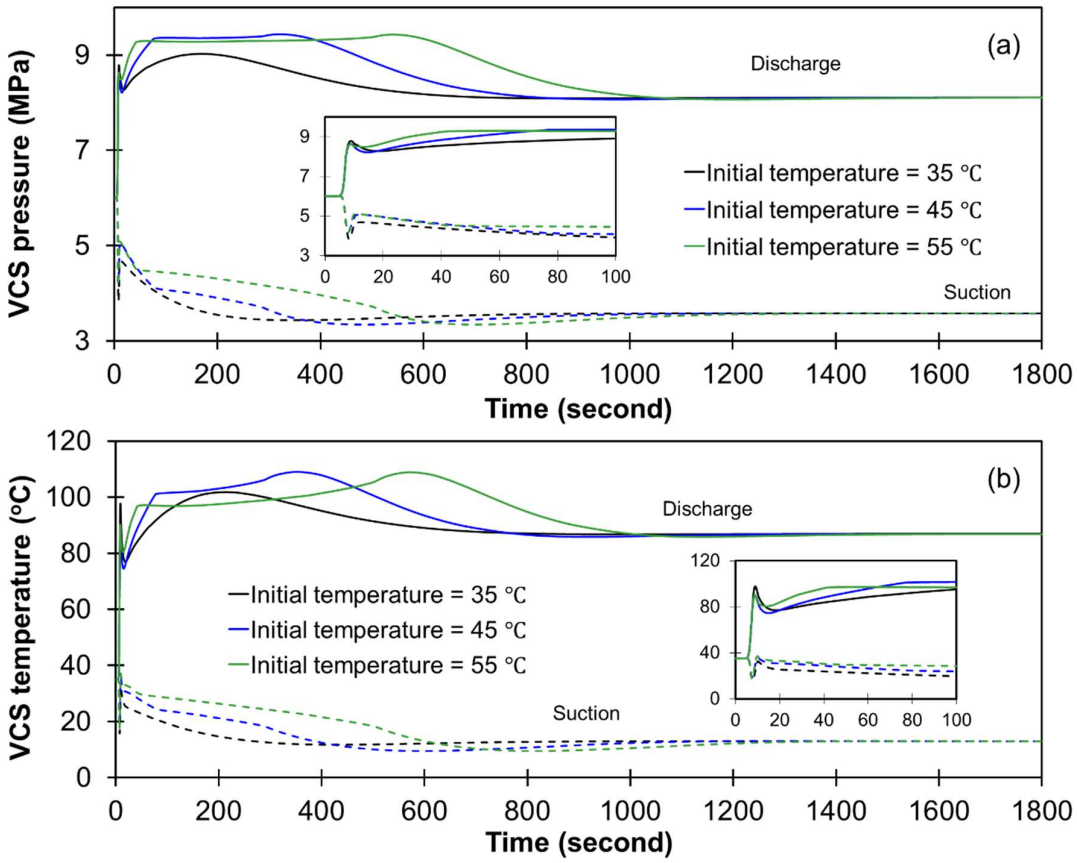

In Figure 3.11a, the compressor power for the 55 ºC maintains a lower value of 0.1 kW during the initial 280 seconds than that of the case 45 ºC. Thus, the system operates higher COP in the case of 55 ºC than that of the case 45 ºC. In the case of 55 ºC, however, the full-load operation period is longer than that of the case 45 ºC. Hence, the total energy consumption of the case 55 ºC is larger than that of the case 45 ºC. In Figure 3.11b, it is observed that the effect of the initial dry-bulb temperature of the cabin air on the energy consumption and cabin pull-down performance is considerable. When the initial temperature increase from 35 ºC (reference) to 45 ºC, it spends 60% longer time than the reference case to pull the cabin temperature down to the setpoint level; in this process, the compressor consumes 144% more energy. Furthermore, if the initial temperature increase from 45 ºC to 55 ºC, the system requires more energy input, about 289%, against the reference case; the pull-down time increases about 150%.

Figure 3.11. Effect of the initial temperature of the cabin; (a) compressor power and COP and (b) normalized energy consumption and normalized cabin pull-down time (Ko et al., 2021b).

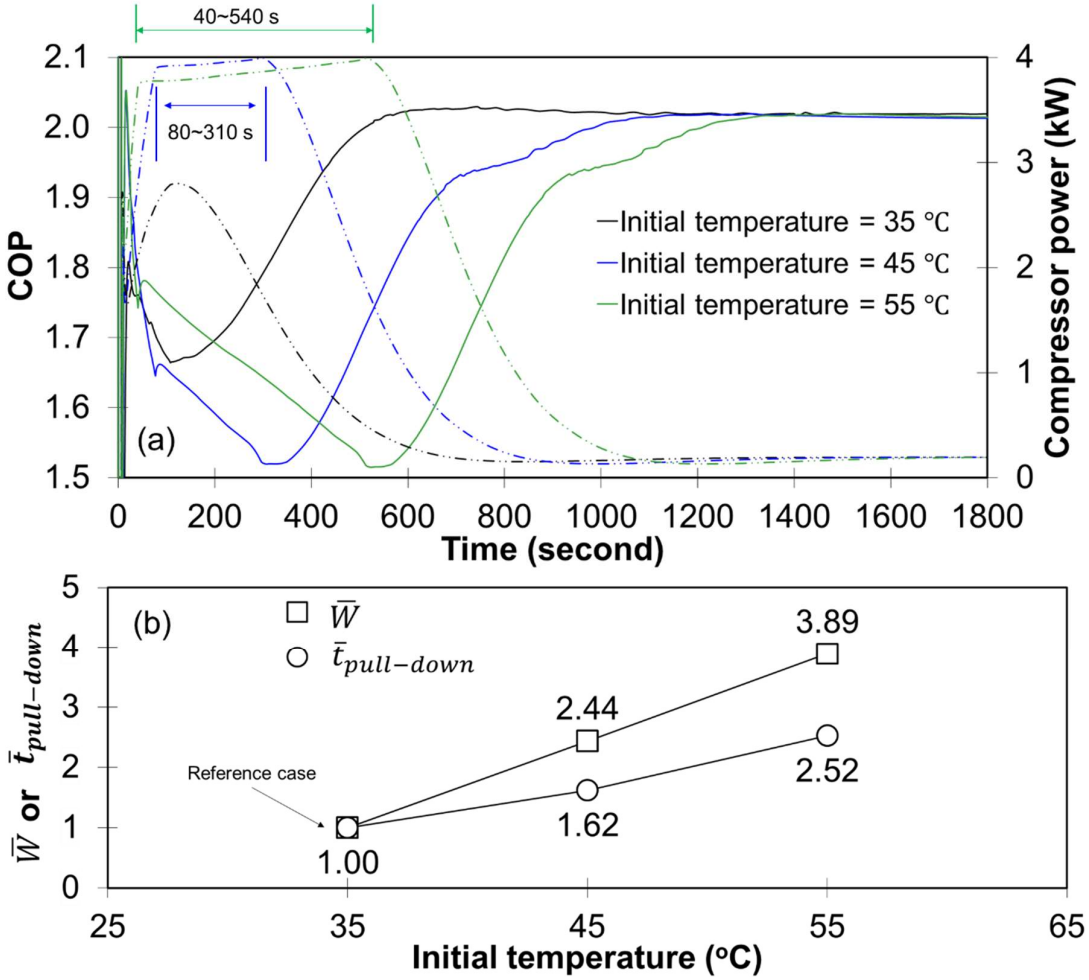

3.3 Effect of the Initial Relative Humidity of the Cabin

Simulations were conducted with increasing the initial RH of 33% (11.61 g kg^{-1}), 50% (17.77 g kg^{-1}), and 66% (23.67 g kg^{-1}) at the fixed initial dry-bulb temperature, 35 °C. The cabin pull-down setpoint was set to be 25 °C.

Figure 3.12a shows the temperatures of the cabin air and the supply air. Figure 3.12b and c depict the cabin pull-down time and the RH of the cabin air. From Figure 3.12a and b, a meaningful difference in the pull-down time against the initial RH is not observed. After the system reaches a steady-state, the cabin RH in each case converges to 33.5% regardless of the initial RH since the given evaporator operating temperature and the cabin's target temperature are fixed. Figure 3.12c and shows that the RH increases temporarily because the cabin dry-bulb temperature decreases in the early initial stage, but the moisture condensation does not start yet at the evaporator.

Figure 3.12. Effect of the initial RH of the cabin; (a) temperature of the cabin air and supply air, (b) pull-down time, and (c) RH of the cabin air (Ko et al., 2021b).

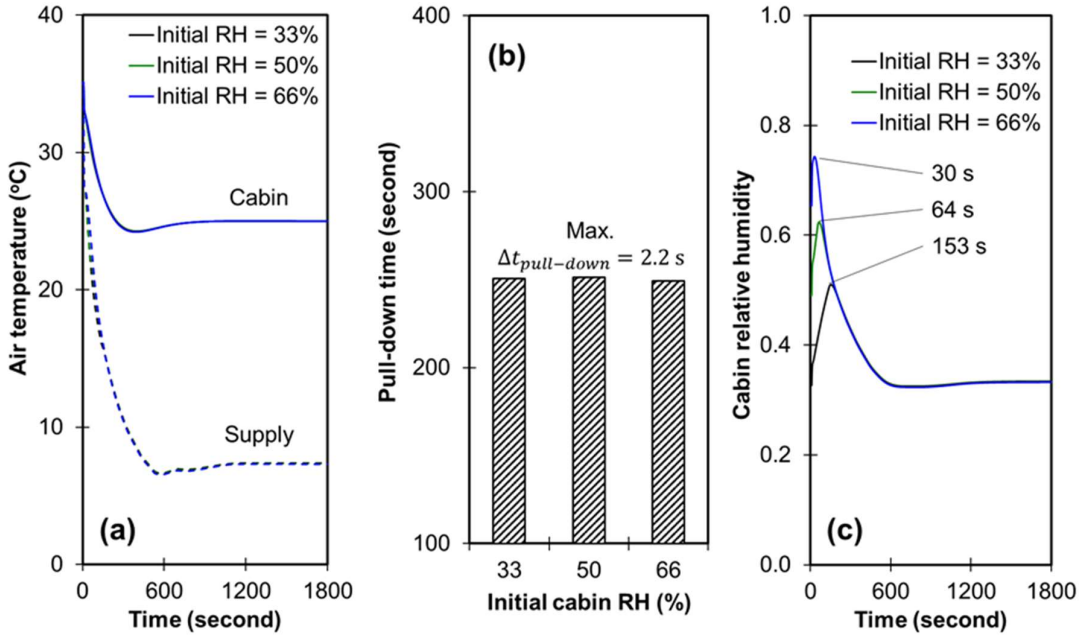

Figure 3.13a and b show the airflow rate and the moisture condensation rate at the evaporator, respectively. From Figure 3.13a, the higher initial RH means that more latent heat load imposes on the system at the start-up and pull-down operation period. So, the system increases the airflow rate in the AHU when the initial RH is high. In Figure 3.13b, the higher initial cabin RH starts condensation faster, also the total amount of condensed moisture increases.

Figure 3.13. Effect of the initial RH of the cabin; (a) evaporator airflow rate and (b) moisture condensation rate at the evaporator (Ko et al., 2021b).

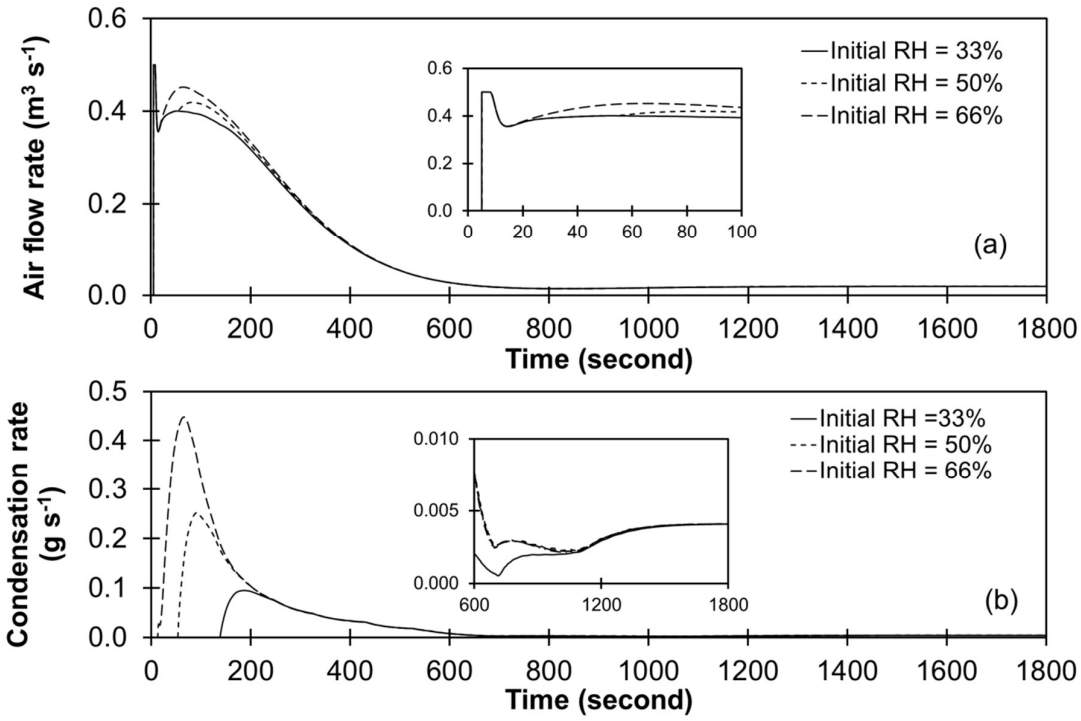

Figure 3.14 shows the transient behavior of the system, resulting from the compressor and expansion valve response. The higher initial RH of the cabin air means the increase of the cooling load, so the response characteristics of the compressor and valve are similar to the above two cases that the sensible heat load increases. Also, it is observed that the effect of the latent heat load on the transient behavior of the system is relatively smaller than that of the sensible heat load. Figure 3.14a presents the refrigerant mass flow rate at the expansion valve outlet. Figure 3.14b and c depict the operating pressure and temperature of the VCS. With the rise of the cabin initial RH, a slight increase in the refrigerant mass flow rate, the discharge pressure, and the discharge temperature is observed during the start-up and pull-down operation period. Figure 3.14d shows the proportion of the sensible heat and latent heat on the evaporator's cooling load. It is observed that the effect of the latent heat load on the transient behavior and performance of the system is relatively smaller than that of the sensible heat load.

Figure 3.14. Effect of the initial RH of the cabin; (a) refrigerant mass flow rate at the expansion valve outlet, (b) VCS pressure, (c) VCS temperature, and (d) the rate of contribution for the cooling load (Ko et al., 2021b).

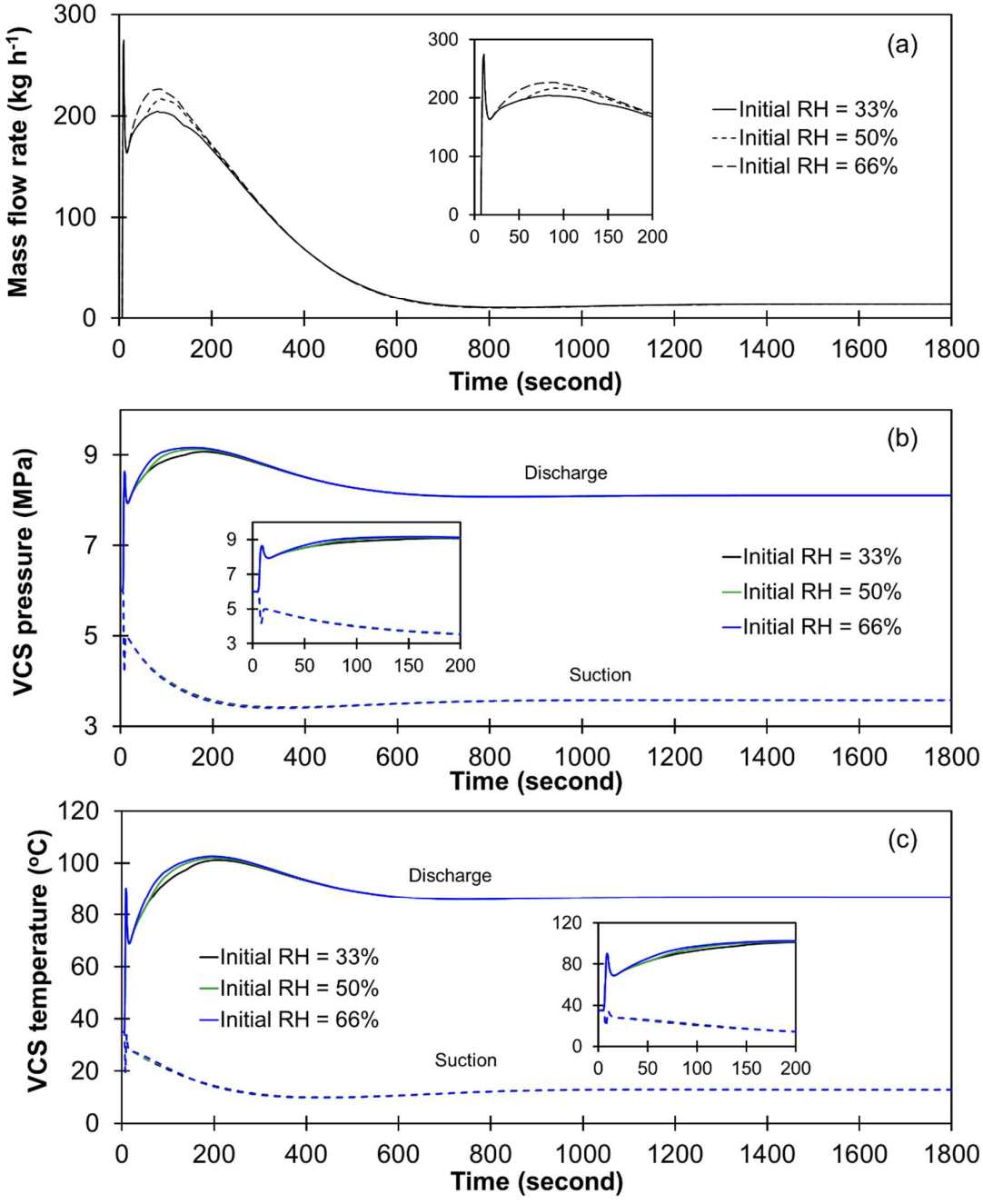

Figure 3.14. continued.

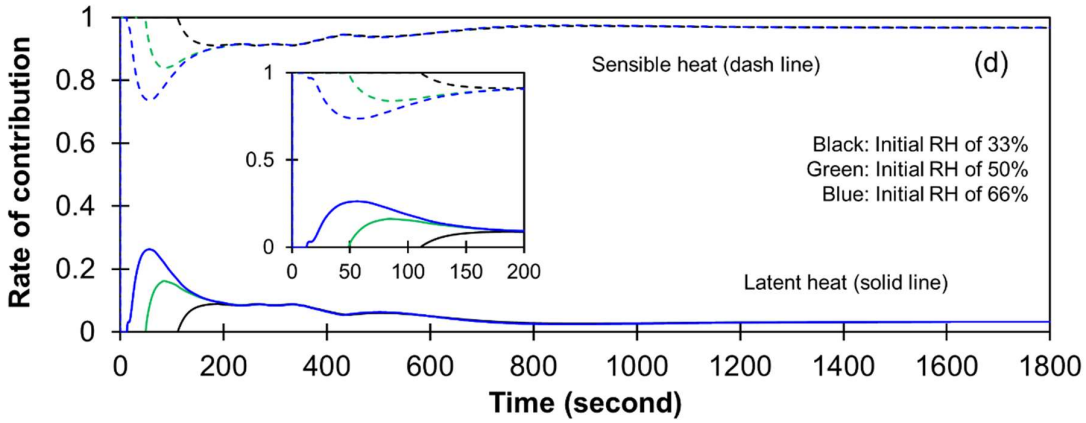

The cabin's initial RH has a relatively small impact on the system's transient performance compared with other parameters related to the sensible heat load. However, the negative effect of the initial RH of the cabin air on the system performance during the start-up and pull-down operation is observed in Figure 3.15a. When the initial RH increases, the compressor consumes more energy during that operation period. Thus, the system COP decreased in the period. Figure 3.15b depicts the normalized energy consumption accumulated for the pull-down operation period. When the initial RH is 50%, the system spends about more energy of 6% than the reference case (RH= 33%) to pull the cabin temperature down to the setpoint. The system requires more energy input of 9% than the reference case when the initial RH is 66% RH.

Figure 3.15. Effect of the initial RH of the cabin; (a) compressor power and COP and (b) normalized energy consumption and normalized cabin pull-down time (Ko et al., 2021b).

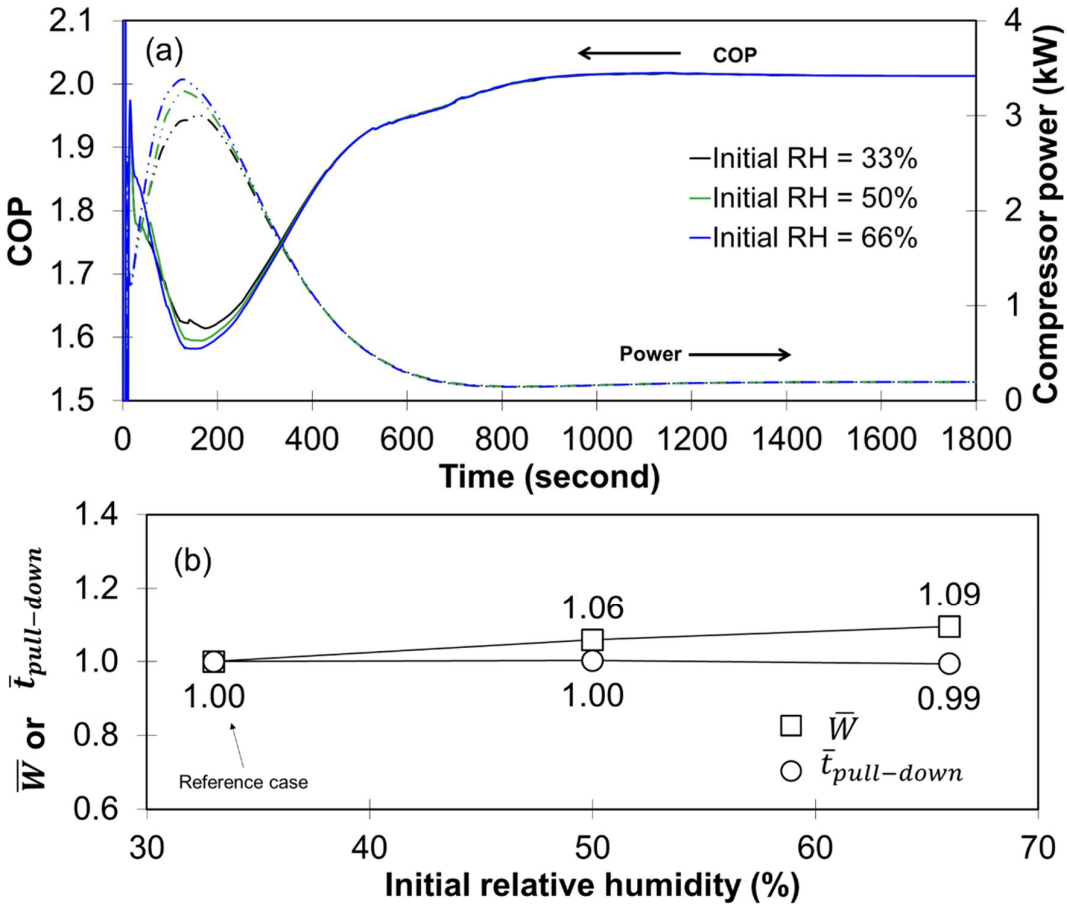

3.4 Effect of the Solar Irradiance

Simulations were conducted by increasing the solar irradiance intensity from 150 W m^{-2} to 350 W m^{-2}. The cabin pull-down setpoint was set to be 25 °C.

In Figure 3.16, considerable differences are not observed for the cabin cool-down time, supply air temperature, cabin temperature, and RH. Figure 3.17a and b show the airflow rate in the AHU and the moisture condensation rate, respectively. The results show that the air flow rate has almost the same tendency and values in all cases until the system reaches a steady-state. After the system is stabilized, the air flow rate increases under greater solar load conditions since the system should remove more heat from the cabin. Besides, when solar irradiance is higher, the starting point of moisture condensation is delayed; this can be explained as follows. The moist-air temperature should reach the dew point to start condensation. Under a more strong solar load condition, it takes more time that the system cools down the cabin's return air, and the condensation rate reaches a steady-state point fast; this is because the AC increases the air flow rate. After the system reaches a steady-state, the condensation rate converges to the same value regardless of the solar load. After simulations finished, the total amount of condensed water moisture indicated the same value.

Figure 3.16. Effect of the solar irradiance; (a) temperature of the cabin air and supply air, (b) pull-down time, and (c) RH of the cabin air.

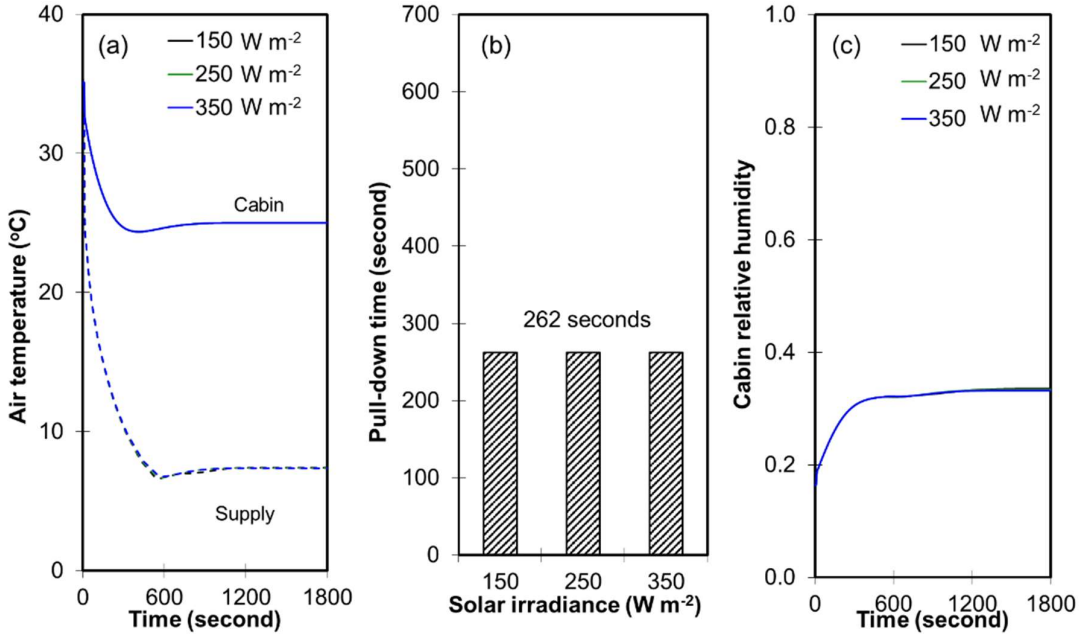

Figure 3.17. Effect of the solar irradiance; (a) evaporator airflow rate and (b) moisture condensation rate at the evaporator.

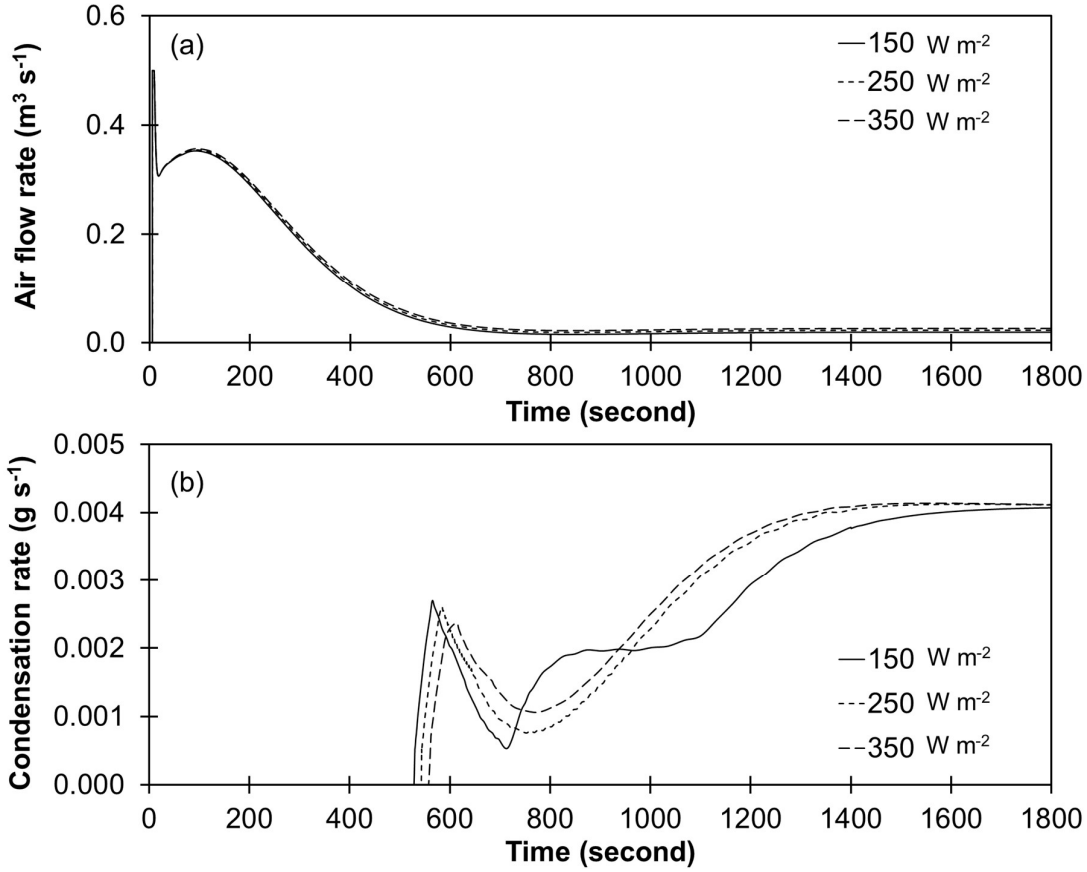

Figure 3.18 shows the responses of the compressor speed and orifice cross-sectional area of the expansion valve with time. The operation characteristics of the compressor speed and expansion valve opening degrees are not changed for the initial start-up stage against the variation of the solar load. However, after the system reaches the steady-state, the higher rotational speed and the large valve opening degree are observed in cases of larger solar loads. The system's response characteristic is similar when the cooling load increases; these are observed in Figure 3.18 and Figure 3.19.

Figure 3.18. Effect of the solar irradiance; (a) compressor rotational speed and (b) orifice cross-sectional area of the expansion valve.

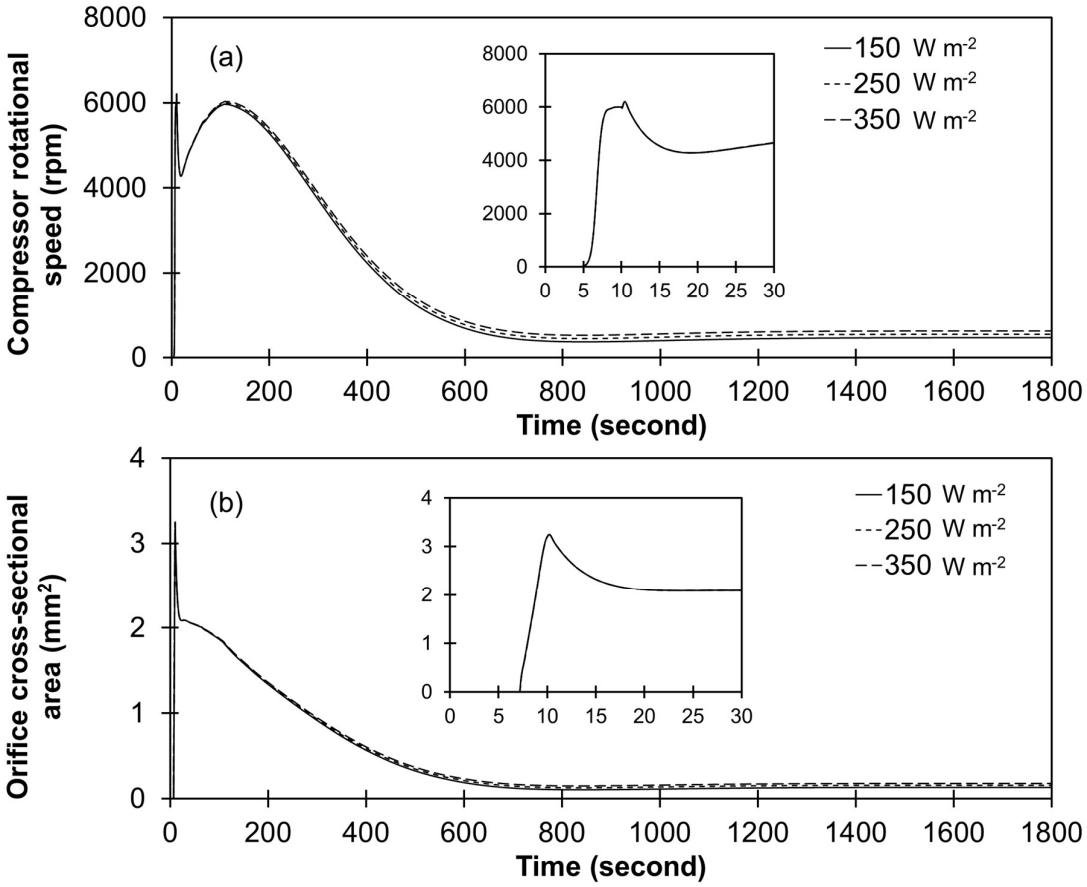

Figure 3.19. Effect of the solar irradiance; (a) refrigerant mass flow rate at the expansion valve outlet, (b) VCS pressure, and (c) VCS temperature.

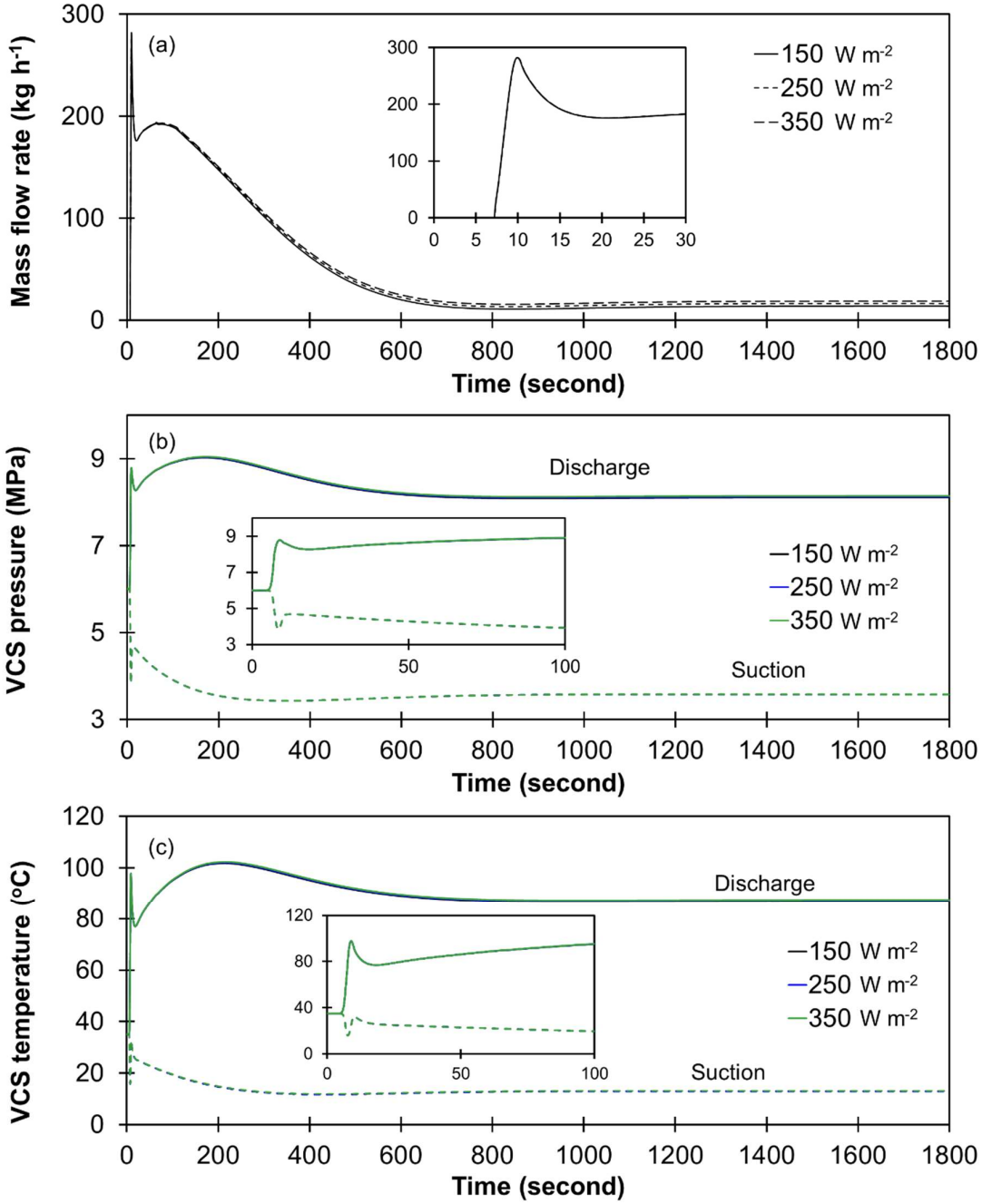

When the solar irradiance increases, the compressor consumes more energy during that operation period. Thus, the system COP is degraded in the period (Figure 3.20). However, solar irradiance has a relatively small impact on the system's transient characteristics than other parameters. Figure 3.20b presents the normalized energy consumption accumulated for the pull-down operation period. Solar irradiance does not significantly affect the pull-down time, but the energy consumption remarkably. From Figure 3.20b, when the solar irradiance increases from 150 W m^{-2} to 250 W m^{-2}, the system spends about 3% more energy to achieve the cabin setpoint than the reference case (150 W m^{-2}). If the solar irradiance increases to 350 W m^{-2}, the system requires more energy input of 4% than the reference case.

Figure 3.20. Effect of the solar irradiance; (a) compressor power and COP and (b) normalized energy consumption and normalized cabin pull-down time.

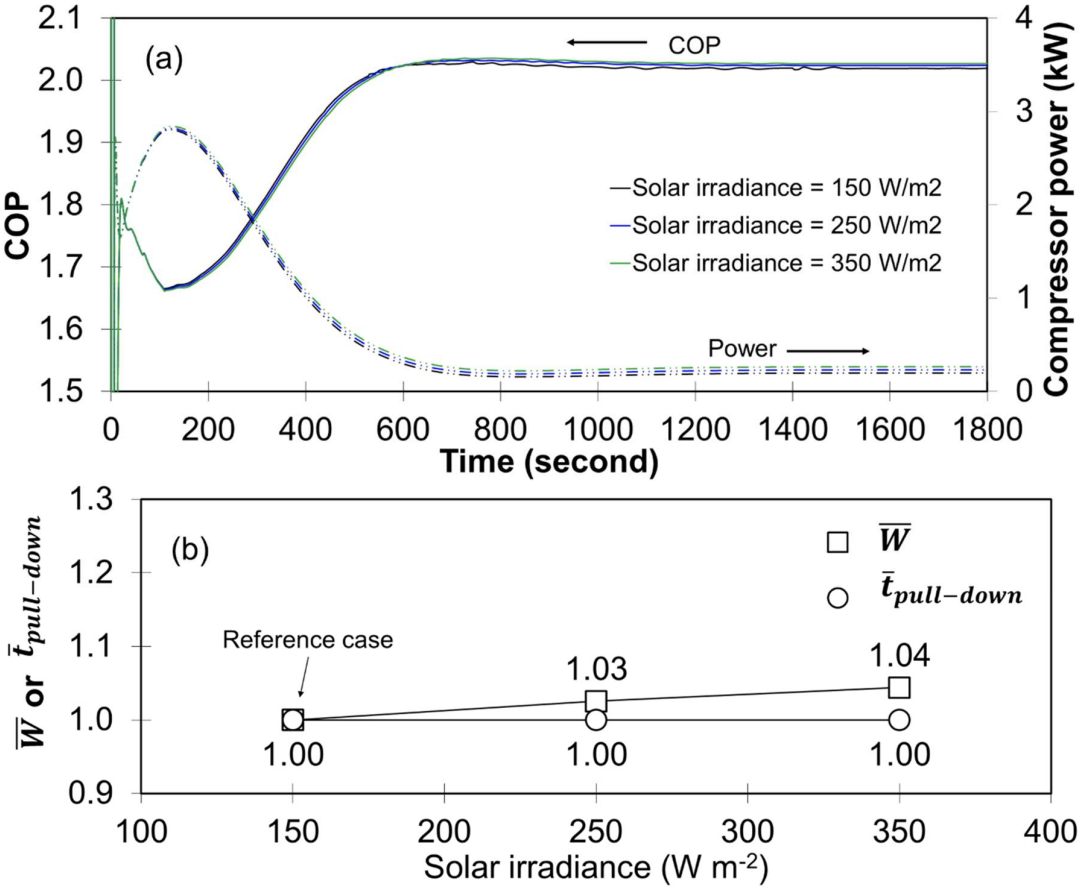

3.5 Effect of the Number of Occupants

A set of simulations was conducted with increasing the number of occupants under the initial RH of 16.4% at the fixed initial dry-bulb temperature, 35 °C. The cabin pull-down setpoint was set to be 25 °C.

Figure 3.21a shows the temperatures of the cabin air and the supply air. Figure 3.21b and c depict the cabin pull-down time and the RH of the cabin air. As shown in Figure 3.21, considerable differences are not observed for the cabin pull-down time, supply air temperature, cabin temperature, and RH.

Figure 3.21. Effect of the number of occupants; (a) temperature of the cabin air and supply air, (b) pull-down time, and (c) RH of the cabin air.

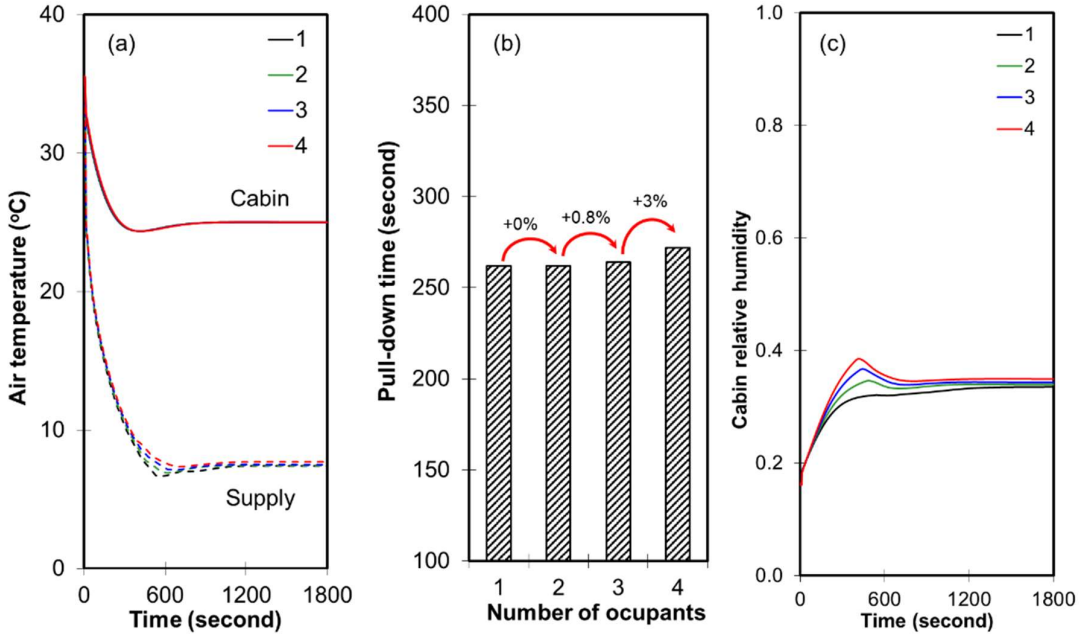

Figure 3.22a depicts the airflow rate in the AHU. Since the cabin's cooling load increases when the number of occupants increases, more thermal energy should be removed from the cabin, so the AC increases the airflow rate. Figure 3.22b shows the condensation rate of water moisture at the evaporator. As shown in Figure 3.22b and c, when the number of passengers increases, the moist-air reaches the dew point earlier so that the condensation starts earlier. Besides, it is observed that the condensation rate increases with the increment of the number of occupants.

Figure 3.22. Effect of the number of occupants; (a) evaporator airflow rate, (b) moisture condensation rate at the evaporator, and (c) psychrometric chart.

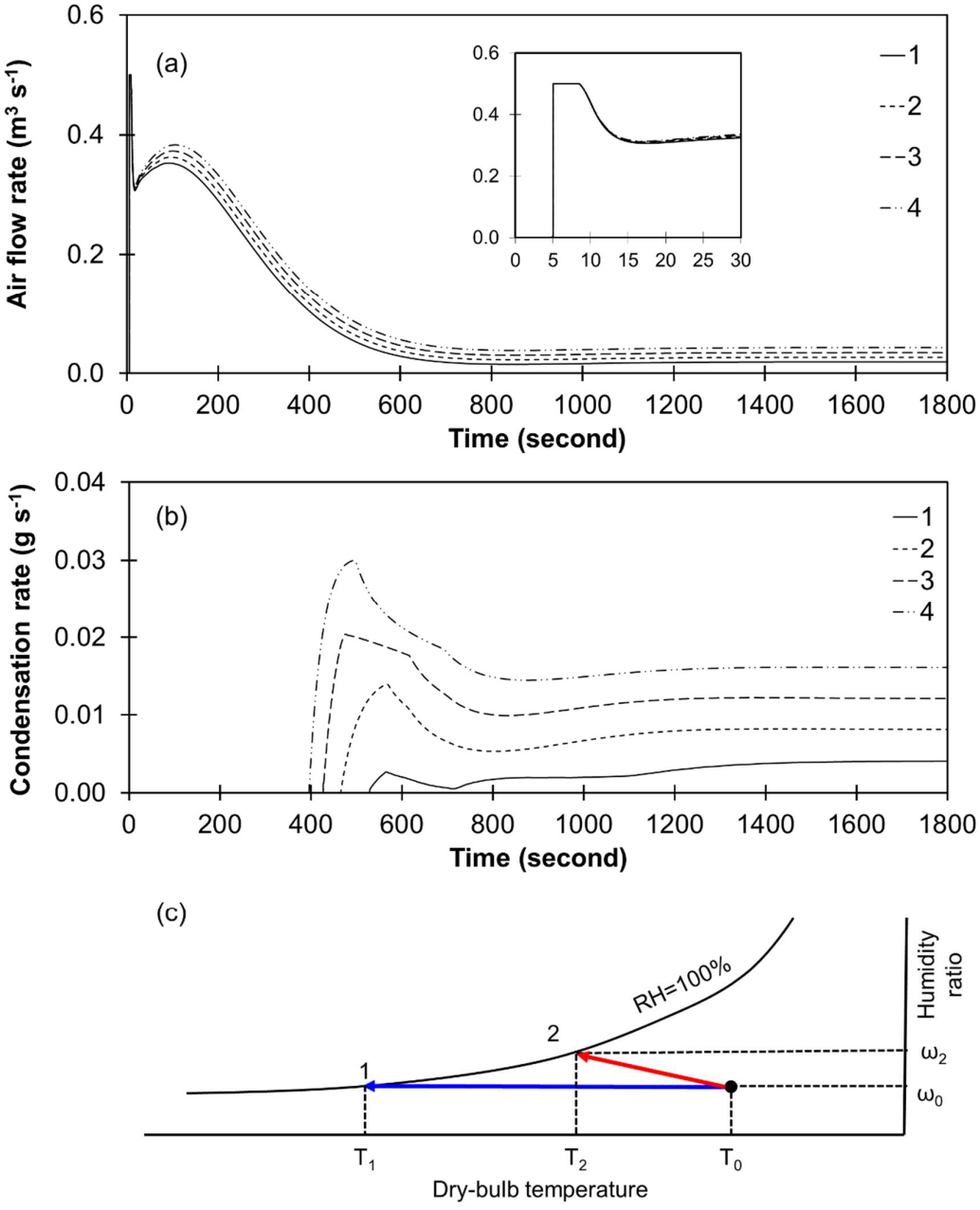

Figure 3.23 shows the compressor rotational speed and orifice cross-sectional area of the expansion valve with time. Due to an increase in the number of occupants, the more heat transfers from the air to the refrigerant in the evaporator so the evaporator cooling capacity increases. In this circumstance, if the refrigerant mass flow rate does not change, the suction superheating increases. The expansion valve's opening degree should increase to keep the set suction superheating degree and increase the refrigerant mass flow rate; this leads to the pressure of the high-pressure side going down and the pressure of the low-pressure side going up. Hence, the compressor speed rises to meet the set evaporator operating temperature.

Figure 3.23. Effect of the number of occupants; (a) compressor rotational speed and (b) orifice cross-sectional area of the expansion valve.

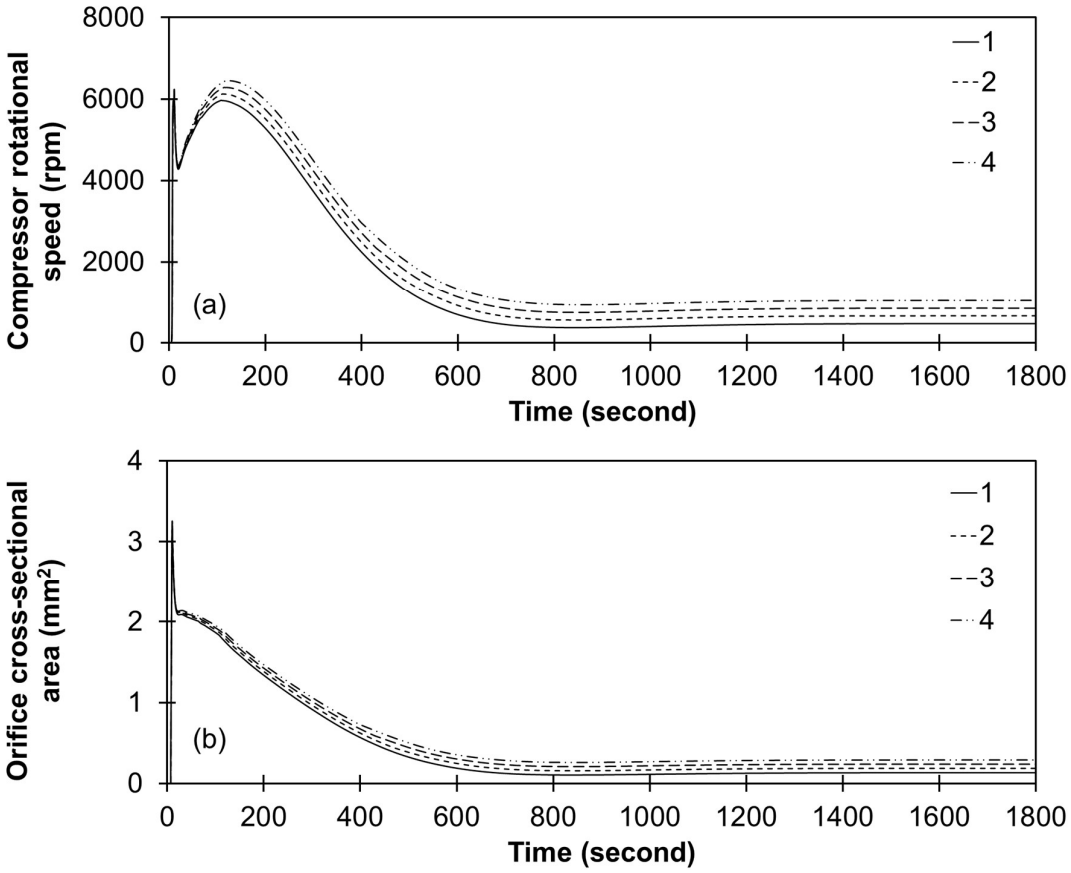

Figure 3.24a shows the refrigerant mass flow rate at the expansion valve outlet. Figure 3.24b and c present the pressure and temperature of the VCS with time, resulting from the compressor and expansion valve responses. The rise in the number of passengers also means that the system cooling capacity needs to be increased. The present simulation results indicate the same effect as the solar heat load increases. When comparing the response characteristics of air flow rate (Figure 3.22a), rotational speed (Figure 3.23a), and valve opening degree (Figure 3.23b) to those provided in the previous section (Figure 3.17a, Figure 3.18a, and b), the time-dependent tendencies are not so different with each other; however, the present results (Figure 3.22a, Figure 3.23a, and b) show notable change than the results in the previous section. It can be explained as follows: An increase in the number of occupants means that both sensible and latent heat load increase. Therefore, the rate of total cooling load increase is greater than when the solar load increase. A certain proportion of the solar irradiance imposes on the cooling load, but the other part is reflected into the outdoor; however, occupants' thermal load transits to the cooling load, 100%. Therefore, it is observed that the operating pressure and temperature at the high-pressure side of the VCS increases with the increment of the number of occupants in Figure 3.24; however, in Figure 3.19, any significant change in the high-pressure side does not appear, the effect is relatively minute.

Figure 3.24. Effect of the number of occupants; (a) refrigerant mass flow rate at the expansion valve outlet, (b) VCS pressure, and (c) VCS temperature.

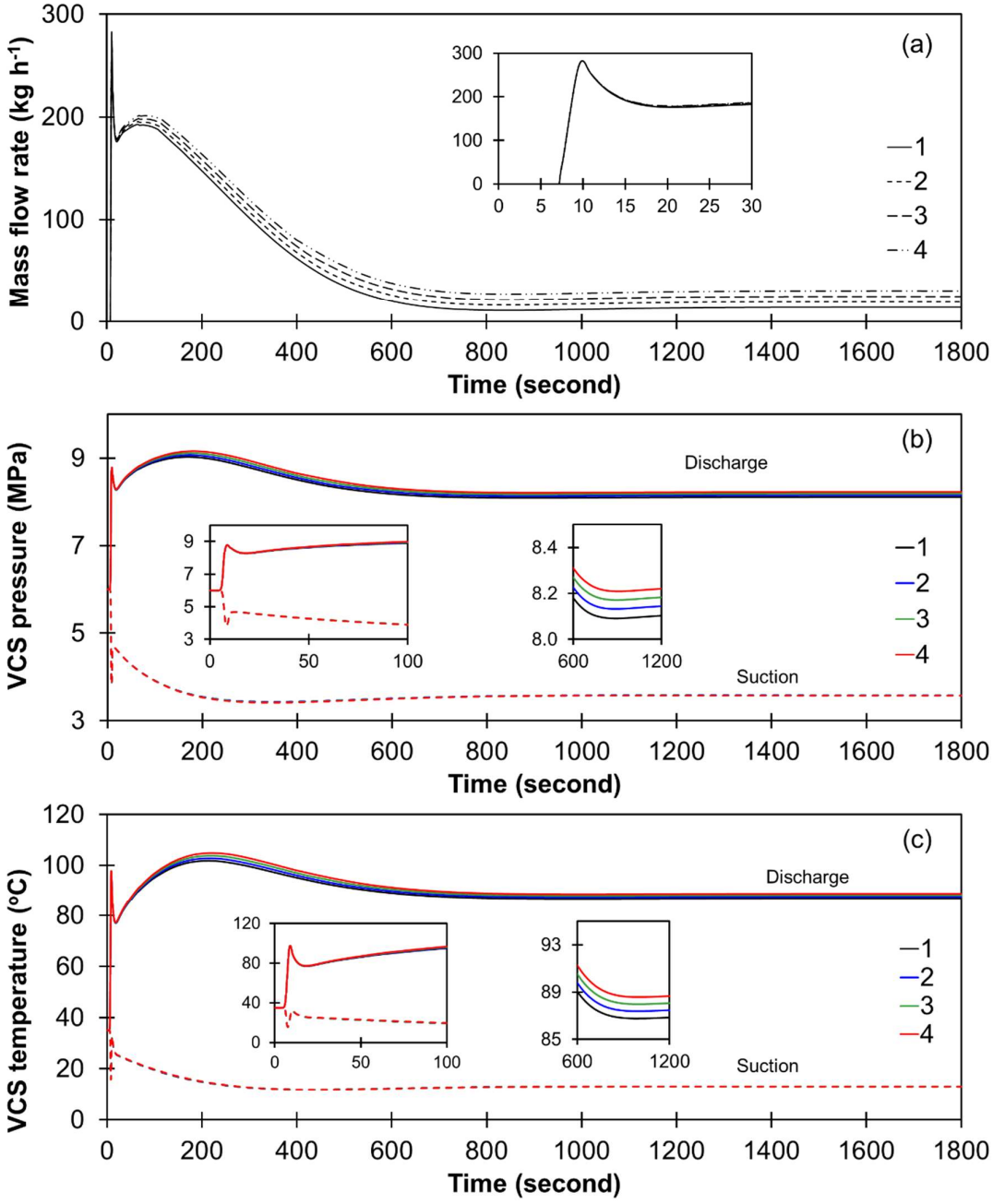

Figure 3.25a shows the COP and compressor power. The number of occupants has a relatively small impact on the system's transient performance compared with the influence of other parameters such as the initial temperature and target temperature. However, its effect is more significant than the initial RH and solar irradiance. When the number of occupants increases, the compressor consumes more energy during that operation period; thereby, the COP is degraded. Figure 3.25b depicts the normalized energy consumption accumulated for the pull-down operation period. The number of occupants does not significantly affect the pull-down time, but when it is over four, the pull-down time increases by 4% than the reference case. The effect of the number of occupants on the energy consumption for the start-up and pull-down operation is evident. When occupants number increases from 1 to 2, 3, and 4, the energy consumption increases by 3%, 9%, and 14% based on the reference case.

Figure 3.25. Effect of the number of occupants; (a) compressor power and COP and (b) normalized energy consumption and normalized cabin pull-down time.

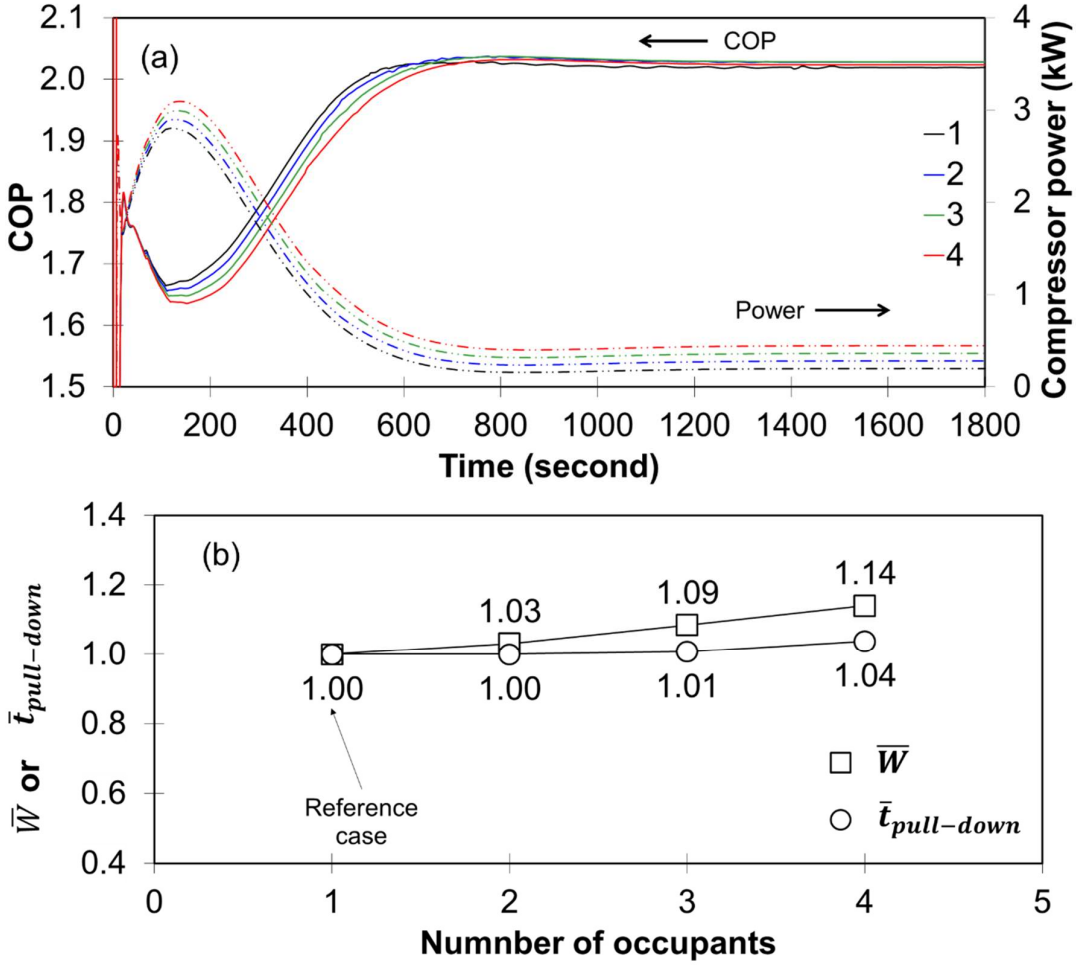

3.6 Ventilation

Occupants' respiration exhale carbon dioxide as a by-product and the carbon dioxide concentration in the cabin air increases with time. Thus, ventilation is necessary to keep a better indoor air quality (McQuiston et al., 2004).

Figure 3.26 shows the opening ratio of the first damper. For the early 2000 seconds, the system operates recirculation mode that the return air from the cabin flows into the evaporator then the cool air supplies into the cabin. At 2000 seconds, the system switches the operation mode to the ventilation mode. In this mode, the return air from the cabin is exhausted to the outdoor, the fresh air from the outdoor intakes and flows into the evaporator. The simulation was conducted under the condition provided in Table 2.8. The carbon dioxide concentration was set to be 500 ppm. The initial carbon dioxide concentration of the cabin was set to be the same value as that of the outdoor air.

Figure 3.26. First damper operation.

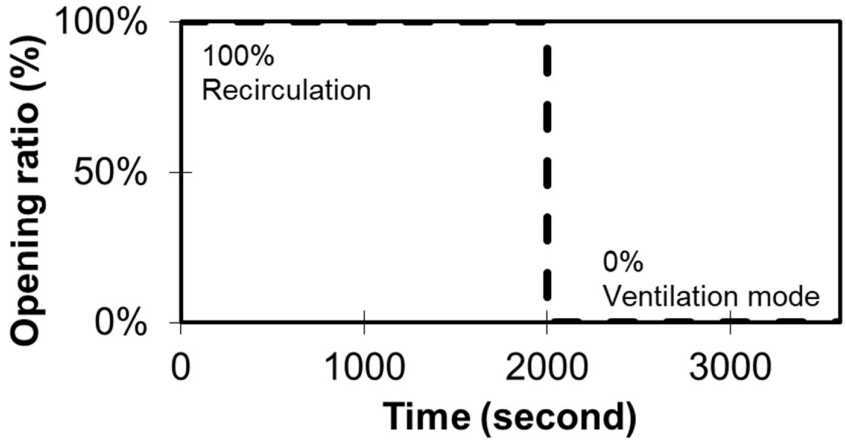

Figure 3.27a shows the air temperature of the cabin, supply, and at the evaporator. For 2000 seconds, the system operates recirculation mode, so the evaporator inlet air corresponds to the return air. The air temperature at the evaporator inlet is the same as that of the cabin. When the system switches ventilation mode, the fresh air of 35 ºC is cooled down to 14 ºC at the evaporator. This cool air supplies into the cabin. Figure 3.27b shows the cabin RH. During the recirculation mode, the cabin RH increases to 33.5%. However, when the ventilation mode is on, the cabin RH increases to 52%; this is because the humidity ratio of the supply air in the ventilation mode is higher than that of the recirculation mode. Figure 3.27c shows the carbon dioxide concentration of the cabin air. The concentration increases while the system is operated in recirculation mode. When the system switches to ventilation mode, the fresh (500 ppm) air intakes, and the carbon dioxide concentration decrease to 708 ppm.

Figure 3.27. Ventilation; (a) air temperature, (b) cabin RH, (c) carbon dioxide concentration in the cabin air.

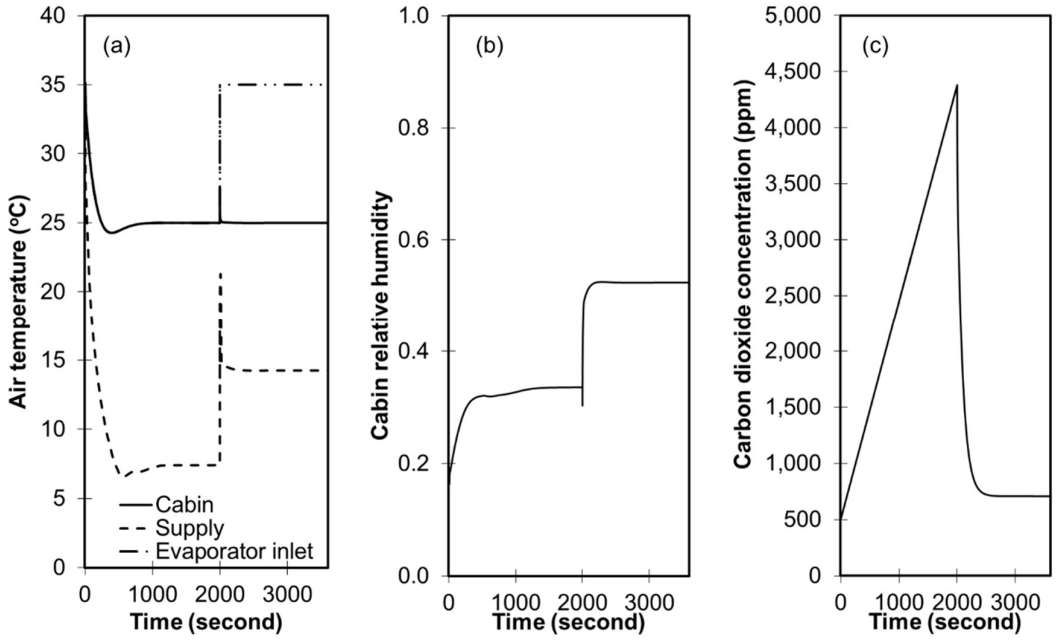

Figure 3.28a shows the moisture condensation rate at the evaporator and airflow rate. When the outdoor air intakes, the condensation rate increases; this is obvious because the outdoor air's humidity ratio is higher than the return air's humidity. Figure 3.28b shows the airflow rate of the air duct system. The airflow rate also increases when the outdoor air intakes. The air with a higher temperature flows into the evaporator and supplies to the cabin. In the meantime, the airflow rate is controlled to satisfy the set cabin temperature, 25 ^{o}C. Thus, the airflow rate should be increased to maintain the set temperature.

Figure 3.28. Ventilation; (a) moisture condensation rate at the evaporator, (b) air flow rate.

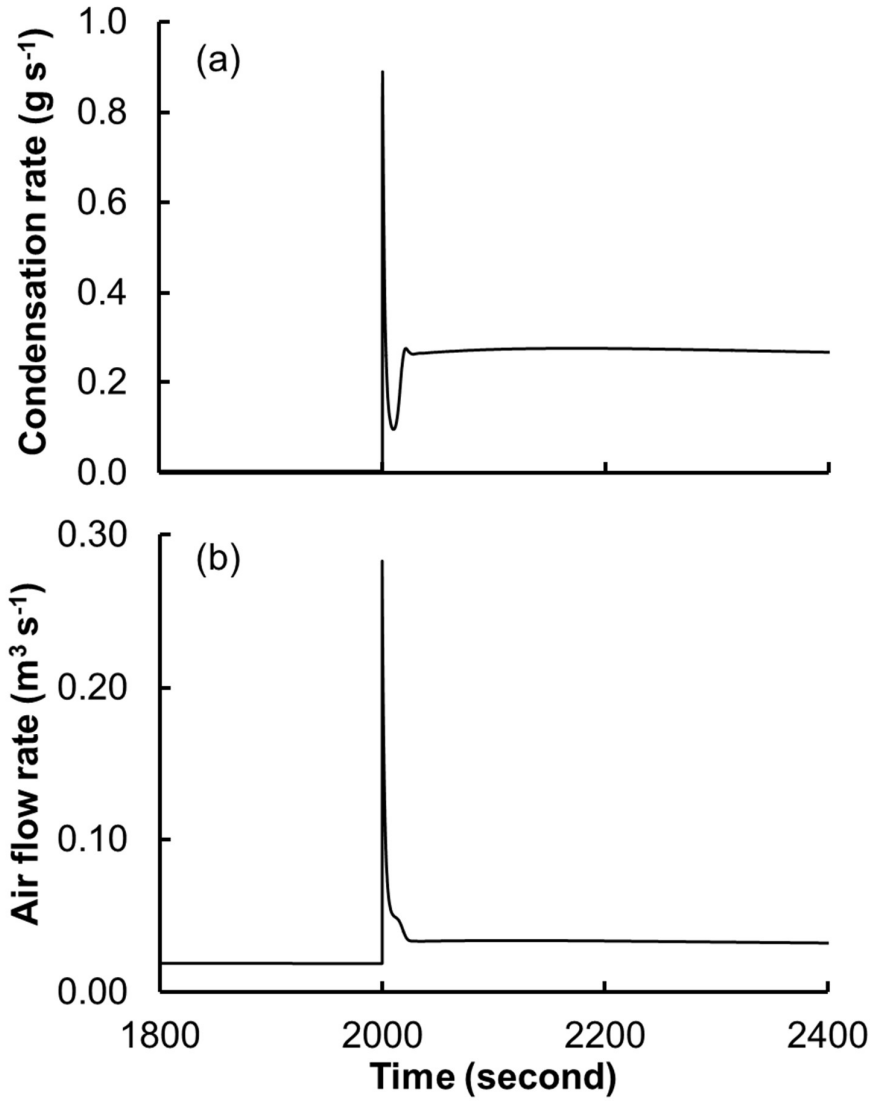

Figure 3.29 shows the behavior and performance of the VCS. The temperature and flow rate of the supply air increase due to the intake of the outdoor air, so the refrigerant temperature at the evaporator temporarily increases but it recovers to 1 ^{o}C; this is because the compressor rotational speed is controlled to keep the set evaporating temperature. The rotational speed increases as shown in Figure 3.29a. To find a new balance point and to maintain the set suction superheating, the expansion valve opening degree increases as shown in Figure 3.29b. Therefore, the refrigerant mass flow rate shown in Figure 3.29c increases but the suction pressure and temperature keep the previous constant value even they change temporarily. Under the fixed evaporator temperature, the rise of the rotational speed and the expansion valve opening leads to the discharge pressure and temperature rise. On the other hand, the cabin cooling load does not change but the system takes the outdoor air which is a higher temperature than the cabin air. This results in the evaporator's cooling capacity increase. In Figure 3.29f, the cooling capacity responds immediately when the outdoor air supplies to the evaporator while it is observed that other parameters change following the responses of the compressor and expansion valve.

Figure 3.29. Ventilation; (a) Compressor rotational speed, (b) orifice cross-sectional area of the expansion valve, (c) refrigerant mass flow rate at the expansion valve outlet, (d) VCS pressure, (e) VCS temperature, and (f) performance of HXs and compressor power.

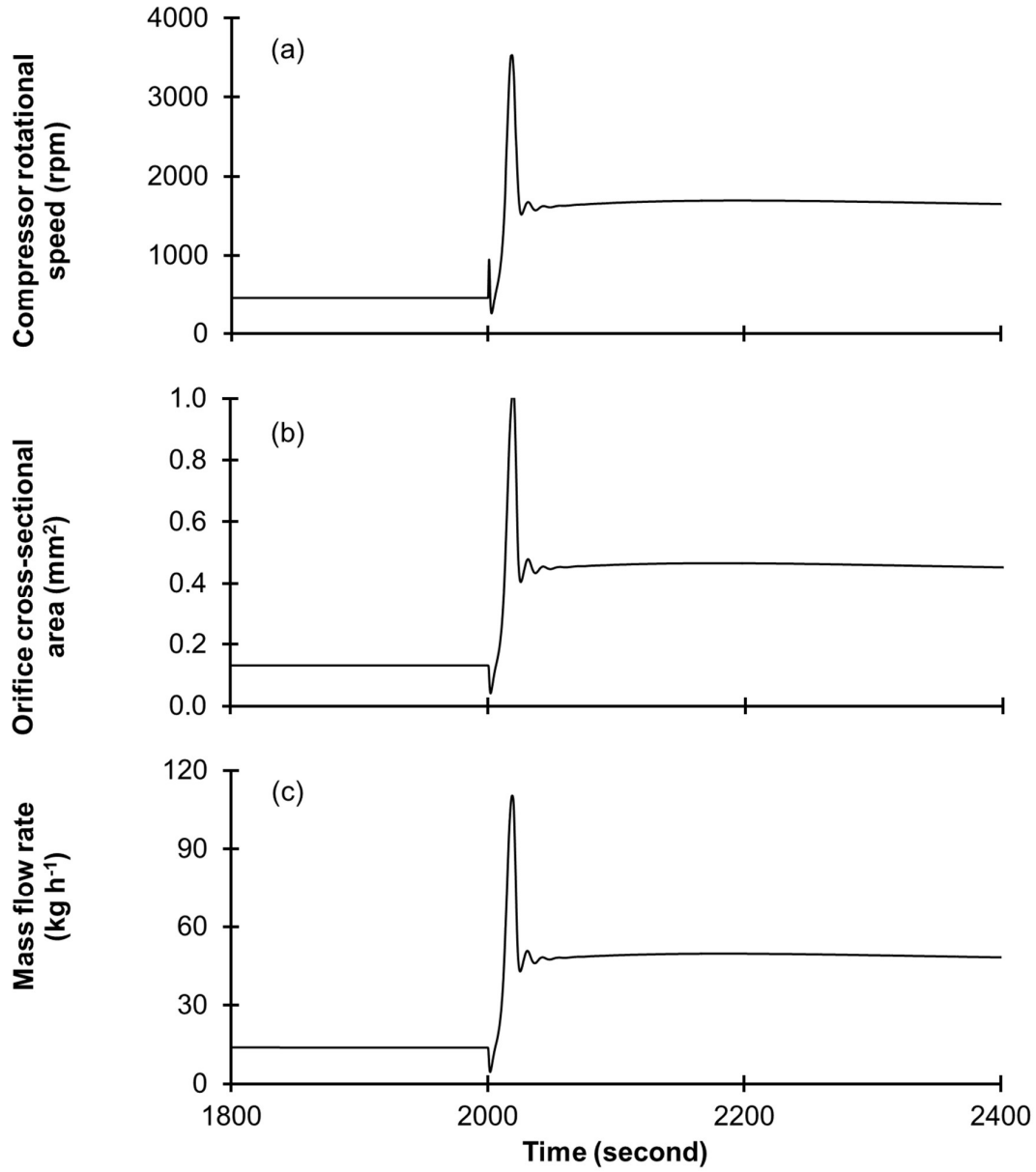

Figure 3.29. continued.

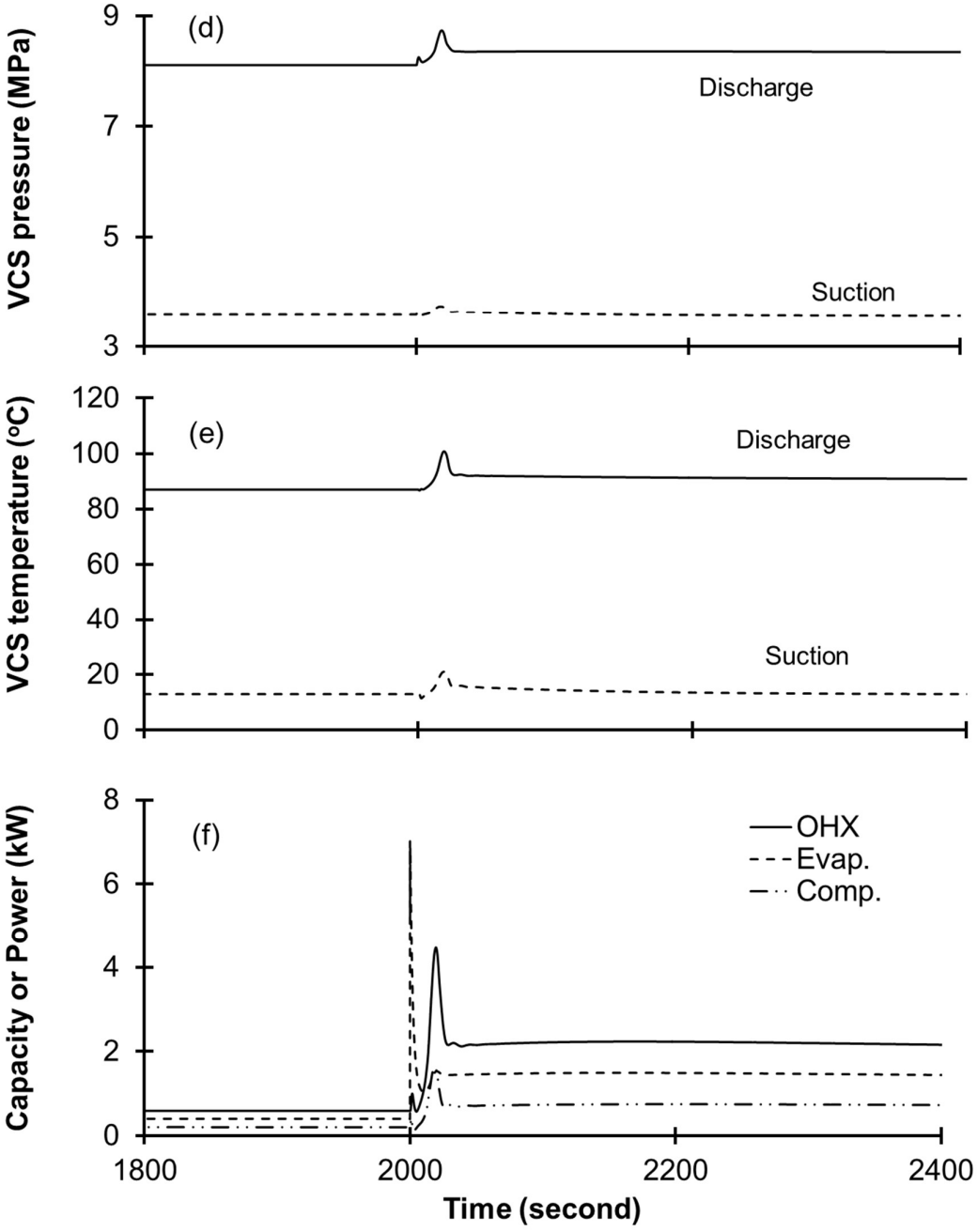

3.7 Supplying Air Temperature Control

Supplying unproperly low-temperature air into the cabin degrades the thermal comfortability of the occupants. To supply the air with proper temperature, ACs adjust the opening ratio of the air blending door (i.e., the second damper) to reheat the low-temperature air using IHX. A part of cooled air flows into the IHX, and the part of the cooled air bypasses the IHX; so, the low-temperature air is blended with the re-heated air then, this blends air supplies into the cabin.

Simulations were conducted with the various opening ratio of the second damper, as shown in Figure 3.30. The system operates without reheating for the pull-down period, then at 2000 seconds, the opening ratio increases to 20%. 500 seconds later, it increases to 40% again.

Figure 3.30. Second damper operation.

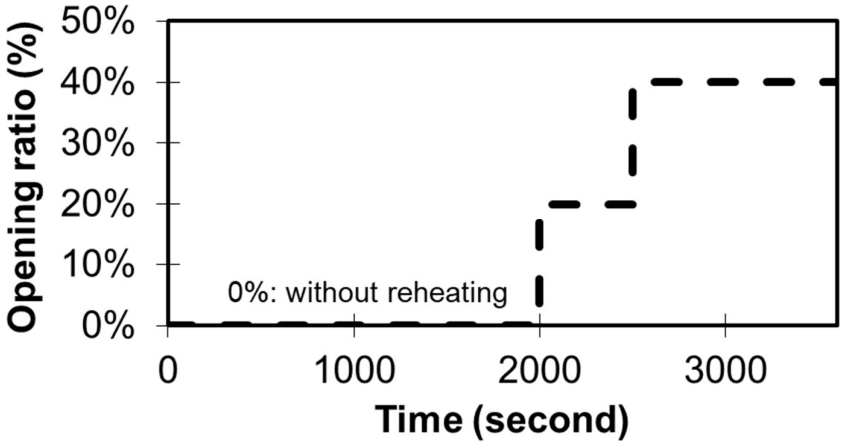

Figure 3.31 shows air temperature in the AHU. Until the system reaches the steady-state (regime A), the supply air temperature indicates 7 ºC. In this regime, the air temperature at the IHX is the same as the refrigerant temperature since there is no heat transfer between the air and refrigerant. When the damper is opened 20% (regime B), the supply air temperature increases to 10.8 ºC. The 20% of airflow having 7 ºC flows into the IHX and is heated to be 64 ºC. 80% of cool airflow bypasses the IHX. The hot and cool air is blended, then the blend air having 10.8 ºC flows into the cabin. When the opening ratio increases to 40% (regime C), the supply air temperature rises to 15 ºC because the airflow rate entering the IHX is increased. The airflow having 7 ºC flows into the IHX and is heated up to be 32 ºC. The hot air of 32 ºC and the cool air of 7 ºC are mixed, then this mixed air having 15 ºC supplies into the cabin. Regardless of the opening ratio, the cabin temperature is maintained for the set temperature, 25 ºC.

Figure 3.31. Air temperature in the AHU.

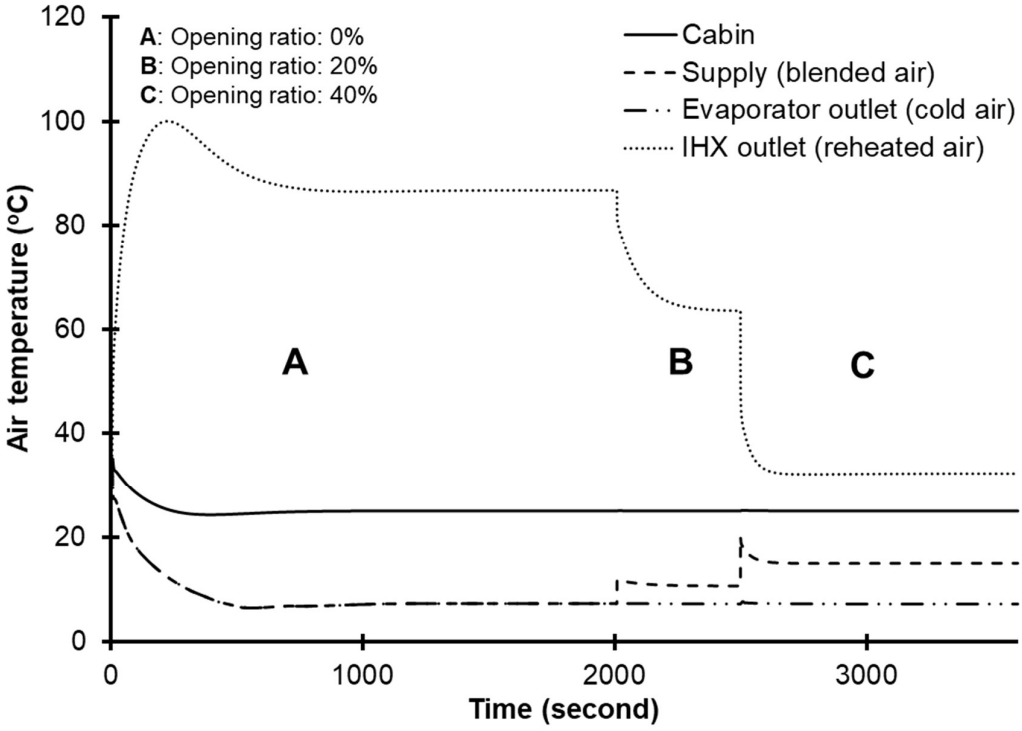

Figure 3.32a shows the moisture condensation rate at the evaporator. When the opening ratio is 0%, the condensation rate is about 0.004 g s^{-1} under the steady-state condition. After the opening ratio suddenly increases, the condensation rate slightly increases. However, after the system is stabilized, the condensation rate approaches the 0.004 g s^{-1} because the moisture generation rate inside the cabin does not change. Figure 3.32b shows the airflow rate. When the opening ratio increases, the airflow rate also increases; this is due to the supply air temperature rise. In this circumstance, the airflow rate should be increased to keep the cabin at the set temperature.

Figure 3.32. Supplying air temperature control; (a) moisture condensation rate at the evaporator and (b) airflow rate.

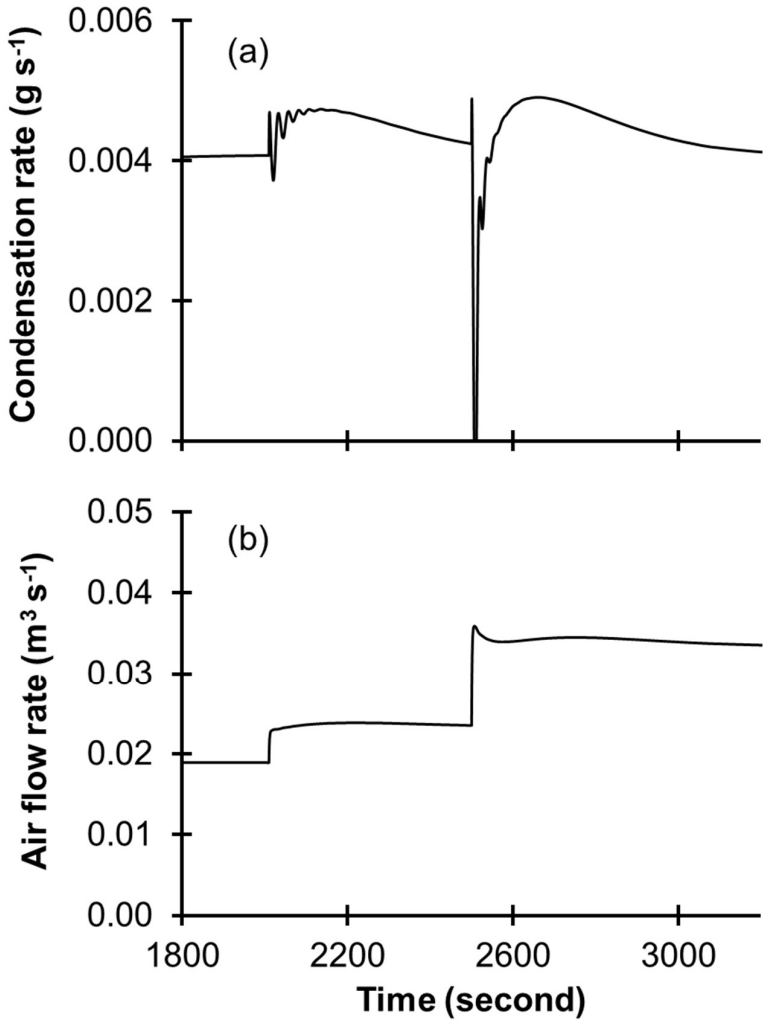

Figure 3.33 depicts the behavior and performance of the VCS. Due to the increase in the air flow rate, the evaporator cooling capacity increase, as shown in Figure 3.33f. So the refrigerant mass flow rate should be increased because the evaporating temperature is fixed. Indeed, the compressor increases the rotational speed (Figure 3.33a), and power consumption also is increased. In series, to balance with the compressor and keep the set suction superheating, the expansion valve opening degree should be increased, as shown in Figure 3.33b. The discharge pressure (Figure 3.33d) temporarily increases due to the slab door opening, but it recovers the previous pressure level. In Figure 3.33e, the refrigerant temperature at the IHX outlet decreases when the slab door opening ratio increase since the heat transfer rate at the IHX increases to heat the cool air, as shown in Figure 3.34.

Figure 3.33. Supplying air temperature control; (a) compressor rotational speed, (b) orifice cross-sectional area of the expansion valve, (c) refrigerant mass flow rate at the expansion valve outlet, (d) VCS pressure, (e) VCS temperature, and (f) performance of HXs and compressor power.

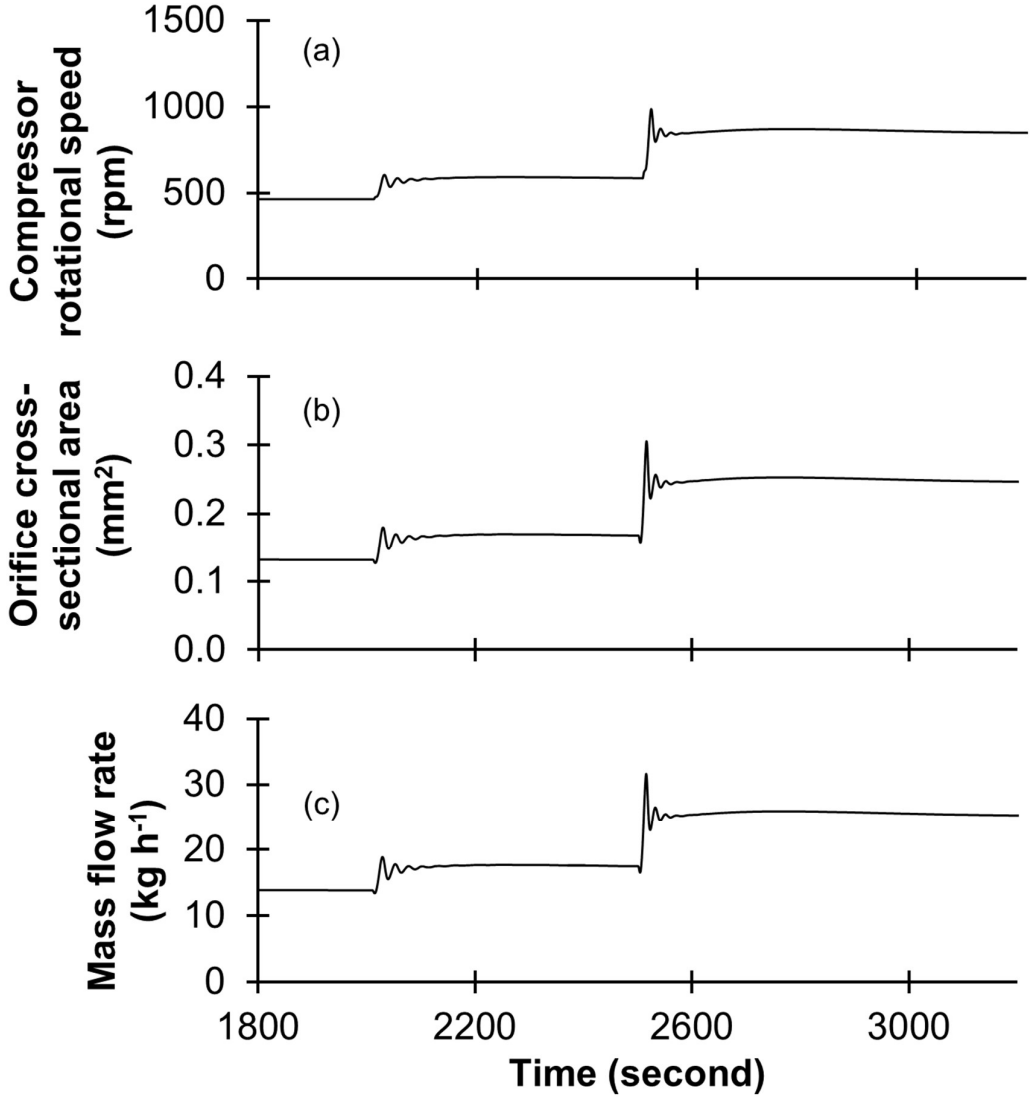

Figure 3.33. continued.

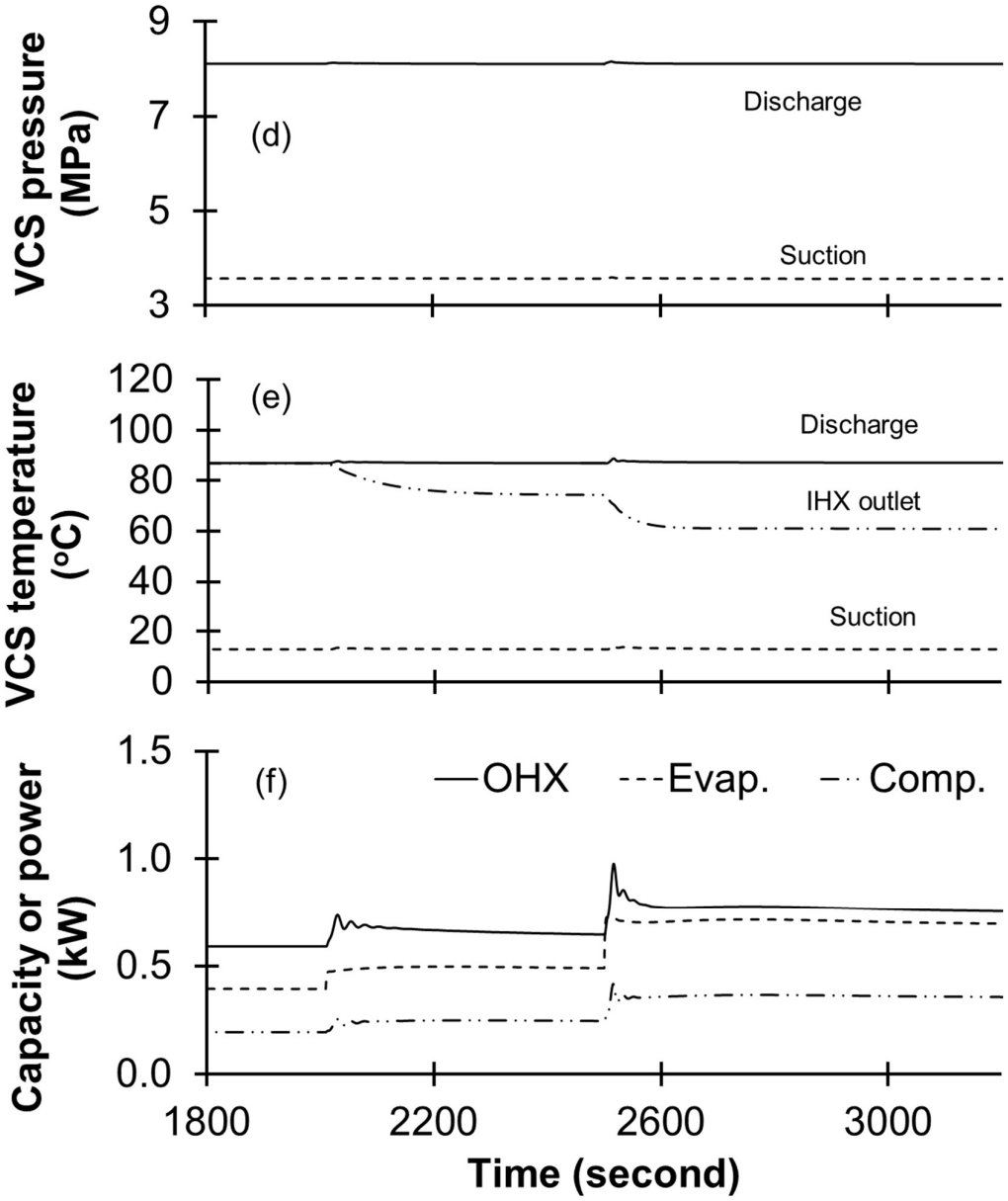

Figure 3.34. Heating capacity of the IHX.

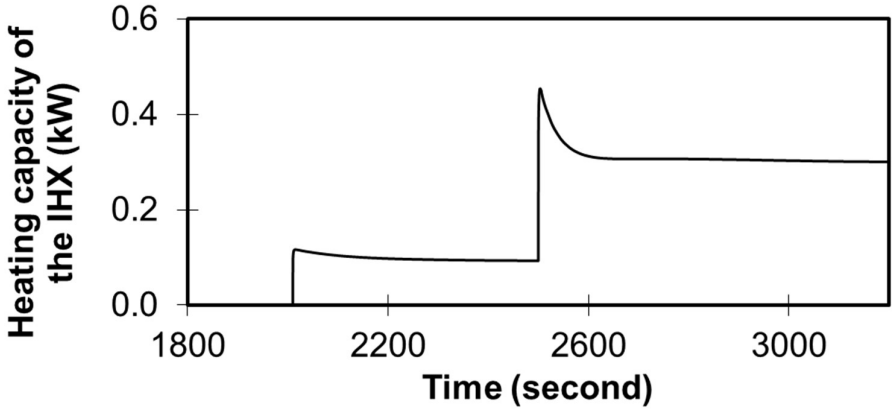

Figure 3.35 shows the air temperature at the evaporator outlet and the supply air temperature against the second slab door's opening ratio. When the opening ratio increases, the more air passes the IHX and be heated; since the more amount of reheated air blends with the cooled air, the supply air temperature increases. With the rise of the supply air temperature, the airflow rate also increases to maintain the cabin temperature to be the set temperature. The air temperature at the evaporator outlet does not increase until the opening ratio is less than 50%, but when it overs 50%, the results indicate that the temperature increases by up to 8.8 ºC.

Figure 3.35. Air temperature and air flow rate with an opening ratio of the second damper.

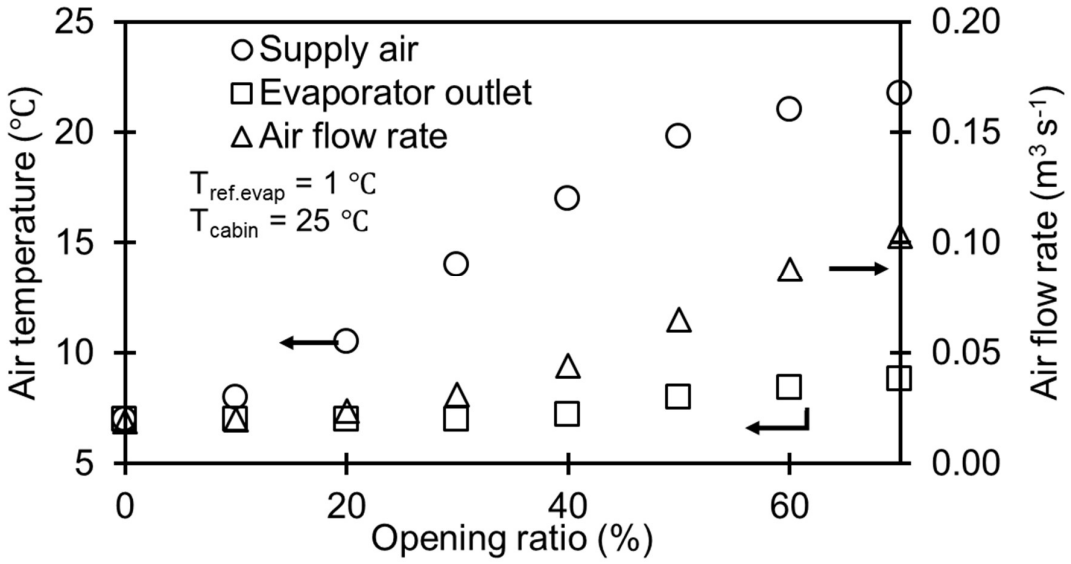

Figure 3.36 shows the supply air temperatures versus the blending door's opening ratio against the various evaporator operating temperatures. The result shows that the supply air temperature increases with the rise of the evaporator operating temperature. When the opening ratio is over 50%, the effect of the evaporator operating temperature is faded out.

Figure 3.36. Supply air temperature versus the second damper opening ratio in various evaporator temperatures.

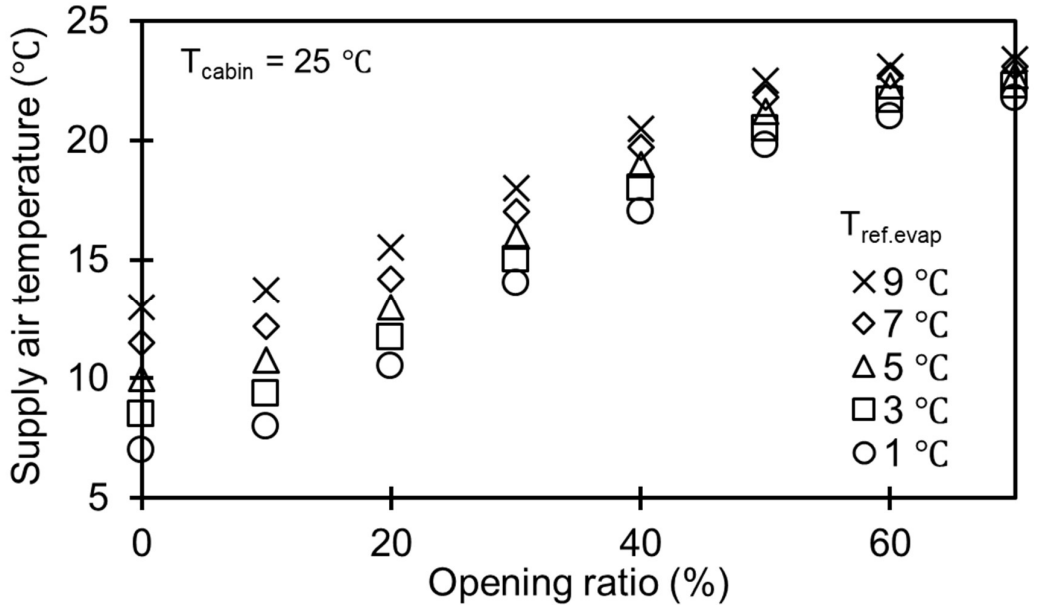

3.8 Optimum Heat Rejection Pressure

A set of simulations was conducted to investigate the optimum heat rejection pressure for the maximum COP. During simulations, the opening degree of the expansion valve was adjusted to control the pressure of the VCS's high-pressure side so that the pressure at the OHX inlet was controlled. Other operating conditions were fixed to be the values provided in Table 2.8.

IntHX gives effects on the system performance and behavior since refrigerant states at the expansion device inlet and the compressor inlet vary with the IntHX's size. Test simulations were conducted several times before proceeding with this investigation and the heat transfer area of the used IntHX was adjusted, so it was set to be a fixed value, 0.09 m^2.

Figure 3.37a shows the system COP against the OHX inlet pressure in the various refrigerant temperatures at the OHX outlet ($T_{ref.OHX.o}$). When the refrigerant temperature at the gas cooler outlet (i.e., OHX outlet) increases, the OHX operating pressure increases, and the system COP decrease due to the compressor power consumption increases. The optimum point of the OHX operating pressures is observed depending on a given temperature. The COP increases with a relatively steep when the OHX operating pressure is less than the threshold value; however, the COP gradually decreases when the operating pressure is beyond the value. This trend can be explained in Figure 3.37b. When the OHX pressure is less than the optimum value ($P_{OHX} < P_{opt}$), a large amount of enthalpy decrease with the pressure increment; this tendency is observed until the pressure approaches the optimum pressure. However, after the pressure is over the optimum value ($P_{OHX} > P_{opt}$), the reduction rate of enthalpy against the pressure increment decreases. Hence, the increasing rate of the heat rejection decreases when the pressure is higher than the optimum pressure, but the compressor power consumption consistently increases due to the large pressure-lift; thus, the COP degrades. The calculated optimum pressure compares to Sarkar et al. (2004)'s correlation that is pre-validated against experimental data by Cabello et al. (2008) and numerical data by Cecchinato et al. (2010). The results are described in Figure 3.38. The present simulation well matches the correlation with an error of 2% as well as the tendency.

Figure 3.37. (a) relationship between the COP and the heat rejection pressure in the various refrigerant temperatures at the OHX outlet and (b) pressure-enthalpy diagram.

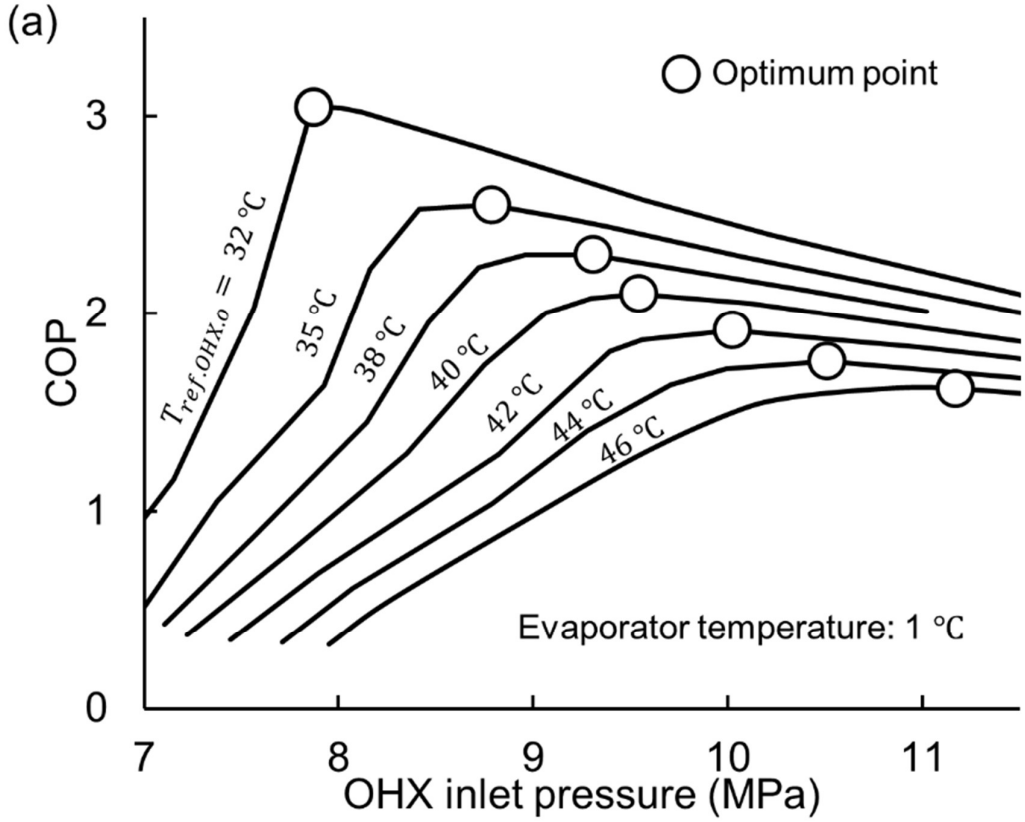

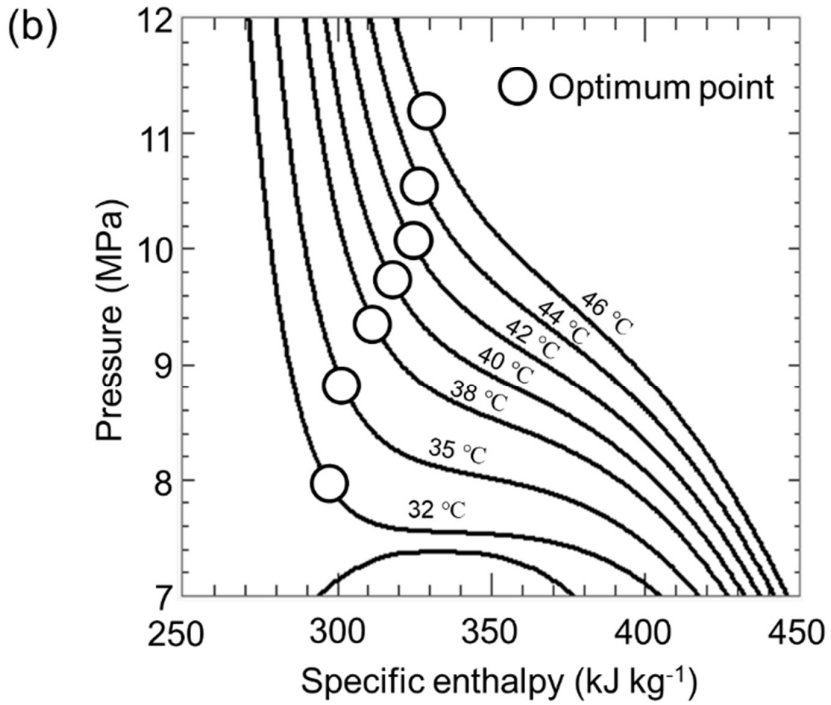

Figure 3.38. Comparison with a correlation.

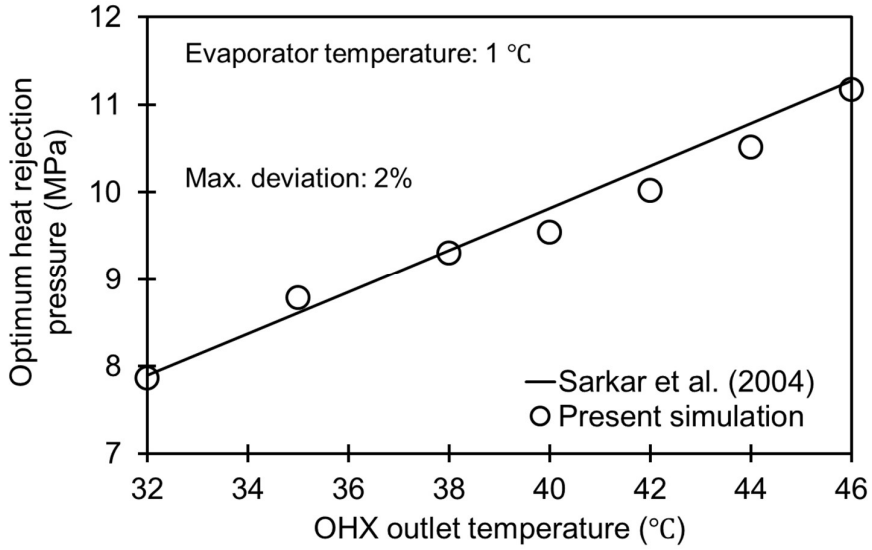

Figure 3.39a shows the system COP against the OHX inlet pressure according to the various operating temperatures of the evaporator ($T_{evap.ref}$). When the evaporator operating temperature decreases, the suction pressure decreases. The lower suction pressure causes larger compressor power, so the system COP decreases. The evaporator temperature does not affect the optimum pressure significantly; the relative deviation of the optimum pressure is 0.7% when the evaporator temperature is 5 ºC and 1 ºC. Chen and Gu (2005) reported that the biggest deviation of the optimum gas cooler pressure is 0.2 MPa when the evaporating temperature changes from 10 ºC to -10 ºC. This amount of deviation corresponds to 1.99%. Figure 3.39b shows the optimum gas cooler pressure calculated by Sarkar et al. (2004) correlation when the evaporator temperature varies from 5 ºC to -5 ºC. The maximum deviation of the optimum pressure is 2.4%. Meanwhile, in Figure 3.39a, the optimum pressure decreases slightly with an increase in evaporator temperature, and this tendency is also observed in Figure 3.39b.

Figure 3.39. (a) COP and the heat rejection pressure in various evaporator temperatures and (b) the optimum heat rejection pressure calculated by the correlation (Sarkar et al., 2004).

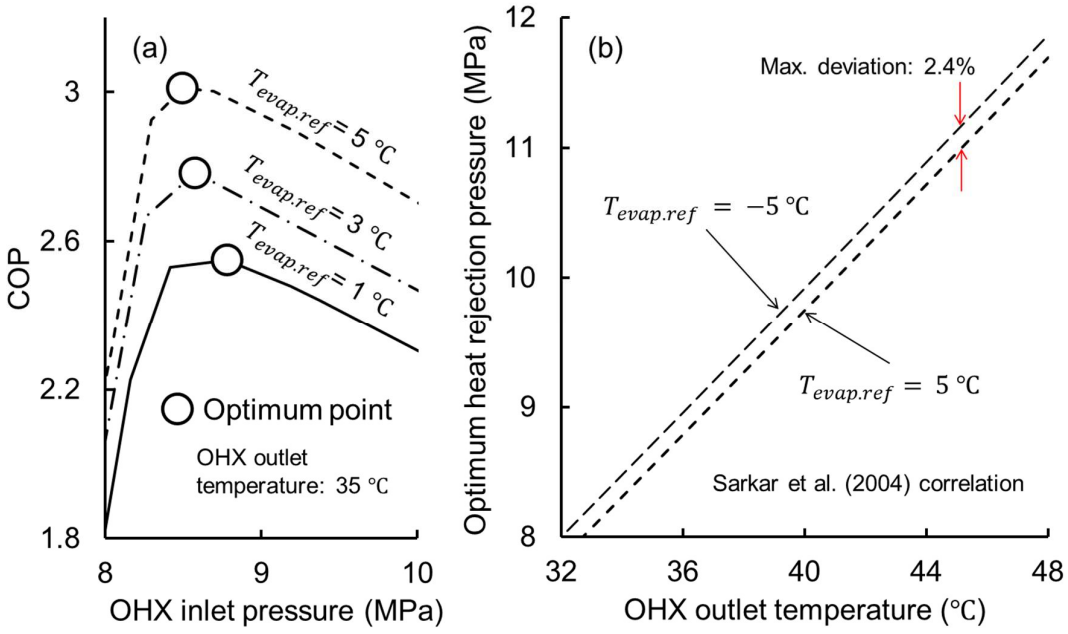

Figure 3.40 shows the comparison results of the transient performance of the system with and without the control for the gas cooler pressure. The simulation was conducted when the OHX outlet temperature fluctuates within the range of 32 ^{o}C to 45 ^{o}C. During simulations, the compressor rotational speed and AHU air flow rate were controlled by the PI control to meet the set evaporator temperature (1 ^{o}C) and the set cabin temperature (25 ^{o}C), respectively. The mean velocity of the air at the OHX was fixed to be a constant value, 60 km h^{-1}. The relationship of the optimum gas cooler pressure with the orifice cross-sectional area was obtained from a set of simulations, the opening degree of the orifice was controlled according to the relationship to control the pressure. In Figure 3.40, the system COP under the control indicates a higher value, approximately 1, than the COP without the control. The tendency of COPs for both cases shows a reversed pattern against the OHX outlet temperature fluctuation; this is because the higher outlet temperature brings the higher gas cooler operating pressure, regardless of the optimum control implementation.

Figure 3.40. COPs with and without control; (a) OHX outlet temperature, (b) OHX inlet pressure, (c) deviation of the pressure, and (d) COP.

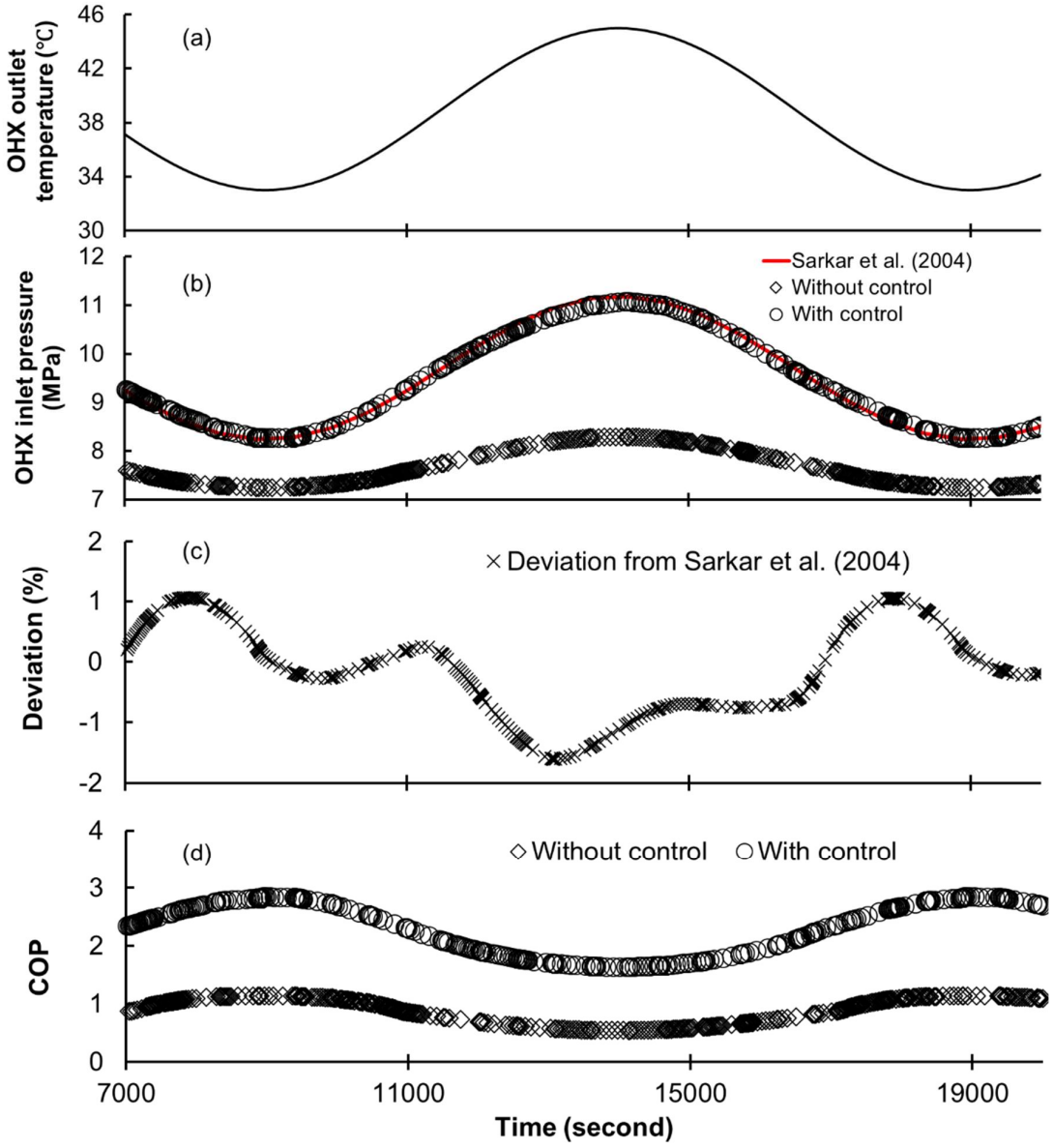

Chapter 4 Conclusion

In this work, an AC model for electric vehicles was established using commercial software offering acausal, equation-based, and object-oriented modeling approaches. The AC model consists of three subsystem models, R-744 VCS, AHU, and cabin. Each model was validated, and the corresponding results state that the present models simulate an actual system's dynamic behavior and performance, reasonably. Transient analysis on an R-744 AC for electric vehicles was carried out using the integrated model.

The AC consumes tremendous energy during the start-up and cabin pull-down operation to achieve a target cabin temperature, and the COP degradation is observed during that period; the outdoor and indoor thermal conditions influence the energy consumption and pull-down time in the order of initial cabin temperature, cabin target temperature, number of occupants, initial cabin RH, and solar irradiance. Concerning ventilation operation, intake of relatively high-temperature and high-humidity outdoor air results in a cooling load increase, thus, the compressor consumes more energy. An increase in air temperature supplying to the cabin increases the cooling load on the AC, under the same cabin set temperature. Considering that the average duration of a single driving for business and personal is about 30 minutes (Pasaoglu et al., 2012), the average operation time of the automobile AC is probably less than 30 minutes. From the present investigation, it is observed that the compressor in a vehicle AC consumes enormous energy for the initial pull-down operation during the 30 minutes; this amount of energy consumption changes with the given initial condition of the cabin and outdoor thermal environments. Besides, the size of cabin space, the materials of structures, the type of refrigerant used, and AC's size can be other factors on that initial energy consumption. Therefore, the amount of energy consumption in the start-up and pull-down period is worth considering in the preliminary designing phase for an electric vehicle AC, since electric vehicles should reduce overall energy consumption to secure a certain level of mileage.

The effect of system operating parameters on the COP was also investigated; the results showed that heat rejection pressure and refrigerant temperature at the main gas cooler's outlet affect the COP markedly. The optimum heat rejection pressure ensuring the maximum COP was clearly observed, and the results are well-matched with that of the literature. The optimum heat rejection pressure highly depends on the refrigerant temperature at the OHX outlet while the evaporator operating condition has a relatively tiny effect on the optimum heat rejection pressure. The COP of the AC controlled for optimal heat removal

pressure was compared to the COP of the AC otherwise. The comparison results showed that the COP operating under control is superior to that without control. The result demonstrates that a proper control strategy can improve the performance of an R-744 AC, remarkably. Hence, it is expected that an electric vehicle can achieve additional energy-saving potential with real-time control on heat rejection pressure, thereby it can secure further extended mileage.

This integrated model was established to understand the transient characteristics of a prototype quickly and estimate its dynamic performance in prompt, by implementing system-scale simulation rapidly in the preliminary stage of the entire production process of a real system. Hence, it can contribute to shortening the prototyping process with a relatively small cost. However, it is difficult to investigate thermofluid characteristics in a specific component with this model. For example, the model with the current form cannot capture a local characteristic of heat transfer in an HX nor track its time-dependent change. To implement this, more segments are necessary, however in doing so, computational cost increases. Separate modeling for a specific component and running simulations can be another solution.

Commercial, industrial, and residential systems utilize an oil separator to avoid the compressor's lubricant oil circulate the system with the refrigerant; however, it is rarely used for automobile AC (Li et al., 2021; Zhang et al., 2018). The effect of oil on the performance of an automobile AC is an important issue. Overall, lubricant oil decreases heat transfer performance and increases pressure drop, in R-744 flow boiling (Dang et al., 2013) and gas cooling conditions (Yun et al., 2007). Particularly, the effects of the oil concentration on the convective gas cooling heat transfers and pressure drops of the supercritical R-744/oil mixture in mini-channel tubes ($D_h \leq 1$ mm) are significant (Yun et al., 2007). Meanwhile, the current model does not take into consideration such lubricating oil effects. For further practical applications, properties of the R-744/oil mixture should be considered for future work.

Furthermore, regarding the evaporator operating temperature, a clear reference has not been known, however typically it avoids decreasing below 0 ^{o}C; unless it does, moisture in the air flow can be frozen on the evaporator exterior surface. Whiles, if the evaporator operates under a needlessly low-temperature, AC consumes energy more than necessary. Hence, the maximum allowable evaporator operating temperature should be found and used depending on given conditions; this operation can minimize the energy consumption of the compressor and reduce the additional energy usage to reheat air to the desired supplying temperature to the cabin. Also, the humidity of moist-air leaving evaporator depends on

evaporator operating temperature; control on the evaporator temperature can offer indoor thermal comfort with better quality. The current work does not provide the relationship between evaporator temperature, cabin humidity, and energy consumption. Further investigation on that will be necessary for the future, and a suitable control strategy based on that data should be given.

References

Alahmer, A., Mayyas, A., Mayyas, A. A., Omar, M. A., & Shan, D. (2011). Vehicular thermal comfort models; a comprehensive review. *Applied Thermal Engineering*, *31*(6-7), 995-1002. https://doi.org/10.1016/j.applthermaleng.2010.12.004.

ANSI/ASHRAE Standard 34 (2019).

ANSI/ASHRAE Standard 55 (2020).

Ap, N. S., Guyonvarch, G., Cloarec, M., & Rouveyre, L. (2000). Cooling system and climate control of fuel cell electric vehicle (FCEV). In EVS17 Congress, Montreal, Canada.

ASHRAE Handbook: Fundamentals (2001).

Atam, E. (2017). Current software barriers to advanced model-based control design for energy-efficient buildings. *Renewable and Sustainable Energy Reviews*, *73*, 1031-1040. https://doi.org/10.1016/j.rser.2017.02.015.

Bandhauer, T. M., Garimella, S., & Fuller, T. F. (2011). A critical review of thermal issues in lithium-ion batteries. *Journal of The Electrochemical Society*, *158*(3), Article R1. https://iopscience.iop.org/article/10.1149/1.3515880.

Barret, K. E., Boitano, S., & Barman, S. M. (Eds.). (2012). *Ganong's review of medical physiology*. McGraw-Hill Medical.

Berry, E. (1914). Relative humidity of expired air. *American Physical Education Review*, *19*(6), 452-454. https://doi.org/10.1080/23267224.1914.10651422.

Boewe, D., Yin, J., Park, Y. C., Bullard, C. W., & Hrnjak, P. S. (1999). The role of suction line heat exchanger in transcritical R744 mobile AC systems (No. 1999-01-0583). *SAE Technical Paper*. https://doi.org/10.4271/1999-01-0583.

Boewe, D. E., Bullard, C. W., Yin, J. M., & Hrnjak, P. S. (2001). Contribution of internal heat exchanger to transcritical R-744 cycle performance. *HVAC&R Research*, *7*(2), 155-168. https://doi.org/10.1080/10789669.2001.10391268.

Brown, J. S., Yana-Motta, S. F., & Domanski, P. A. (2002). Comparitive analysis of an automotive air conditioning systems operating with CO_2 and R134a. *International Journal of Refrigeration*, *25*(1), 19-32. https://doi.org/10.1016/S0140-7007(01)00011-1.

Budde-Meiwes, H., Drillkens, J., Lunz, B., Muennix, J., Rothgang, S., Kowal, J., & Sauer, D. U. (2013). A review of current automotive battery technology and future prospects. *Proceedings of the Institution of Mechanical Engineers, Part D: Journal of Automobile Engineering*, *227*(5), 761-776.

https://doi.org/10.1177/0954407013485567.

Bukhari, S. M. A. S., Maqsood, J., Baig, M. Q., Ashraf, S., & Khan, T. A. (2015). Comparison of characteristics-lead acid, nickel based, lead crystal and lithium based batteries. *Proceedings of 2015 17th UKSim-AMSS International Conference on Computer Modelling and Simulation,* 444-450, IEEE. http://doi.org/10.1109/UKSim.2015.69.

Cabello, R., Sánchez, D., Llopis, R., & Torrella, E. (2008). Experimental evaluation of the energy efficiency of a CO_2 refrigerating plant working in transcritical conditions. *Applied Thermal Engineering*, *28*(13), 1596-1604. https://doi.org/10.1016/j.applthermaleng.2007.10.026.

Cecchinato, L., Corradi, M., & Minetto, S. (2010). A critical approach to the determination of optimal heat rejection pressure in transcritical systems. *Applied Thermal Engineering*, *30*(13), 1812-1823. https://doi.org/10.1016/j.applthermaleng.2010.04.015.

Cecchinato, L., Corradi, M., Cosi, G., Minetto, S., & Rampazzo, M. (2012). A real-time algorithm for the determination of R744 systems optimal high pressure. *International Journal of Refrigeration*, *35*(4), 817-826. https://doi.org/10.1016/j.ijrefrig.2012.01.005.

Cengel, Y. A., & Boles, M. A. (2007). *Thermodynamics: An Engineering Approach 6th Editon (SI Units)*. The McGraw-Hill Companies, Inc., New York.

Chen, J. C. (1966). Correlation for boiling heat transfer to saturated fluids in convective flow. *Industrial & Engineering Chemistry Process Design and Development*, *5*, 322-329. https://pubs.acs.org/doi/pdf/10.1021/i260019a023.

Chen, Y., & Gu, J. (2005). The optimum high pressure for CO_2 transcritical refrigeration systems with internal heat exchangers. *International Journal of Refrigeration*, *28*(8), 1238-1249. https://doi.org/10.1016/j.ijrefrig.2005.08.009.

Cho, H., Ryu, C., & Kim, Y. (2007). Cooling performance of a variable speed CO_2 cycle with an electronic expansion valve and internal heat exchanger. *International Journal of Refrigeration*, *30*, 664-671. https://doi.org/10.1016/j.ijrefrig.2006.10.004.

Churchill, S. W., & Chu, H. H. (1975). Correlating equations for laminar and turbulent free convection from a vertical plate. *International Journal of Heat and Mass Transfer*, *18*(11), 1323-1329. https://doi.org/10.1016/0017-9310(75)90243-4.

Dang, C., Haraguchi, N., Yamada, T., Li, M., & Hihara, E. (2013). Effect of lubricating oil on flow boiling heat transfer of carbon dioxide. *International journal of refrigeration*, *36*(1), 136-144. https://doi.org/10.1016/j.ijrefrig.2012.09.020.

Dassault Systemes®. Dymola: Dynamic Modeling Laboratory. https://www.3ds.com/products-services/catia/products/dymola/. (accessed December 10th, 2020).

Dhami, P.S., Chopra, G., & Shrivastava, H.N. (2015). *A Textbook of Biology*. Jalandhar, Punjab: Pradeep Publications.

Ding, G. L. (2007). Recent developments in simulation techniques for vapor-compression refrigeration systems. *International Journal of Refrigeration*, *18*, 1119-1133. https://doi.org/10.1016/j.ijrefrig.2007.02.001.

Dong, J., Wang, Y., Jia, S., Zhang, X., Hwang, L. (2021). Experimental study of R744 heat pump system for electric vehicle application. *Applied Thermal Engineering*, *183*, Article 116191. https://doi.org/10.1016/j.applthermaleng.2020.116191.

DuBois, D., & DuBois, E. F. (1915). Fifth paper the measurement of the surface area of man. *Archives of Internal Medicine*, *15*(5_2), 868-881. https://doi.org/10.1001/archinte.1915.00070240077005.

Dunn, B., Kamath, H., & Tarascon, J. M. (2011). Electrical energy storage for the grid: a battery of choices. *Science*, *334*(6058), 928-935. https://doi.org/10.1126/science.1212741.

Elsheikh, A., Widl, E., Pensky, P., Dubisch, F., Brychta, M., Basciotti, D., & Müller, W. (2013). Modelica-enabled rapid prototyping via TRNSYS. *Proceedings of 13th International Conference of the International Building Performance Simulation Association*. 3291-3298. http://www.ibpsa.org/proceedings/BS2013/p_1414.pdf.

Etacheri, V., Marom, R., Elazari, R., Salitra, G., & Aurbach, D. (2011). Challenges in the development of advanced Li-ion batteries: a review. *Energy and Environmental Science*, *4*(9), 3243–3262. https://doi.org/10.1039/C1EE01598B.

Fang, X. (2013). A new correlation of flow boiling heat transfer coefficients for carbon dioxide. *International Journal of Heat and Mass Transfer*, *64*, 802-807. https://doi.org/10.1016/j.ijheatmasstransfer.2013.05.024.

Farrington, R., Cuddy, M., Keyser, M., & Rugh, J. (1999). *Opportunities to reduce air-conditioning loads through lower cabin soak temperatures* (No. NREL/CP-540-26615). National Renewable Energy Lab., Golden, CO (US). https://www.osti.gov/servlets/purl/9822.

Farrington, R., & Rugh, J. (2000). *Impact of vehicle air-conditioning on fuel economy, tailpipe emissions, and electric vehicle range* (No. NREL/CP-540-28960). National Renewable Energy Lab., Golden, CO (US).

https://www.nrel.gov/docs/fy00osti/28960.pdf.

Gado, A. (2006). *Development of a dynamic test facility for environmental control systems* [Doctoral dissertation, University of Maryland]. https://drum.lib.umd.edu/bitstream/handle/1903/3391/umi-umd-3203.pdf;sequence=1.

Gado, A., Hwang, Y., & Radermacher, R. (2008). Dynamic behavior of mobile air-conditioning systems. *HVAC&R Research*, *14*(2), 307-321. https://doi.org/10.1080/10789669.2008.10391010.

Ghiaasiaan, S. M. (2007). *Two-phase flow, boiling, and condensation: in conventional and miniature systems*. Cambridge University Press.

Giraud, L., Bavière, R., & Paulus, C. (2014). Modeling of solar district heating: a comparison between TRNSYS and MODELICA. *Proceedings of EuroSun 2014*. http://proceedings.ises.org/paper/eurosun2014/eurosun2014-0081-Giraud.pdf.

Gnielinski, V. (1976). New equations for heat and mass transfer in turbulent pipe and channel flow. *International Chemical Engineering*, *16*, 359-368.

Haaland, S. E. (1983). Simple and explicit formulas for the friction-factor in turbulent pipe flow. *Journal of Fluids Engineering*, *105*(1), 89-90. https://doi.org/10.1115/1.3240948.

Hermes, C. J., & Melo, C. (2008). A first-principles simulation model for the start-up and cycling transients of household refrigerators. *International Journal of Refrigeration*, *31*(8), 1341-1357. https://doi.org/10.1016/j.ijrefrig.2008.04.003.

International Energy Agency (IEA). (2020). Technology report; Global EV outlook 2020, June. https://www.iea.org/reports/global-ev-outlook-2020.

Incropera, F. P., Lavine, A. S., Bergman, T. L., & DeWitt, D. P. (2007). *Fundamentals of heat and mass transfer*. Wiley.

Jamila, E., & Abdelmjid, S. (2014). Physical network approach applied to wind turbine modeling with simscape language. *Open Journal of Modelling and Simulation*, *2*, 77-89. http://dx.doi.org/10.4236/ojmsi.2014.22010.

Japan Meteorological Agency, https://www.jma.go.jp/jma/index.html. (accessed January 23rd, 2021).

Jin, J., Chen, J., & Chen, Z. (2011). Development and validation of a microchannel evaporator model for a CO_2 air-conditioning system. *Applied Thermal Engineering*, *31*, 137-146. https://doi.org/10.1016/j.applthermaleng.2010.06.019.

Karn, A., Chintala, V., & Kumar, S. (2019). An investigation into sky temperature estimation, its variation, and significance in heat transfer calculations of solar cookers. *Heat*

Transfer-Asian Research, *48*(5), 1830-1856. https://doi.org/10.1002/htj.21459.

Kauf, F. (1999). Determination of the optimum high pressure for transcritical CO_2-refrigeration cycles. *International Journal of Thermal Science,* 38, 325-330. https://doi.org/10.1016/S1290-0729(99)80098-2.

Khayyam, H., Kouzani, A. Z., Hu, E. J., & Nahavandi, S. (2011a). Coordinated energy management of vehicle air conditioning system. *Applied Thermal Engineering*, *31*(5), 750-764. https://doi.org/10.1016/j.applthermaleng.2010.10.022.

Khayyam, H., Nahavandi, S., Hu, E., Kouzani, A., Chonka, A., Abawajy, J., Marano, V., & Davis, S. (2011b). Intelligent energy management control of vehicle air conditioning via look-ahead system. *Applied Thermal Engineering*, *31*(16), 3147-3160. https://doi.org/10.1016/j.applthermaleng.2011.05.023.

Khayyam, H., Abawajy, J., & Jazar, R. N. (2012). Intelligent energy management control of vehicle air conditioning system coupled with engine. *Applied Thermal Engineering*, *48*, 211-224. https://doi.org/10.1016/j.applthermaleng.2012.04.050.

Khayyam, H. (2013). Adaptive intelligent control of vehicle air conditioning system. *Applied Thermal Engineering*, *51*, 1154-1161. https://doi.org/10.1016/j.applthermaleng.2012.10.028.

Kim, M. H., Pettersen, J., & Bullard, C. W. (2004). Fundamental process and system design issues in CO_2 vapor compression systems. *Progress in Energy and Combustion Science*, *30*(2), 119-174. https://doi.org/10.1016/j.pecs.2003.09.002.

Kim, S. C., Kim, M. S., Hwang, I. C., & Lim, T. W. (2007a). Performance evaluation of a CO_2 heat pump system for fuel cell vehicles considering the heat exchanger arrangements. *International Journal of Refrigeration*, *30*, 1195-1206. https://doi.org/10.1016/j.ijrefrig.2007.02.008.

Kim, S. C., Kim, M. S., Hwang, I. C., & Lim, T. W. (2007b). Heating performance enhancement of a CO_2 heat pump system recovering stack exhaust thermal energy in fuel cell vehicles. *International Journal of Refrigeration*, *30*, 1215-1226. https://doi.org/10.1016/j.ijrefrig.2007.02.002.

Kim, S. C., Won, J. P., & Kim, M. S. (2009). Effects of operating parameters on the performance of a CO_2 air conditioning system for vehicles. *Applied Thermal Engineering*, *29*, 2408-2416. https://doi.org/10.1016/j.applthermaleng.2008.12.017.

Kim, M. S., Shin, C. S., & Kim, M. S. (2014). A study on the real time optimal control method for heat rejection pressure of a CO_2 refrigeration system with an internal heat exchanger. *International journal of refrigeration*, *48*, 87-99.

https://doi.org/10.1016/j.ijrefrig.2014.09.014.

Kiss, T., Chaney, L., & Meyer, J. (2013). A new automotive air conditioning system simulation tool developed in MATLAB/Simulink. *SAE International Journal of Passenger Cars – Mechanical Systems, 6*(2). https://doi.org/10.4271/2013-01-0850.

Klein, S.A., Duffie, J.A., & Beckman, W.A. (1976). TRNSYS - A transient simulation program, *ASHRAE Transaction, 82*(1), 623-633.

Ko, J., Takata, N., Thu, K., & Miyazaki, T. (2020). Dynamic modeling and validation of a carbon dioxide heat pump system. *Evergreen, 7*(2), 172-194. https://doi.org/10.5109/4055215.

Ko, J., Thu, K., & Miyazaki, T. (2021a). Investigation of a cascaded CO_2 refrigeration system using phase change materials for energy-saving potentials. *Applied Thermal Engineering, 182*, Article 116104. https://doi.org/10.1016/j.applthermaleng.2020.116104.

Ko, J., Thu, K., & Miyazaki, T. (2021b). Transient analysis of an electric vehicle air-conditioning system using CO_2 for start-up and cabin pull-down operations. *Applied Thermal Engineering, 190*, Article 116825. https://doi.org/10.1016/j.applthermaleng.2021.116825.

Kuang, G. (2006). *Heat transfer and mechanical design analysis of supercritical gas cooling process of CO_2 in microchannels* [Doctoral dissertation, University of Maryland]. http://hdl.handle.net/1903/4278.

Lee, D., & Hwang, S. (2019). Development Trends of Refrigerant and Refrigerant Oil for Automotive Air-conditioner. *Tribology and Lubricants*, *35*(4), 206-214. http://doi.org/10.9725/kts.2019.35.4.206.

Lambert, M. A., & Jones, B. J. (2006). Automotive adsorption air conditioner powered by exhaust heat. Part 1: conceptual and embodiment design. *Proceedings of the Institution of Mechanical Engineers, Part D: Journal of Automobile Engineering*, *220*(7), 959-972. https://doi.org/10.1243/09544070JAUTO221.

Lemmon, E. W., Bell, I. H., Huber, M. L., & McLinden, M. O. (2018). Reference Fluid Thermodynamic and Transport Properties-REFPROP Ver. 10.0. *National Institute of Standards and Technology*. *Boulder, CO, USA.*

Li, B., & Alleyne, A. G. (2010). A dynamic model of a vapor compression cycle with shut-down and start-up operations. *International Journal of Refrigeration*, *33*(3), 538-552. https://doi.org/10.1016/j.ijrefrig.2009.09.011.

Li, B., Peuker, S., Hrnjak, P. S., & Alleyne, A. G. (2011). Refrigerant mass migration

modeling and simulation for air conditioning systems. *Applied Thermal Engineering*, *31*(10), 1770-1779. https://doi.org/10.1016/j.applthermaleng.2011.02.022.

Li, K., Luo, S., Wang, Z., Zhang, H., Su, L., Fang, Y., Zhou, X., Zhang, H., & Tu, R. (2021). An experimental investigation of oil circulation ratio influence on heating performance in an air condition heat pump system for electrical vehicles. *International Journal of Refrigeration*, *122*, 220-231. https://doi.org/10.1016/j.ijrefrig.2020.11.007.

Li, W., & Sun, J. (2013). Numerical simulation and analysis of transport air conditioning system integrated with passenger compartment. *Applied Thermal Engineering*, *50*(1), 37-45. https://doi.org/10.1016/j.applthermaleng.2012.05.030.

Liao, S. M., Zhao, T. S., & Jakobsen, A. (2000). Correlation of optimal heat rejection pressures in transcritical carbon dioxide cycles. *Applied Thermal Engineering*, *20*(9), 831-841. https://doi.org/10.1016/S1359-4311(99)00070-8.

Lim, D. K., Ahn, B. H., & Jeong, J. H. (2018). Method to control an air conditioner by directly measuring the relative humidity of indoor air to improve the comfort and energy efficiency. *Applied energy*, *215*, 290-299. https://doi.org/10.1016/j.apenergy.2018.02.004.

Liu, H., Chen, J., & Chen, Z. (2005). Experimental investigation of a CO_2 automotive air conditioner. *International Journal of Refrigeration*, *28*(8), 1293-1301. https://doi.org/10.1016/j.ijrefrig.2005.08.011.

Lloyd, J. R., & Moran, W. R. (1974). Natural convection adjacent to horizontal surface of various platforms. *Journal of Heat Transfer*, *96*(4), 443-447. https://doi.org/10.1115/1.3450224.

Lorentzen, G., & Pettersen, J. (1992). *New possibilities for non-CFC refrigeration* (No. NEI-NO--425).

Lorentzen, G., & Pettersen, J. (1993). A new, efficient and environmentally benign system for car air-conditioning. *International Journal of Refrigeration*, *16*(1), 4-12. https://doi.org/10.1016/0140-7007(93)90014-Y.

Lowe, M., Tokuoka, S., Trigg, T., & Gereffi, G. (2010). Lithium-ion batteries for electric vehicles: The U.S. value chain*, Center on Globalization, Governance & Competitiveness*, Duke University, US. https://millenniumindicators.un.org/unsd/trade/s_geneva2011/refdocs/RDs/Lithium-Ion%20Batteries%20(Gereffi%20-%20May%202010).pdf.

Lukic, S. M., Cao, J., Bansal, R. C., Rodriguez, F., & Emadi, A. (2008). Energy storage systems for automotive applications. *IEEE Transactions on Industrial Electronics*, *55*(6), 2258-2267. https://doi.org/10.1109/TIE.2008.918390.

Makino, M., Ogawa, N., Abe, Y., & Fujiwara, Y. (2003). Automotive air-conditioning electrically driven compressor (No. 2003-01-0734). SAE Technical Paper. https://doi.org/10.4271/2003-01-0734.

Marcos, D., Pino, F. J., Bordons, C., & Guerra, J. J. (2014). The development and validation of a thermal model for the cabin of a vehicle. *Applied Thermal Engineering*, *66*, 646-656. https://doi.org/10.1016/j.applthermaleng.2014.02.054.

MathWorks, (2018a). Simulink® User Guide 2018b.

MathWorks, (2018b). Simscape™ User Guide 2018b.

MathWorks, (2018c). Simscape™ Reference 2018b.

McEnaney, R. P., Boewe, D. E., Yin, J. M., Park, Y. C., Bullard, C. W., & Hrnjak, P. S. (1998). Experimental comparison of mobile AC systems when operated with transcritical CO_2 versus conventional R134a. *Proceedings of the Seventh International Refrigeration Conference at Purdue University*, Paper 402. http://docs.lib.purdue.edu/iracc/402.

McQuiston, F. C., Parker, J. D., & Spitler, J. D. (2004). Heating, ventilating, and air conditioning: analysis and design. John Wiley & Sons.

Modelica Association. Modelica. https://www.modelica.org/. (accessed November 3rd, 2019).

Monforte, R., & Caretto, L. (2009). *Safety Issues in the Application of a Flammable Refrigerant Gas in MAC Systems: The OEM Perspective [Revised July, 2009]* (No. 2009-01-0541). SAE Technical Paper. https://doi.org/10.4271/2009-01-0541.

Murphy, W. E., & Goldschmidt, V. W. (1985). Cyclic characteristics of a typical residential air conditioner-modeling of start-up transients. *ASHRAE transactions*, *91*(2A), 427-437. https://pascal-francis.inist.fr/vibad/index.php?action=getRecordDetail&idt=8106966.

Olesen, B. W., & Parsons, K. C. (2002). Introduction to thermal comfort standards and to the proposed new version of EN ISO 7730. *Energy and Buildings*, *34*(6), 537-548. https://doi.org/10.1016/S0378-7788(02)00004-X.

Ozeki, Y., Takabayashi, T., & Tanabe, S. I. (2005). Effects of spectral properties of glass on the thermal comfort of car occupants. *Elsevier Ergonomics Book Series*, *3*, 289-297. https://doi.org/10.1016/S1572-347X(05)80047-3.

Park, Y.-G. & Jacobi, A.M. (2009). Air-side heat transfer and friction correlations for flat-tube

louver-fin heat exchangers. *Journal of Heat Transfer*, *131*(*2*), Article 02180. https://doi.org/10.1115/1.3000609.

Pasaoglu, G., Fiorello, D., Martino, A., Scarcella, G., Alemanno, A., Zubaryeva, A., & Thiel, C. (2012). Driving and parking patterns of European car drivers-a mobility survey. *Luxembourg: European Commission Joint Research Centre*. http://www.eurosfaire.prd.fr/7pc/documents/1373985744_driving_and_parking_patterns___final_online.pdf.

Pesaran, A. A. (2001). Battery thermal management in EV and HEVs: issues and solutions. *Battery Man*, *43*(5), 34-49.

Pesaran, A. A. (2002). Battery thermal models for hybrid vehicle simulations. *Journal of Power Sources*, *110*(2), 377-382. https://doi.org/10.1016/S0378-7753(02)00200-8.

Pesaran, A. A., Santhanagopalan, S., & Kim, G. H. (2013). *Addressing the impact of temperature extremes on large format li-ion batteries for vehicle applications (presentation)* (No. NREL/PR-5400-58145). National Renewable Energy Lab.(NREL), Golden, CO, US. https://www.nrel.gov/docs/fy13osti/58145.pdf.

Petter, N., Filippo, D., Havard, R., & Arne, B. (2004). Measurements and experience on semi-hermetic CO_2 compressors. In *5th International Conference on Compressors and Coolants*, IIR, Slovak Republic.

Pettersen, J. (1994). An efficient new automobile air-conditioning system based on CO_2 vapor compression. *ASHRAE Transactions*, *100*(2), 657-665.

Peuker, S., & Hrnjak, P. (2008). Refrigerant mass and oil migration during start-up transient. *International Refrigeration and Air Conditioning Conference*, Paper 994. http://docs.lib.purdue.edu/iracc/994.

Pfafferott, T., & Schmitz, G. (2004). Modelling and transient simulation of CO_2-refrigeration systems with Modelica. *International Journal of Refrigeration*, *27*(1), 42-52. https://doi.org/10.1016/S0140-7007(03)00098-7

Qi, Z. (2014). Advances on air conditioning and heat pump system in electric vehicles - A review. *Renewable and Sustainable Energy Reviews*, *38*, 754–764. https://doi.org/10.1016/j.rser.2014.07.038.

Qi, Z., Chen, J., Chen, Z., Hu, W., & He, B. (2007). Experimental study of an auto-controlled automobile air conditioning system with an externally-controlled variable displacement compressor. *Applied Thermal Engineering*, *27*, 927–933. https://doi.org/10.1016/j.applthermaleng.2006.08.017.

Qiao, H. (2014). *Transient modeling of two-stage and variable refrigerant flow vapor*

compression systems with frosting and defrosting [Doctoral dissertation, University of Maryland]. https://doi.org/10.13016/M24892.

Qiao, H., Aute, V., & Radermacher, R. (2012). Comparison of equation-based and non-equation-based approaches for transient modeling of a vapor compression cycle. *International Refrigeration and Air Conditioning Conference*, Paper 1205. https://docs.lib.purdue.edu/iracc/1205.

Radziemska, E., & Lewandowski, W. M. (2001). Heat transfer by natural convection from an isothermal downward-facing round plate in unlimited space. *Applied Energy*, *68*(4), 347-366. https://doi.org/10.1016/S0306-2619(00)00061-1.

Rajendran, H., & Pate, M. (1986). A computer model of the start-up transients in a vapor compression refrigeration system. *International Refrigeration and Air Conditioning Conference*, Paper 17. https://docs.lib.purdue.edu/iracc/17.

Rich, B. R. (1953). An investigation of heat transfer from an inclined flat plate in free convection. *Transection of ASME*, *75*, 489-499.

Sanaye, S., & Dehghandokht, M. (2011). Thermal modeling for predication of automobile cabin air temperature. *International Journal of Automotive Engineering*, *1*(3), 152-164. http://ijae.iust.ac.ir/article-1-21-en.html.

Sarkar, J., Bhattacharyya, S., & Gopal, M. R. (2004). Optimization of a transcritical CO_2 heat pump cycle for simultaneous cooling and heating applications. *International Journal of Refrigeration*, *27*(8), 830-838. https://doi.org/10.1016/j.ijrefrig.2004.03.006.

Sasaki, T., Ukyo, Y., & Novák, P. (2013). Memory effect in a lithium-ion battery. *Nature Materials*, *12*(6), 569-575. https://doi.org/10.1038/nmat3623.

Seybold, L., Styles, B., Lazaridis, I., & Kneusels, H. J. (2014). Vehicle hot surface ignition and mitigation measures of R-1234yf refrigerant for MAC systems. *SAE International Journal of Transportation Safety*, *2*(2), 219-239.

Singh, S., & Abbassi, H. (2018). 1D/3D transient HVAC thermal modeling of an off-highway machinery cabin using CFD-ANN hybrid method. *Applied Thermal Engineering*, *135*, 406-417. https://doi.org/10.1016/j.applthermaleng.2018.02.054.

Song, X., Lu, D., Lei, Q., Cai, Y., Wang, D., Shi, J., & Chen, J. (2021). Experimental study on heating performance of a CO_2 heat pump system for an electric bus, *Applied Thermal Engineering*, *190*, Article 116789. https://doi.org/10.1016/j.applthermaleng.2021.116789.

Tarascon, J. M., & Armand, M. (2001). Issues and challenges facing rechargeable lithium batteries. *Nature*, *414*(6861), 359-367.

Torregrosa-Jaime, B., Bjurling, F., Corberán, J. M., Di Sciullo, F., & Payá, J. (2015). Transient thermal model of a vehicle's cabin validated under variable ambient conditions. *Applied Thermal Engineering*, *75*, 45-53. https://doi.org/10.1016/j.applthermaleng.2014.05.074.

Tortora, G. J., & Derrickson, B. H. (2018). *Principles of anatomy and physiology*. John Wiley & Sons.

Trčka, M., & Hensen, J. L. (2010). Overview of HVAC system simulation. *Automation in Construction*, *19*(2), 93-99. https://doi.org/10.1016/j.autcon.2009.11.019.

Wang, Y., Dong, J., Jia, S., & Huang, L. (2021). Experimental comparison of R744 and R134a heat pump systems for electric vehicle application. *International Journal of Refrigeration*, *121*, 10-22. https://doi.org/10.1016/j.ijrefrig.2020.10.026.

Wang, D., Yu, B., Hu, J., Chen, L., Shi, J., & Chen, J. (2018a). Heating performance characteristics of CO_2 heat pump system for electrical vehicle in a cold climate. *International Journal of Refrigeration*, *85*, 27-41. https://doi.org/10.1016/j.ijrefrig.2017.09.009.

Wang, D., Yu, B., Li, W., Shi, J., & Chen, J. (2018b). Heating performance evaluation of a CO_2 heat pump system for an electrical vehicle at cold ambient temperatures. *Applied Thermal Engineering*, *142*, 656-664. https://doi.org/10.1016/j.applthermaleng.2018.07.062.

Wang, D., Zhang, Z., Yu, B., Wang, X., Shi, J., & Chen, J. (2019). Experimental research on charge determination and accumulator behavior in trans-critical CO_2 mobile air-conditioning system. *Energy*, *183*, 106–115. https://doi.org/10.1016/j.energy.2019.06.116.

Wetter, M., & Haugstetter, C. (2006). Modelica versus TRNSYS–A comparison between an equation-based and a procedural modeling language for building energy simulation.*Proceedings of SimBuild*, *2*(1), 262-269. http://www.ibpsa-usa.org/index.php/ibpusa/article/view/220.

Winkler, J. M. (2009). *Development of a component based simulation tool for the steady state and transient analysis of vapor compression systems* [Doctoral dissertation, University of Maryland]. http://hdl.handle.net/1903/9493.

Wu, J., Jiang, F., Song, H., Liu, C., & Lu, B. (2017). Analysis and validation of transient thermal model for automobile cabin. *Applied Thermal Engineering*, *122*, 91-102. https://doi.org/10.1016/j.applthermaleng.2017.03.084.

Yin, J. M., Bullard, C. W., & Hrnjak, P. S. (2001). R-744 gas cooler model development and

validation. *International Journal of Refrigeration*, *24*, 692–701. https://doi.org/10.1016/S0140-7007(00)00082-7.

Yun, R., Hwang, Y., & Radermacher, R. (2007). Convective gas cooling heat transfer and pressure drop characteristics of supercritical CO_2/oil mixture in a minichannel tube. *International Journal of Heat and Mass Transfer*, *50*(23-24), 4796-4804. https://doi.org/10.1016/j.ijheatmasstransfer.2007.03.018.

Zhang, Z., Wang, J., Feng, X., Chang, L., Chen, Y., & Wang, X. (2018). The solutions to electric vehicle air conditioning systems: A review. *Renewable and Sustainable Energy Reviews*, *91*, 443-463. https://doi.org/10.1016/j.rser.2018.04.005.

Appendix A

Table A.1. Experimental conditions for steady-state operations (Ko et al., 2020).

Case	A	B	C	D	E	F	G	H	I	J
1	29.9	126.6	8.29	75.0	20.4	90.8	3.92	295.8	72	225
2	30.0	137.3	8.32	76.6	20.4	100.0	3.94	294.4	78	237
3	29.8	118.4	8.36	68.4	20.4	134.9	4.45	295.0	60	219
4	29.8	128.5	8.43	70.0	20.4	147.3	4.44	286.7	62	179
5	29.8	137.2	10.0	86.0	20.4	152.9	4.45	270.9	60	127
6	20.1	83.8	7.83	65.4	15.6	253.6	4.32	283.8	68	245
7	20.1	91.1	7.85	66.3	15.6	273.7	4.32	283.1	74	263
8	20.1	89.3	7.92	66.4	15.6	270.9	4.32	272.2	68	176
9	20.1	97.2	7.95	66.8	15.7	289.4	4.31	271.9	74	192
10	20.1	103.7	8.29	69.1	15.6	318.7	4.30	247.9	70	142
11	24.9	67.6	10.0	80.5	20.5	310.7	4.85	269.2	68	159
12	24.9	64.2	10.1	80.3	20.5	296.8	4.87	266.6	64	146
13	24.9	69.0	10.1	82.2	20.5	318.0	4.85	263.9	68	150
14	24.9	65.1	10.4	83.8	20.5	302.7	4.85	256.9	62	126
15	29.9	126.6	8.29	75.0	20.5	315.7	4.85	256.3	64	129

A: Water temperature at the gas cooler inlet, ^{o}C.

B: Water flow rate at the gas cooler, L h^{-1}.

C: Refrigerant pressure at the gas cooler inlet, MPa.

D: The refrigerant temperature at the gas cooler inlet, ^{o}C.

E: Water temperature at the evaporator inlet, ^{o}C.

F: Water flow rate at the evaporator, L h^{-1}.

G: Refrigerant pressure at the evaporator inlet, MPa.

H: Refrigerant enthalpy at the evaporator inlet, kJ kg^{-1}.

I: Compressor rotational speed, rev s^{-1}.

J: EEV opening step.

Table A.2. Experimental results in steady-state operations (Ko et al., 2020).

Case	A	B	C	D	E	F	G	H	I	J	K	L	M	N
1	32.5	2.31	45.0	2.21	5.4	3.77	1.73	4.9	1.63	2.5	45.4	0.63	2.60	3.53
2	32.3	2.52	45.1	2.41	5.7	3.76	1.88	5.0	1.78	2.9	48.5	0.69	2.59	3.51
3	32.5	2.16	45.0	2.07	11.9	4.32	1.72	9.9	1.63	3.5	45.2	0.49	3.33	4.22
4	31.3	2.35	45.0	2.26	12.1	4.44	1.88	9.9	1.79	3.8	46.3	0.52	3.47	4.38
5	29.5	2.54	45.1	2.42	11.9	4.33	1.95	10.0	1.85	3.5	43.6	0.65	2.86	3.74
6	29.3	2.52	45.0	2.42	10.7	4.16	2.04	9.0	1.94	3.8	48.9	0.52	3.75	4.68
7	29.2	2.73	45.0	2.63	10.3	4.14	2.20	9.0	2.10	3.6	52.5	0.57	3.67	4.82
8	27.0	2.68	45.0	2.58	10.6	4.16	2.19	9.0	2.08	3.8	48.7	0.52	3.96	4.91
9	27.0	2.90	45.0	2.90	8.7	4.12	2.35	9.1	2.24	3.1	52.6	0.58	3.86	5.00
10	20.4	3.12	45.0	3.00	9.1	4.14	2.56	9.0	2.44	2.4	50.2	0.58	4.19	5.16
11	29.2	3.11	63.0	2.99	14.6	4.68	2.46	13.9	2.36	2.8	55.4	0.71	3.33	4.21
12	28.5	2.96	63.0	2.83	14.3	4.68	2.35	13.9	2.25	2.6	52.4	0.67	3.34	4.21
13	27.6	3.16	62.9	3.04	14.7	4.64	2.51	14.0	2.41	3.2	54.4	0.72	3.34	4.22
14	25.6	3.01	63.1	2.88	14.5	4.68	2.40	13.9	2.30	2.7	50.3	0.69	3.35	4.19
15	25.5	3.13	62.9	2.99	14.6	4.68	2.48	14.0	2.38	2.0	51.8	0.72	3.30	4.15

A: Refrigerant temperature at the gas cooler outlet, ^{o}C.

B: Heat transfer rate at the refrigerant side of the gas cooler, kW.

C: Water temperature at the gas cooler outlet, ^{o}C.

D: Heat transfer rate at the water-side of the gas cooler, kW.

E: The refrigerant temperature at the evaporator outlet, ^{o}C.

F: The refrigerant pressure at the evaporator outlet, MPa.

G: Heat transfer rate at the refrigerant side of the evaporator, kW.

H: Water temperature at the evaporator outlet, ^{o}C.

I: Heat transfer rate at the water-side of the evaporator, kW.

J: Degree of suction superheating, ^{o}C.

K: Refrigerant mass flow rate, kg h^{-1}.

L: Compressor power, kW.

M: COP for cooling.

N: COP for heating.

Table A.3. Simulation inputs for steady-state operations (Ko et al., 2020).

Case	A	B	C	D	E	F	G	H
1	32.0	8.3	32.0	4.5	4.5	11.0	4.0	72
2	32.0	11.0	32.0	4.5	4.5	11.0	4.0	78
3	31.0	7.8	32.0	9.5	4.5	11.0	2.0	60
4	31.1	7.9	32.0	9.5	4.5	11.0	3.5	62
5	29.2	8.3	32.0	9.5	4.5	11.0	4.0	60
6	29.0	8.3	32.0	8.3	4.5	11.0	2.5	68
7	28.5	8.2	32.0	8.3	4.5	11.0	4.0	74
8	26.0	8.9	32.0	8.3	4.5	11.0	4.0	68
9	26.0	8.9	32.0	8.3	4.5	11.0	3.5	74
10	20.0	9.0	26.0	8.0	4.5	11.0	3.5	70
11	28.0	10.0	30.0	13.0	4.8	13.0	3.5	68
12	27.0	10.5	30.0	13.0	4.8	13.0	4.0	64
13	27.0	10.4	30.0	13.0	4.8	13.0	3.5	68
14	24.0	12.3	30.0	12.5	4.8	13.0	4.0	62
15	24.0	12.3	30.0	12.5	4.8	13.0	4.0	64

A: Thermal reservoir temperature at the gas cooler, ^{o}C.

B: Initial pressure of the refrigerant at the high-pressure side, MPa.

C: Initial temperature of the refrigerant at the high-pressure side, ^{o}C.

D: Thermal reservoir temperature at the evaporator, ^{o}C.

E: Initial pressure of the refrigerant at the low-pressure side, MPa.

F: Initial temperature of the refrigerant at the low-pressure side, ^{o}C.

G: The temperature difference between the suction and the expansion valve outlet, ^{o}C.

H: Compressor rotational speed, rev s^{-1}.

Table A.4. Simulation results in steady-state conditions (Ko et al., 2020).

Case	A	B	C	D	E	F	G
1	45.8	4.9	1.62	2.22	0.59	2.75	3.76
2	49.1	4.9	1.80	2.46	0.66	2.73	3.73
3	47.7	2.9	1.66	2.16	0.50	3.32	4.32
4	47.0	4.9	1.71	2.20	0.49	3.49	4.49
5	44.0	4.0	1.76	2.38	0.61	2.89	3.90
6	50.6	3.5	1.92	2.42	0.50	3.84	4.84
7	52.3	5.7	2.06	2.62	0.56	3.68	4.68
8	48.3	4.8	2.03	2.53	0.50	4.06	5.06
9	52.8	4.4	2.22	2.77	0.55	4.04	5.04
10	49.4	3.5	2.35	2.90	0.56	4.20	5.18
11	55.6	3.6	2.30	2.99	0.69	3.33	4.33
12	51.8	4.0	2.19	2.84	0.65	3.37	4.37
13	55.5	3.5	2.34	3.03	0.69	3.39	4.39
14	49.4	4.0	2.19	2.85	0.65	3.37	4.38
15	50.7	4.1	2.26	2.94	0.68	3.32	4.32

A: Refrigerant mass flow rate, kg h^{-1}.

B: Degree of suction superheating, ^{o}C.

C: Heat transfer rate at the evaporator, kW.

D: Heat transfer rate at the gas cooler, kW.

E: Compressor power, kW.

F: COP for cooling.

G: COP for heating.

Appendix B

Figure B.1 provides the influence of moisture for the moist-air j-factor evaluation as an example. In the graph, j_a represents the j-factor evaluated based on properties of the dry air in the given moist-air flowing condition and j_{ma} indicates the j-factor calculated based on properties of the moist-air mixture. Both were evaluated using the model of Park and Jacobi (2009), which was used in the present study. The result shows that the j-factor value is underestimated if the moisture properties are not considered. The degree of underestimation increases with an increase in the contained moisture amount, while the temperature effect is not significant. The maximum value of the underestimation, 17.6%, is observed at the temperature of 5 °C and RH of 99.2% in this investigation. Besides, the underestimation degree is less than 10% when the RH is below 60%. The original article (Park and Jacobi, 2009) provides the prediction performance of the used j-factor model (Park and Jacobi, 2009). Considering that, the degree of underestimation, which is caused by the disregard of the moisture properties, lies within the range of the prediction confidence of the original model. The inconsideration of moisture contribution affects the thermophysical properties of a moist-air mixture, then this results in an underestimation of the j-factor value for the moist-air flow, but the effect is not significant, as much as to affect the present investigations.

Figure B.1. Influence of moisture on Colburn j-factor evaluation in moist-air flow (Ko et al., 2021b).

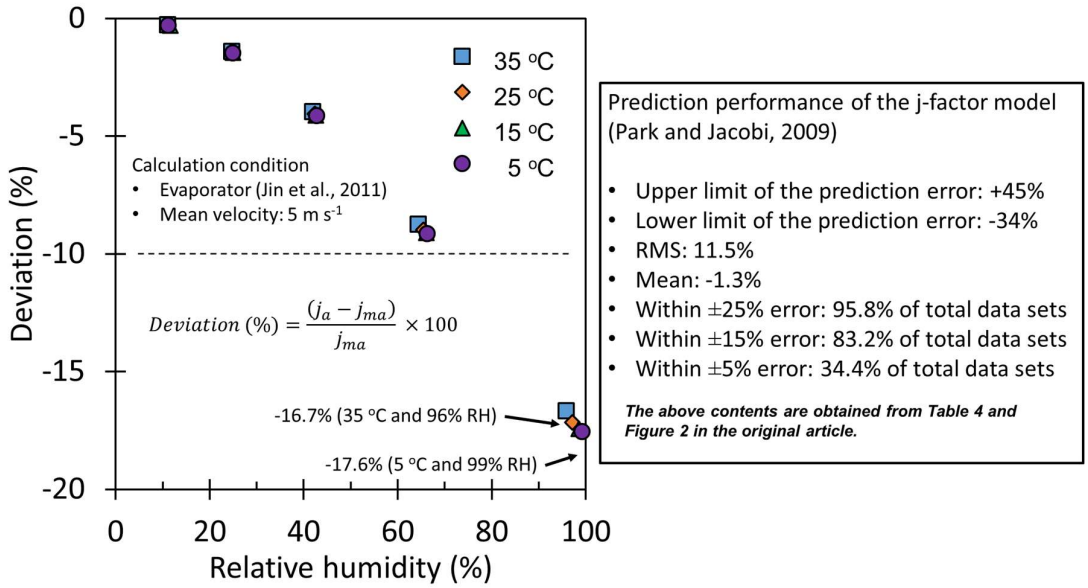

Appendix C

Heat transfer rate through each structure was considered with the following assumptions (Ko et al., 2021b):

1. The thermophysical properties of each structure are uniform in a plane.
2. The heat transfer through each structure is one-dimensional in the normal direction of each plane.
3. The roof panel is a horizontal plate and an opaque medium.
4. When the vehicle speed is larger than 0 m s^{-1}, forced convection heat transfer of the outdoor air is considered on the vehicle exterior surface.
5. When the vehicle is 0 m s^{-1}, free convection heat transfer of the outdoor air is considered on the vehicle's exterior surface.
6. When the AC is on, the cabin airflow is treated as a fully developed turbulent flow, in this case, forced convection heat transfer of the cabin air is considered.
7. When the AC is off, the cabin airflow is treated as a fully developed laminar flow, in this case, free convection heat transfer of the cabin air is considered.
8. Heat transfer from the vehicle trunk and floor is neglected since the thermal insulation is installed.

Figure C.1 shows a schematic of heat transfer throughout the roof. The heat balance equations in each object are as follows:

Heat balance at the outer surface of the roof panel is as follows:

$$\dot{Q}_{conv.od} + \dot{Q}_{emi.out} = \dot{Q}_{abs} + \dot{Q}_{cond.rp.outh}, \quad \text{(C1)}$$

$$\dot{Q}_{conv.od} = h_{od} A_{rp} \left(T_{od.ma} - T_{rp.out}\right), \quad \text{(C2)}$$

$$\dot{Q}_{emi.out} = \varepsilon^*_{rp.out} A_{rp} \sigma_{SB} \left(T^4_{rp.out} - T^4_{sky}\right), \quad \text{(C3)}$$

$$\dot{Q}_{abs.rp} = G_s \alpha^*_{rp} A_{rp}, \quad \text{(C4)}$$

$$\dot{Q}_{cond.rp.out} = \frac{k_{rp}A_{rp}(T_{rp.out}-T_{rp.mass})}{\left(\frac{th_{rp}}{2}\right)}, \quad \text{(C5)}$$

The subscripts $conv$, emi, $cond$, abs, out, $outh$, rp, and sky represent the emission, the conduction, the solar irradiation absorbed, the outer surface of an object, the outer half of an object, the roof panel, and the sky, respectively. G_s, ε^*, α^*, σ_{SB}, and th indicate the solar irradiance, the emissivity, the absorptivity, the Stefan-Boltzmann constant, and the thickness, respectively.

Heat balance in the roof panel is as follows:

$$\left(V\rho C_P \frac{dT}{dt}\right)_{rp} = \dot{Q}_{cond.rp.outh} + \dot{Q}_{cond.rp.inh}, \quad \text{(C6)}$$

where the subscript, inh, represents the inner half of an object.

$$\dot{Q}_{cond.rp.inh} = \frac{k_{rp}A_{rp}(T_{rp.mass}-T_{rp.in})}{\left(\frac{th_{rp}}{2}\right)}, \quad \text{(C7)}$$

Heat balance at the outer surface of the insulation (i.e., at the inner surface of the roof panel) is as follows:

$$\dot{Q}_{cond.ins.outh} = \dot{Q}_{cond.rp.inh}, \quad \text{(C8)}$$

where the subscript, ins, denotes the insulation.

Heat balance in the insulation layer is as follows:

$$\left(V\rho C_P \frac{dT}{dt}\right)_{ins} = \dot{Q}_{cond.ins.outh} + \dot{Q}_{cond.ins.inh}, \quad \text{(C9)}$$

$$\dot{Q}_{cond.ins.outh} = \frac{k_{ins}A_{ins}(T_{ins.out}-T_{ins.mass})}{\left(\frac{th_{ins}}{2}\right)}, \quad \text{(C10)}$$

$$\dot{Q}_{cond.ins.inh} = \frac{k_{ins}A_{ins}(T_{ins.mass} - T_{ins.in})}{\left(\frac{th_{ins}}{2}\right)}. \quad \text{(C11)}$$

Heat balance at the outer surface of the ceiling (i.e., at the inner surface of the insulation) is as follows:

$$\dot{Q}_{cond.ins.inh} = \dot{Q}_{cond.ce.outh}, \quad \text{(C12)}$$

where the subscript, ce, denotes the ceiling.

Heat balance in the ceiling material is as follows:

$$\left(V\rho C_P \frac{dT}{dt}\right)_{ce} = \dot{Q}_{cond.ce.outh} + \dot{Q}_{cond.ce.inh}, \quad \text{(C13)}$$

$$\dot{Q}_{cond.ce.outh} = \frac{k_{ce}A_{ce}(T_{ce.out} - T_{ce.mass})}{\left(\frac{th_{ce}}{2}\right)}, \quad \text{(C14)}$$

$$\dot{Q}_{cond.ce.inh} = \frac{k_{ce}A_{ce}(T_{ce.mass} - T_{ce.in})}{\left(\frac{th_{ce}}{2}\right)}, \quad \text{(C15)}$$

where the subscript, in, denotes the inner surface of an object.

Heat balance at the inner surface of the ceiling is as follows:

$$\dot{Q}_{cond.ce.inh} = \dot{Q}_{conv.cabin}, \quad \text{(C16)}$$

$$\dot{Q}_{conv.cabin} = h_{ce}A_{ce}(T_{ce.in} - T_{cabin.ma}), \quad \text{(C17)}$$

Figure C.1. Heat transfer through the roof (Ko et al., 2021b).

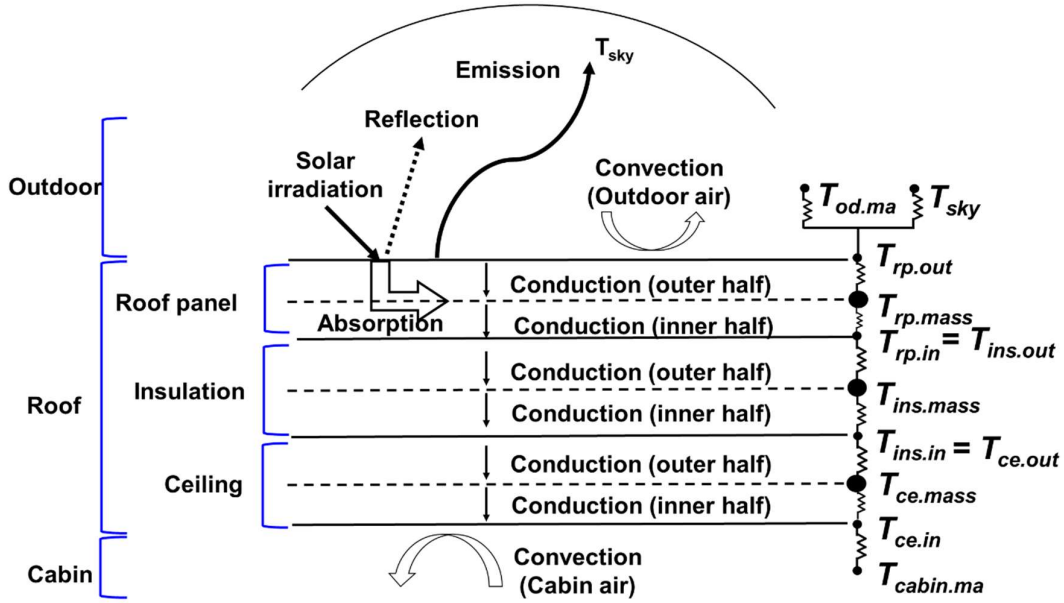

Figure C.2 shows a schematic of heat transfer in the window. Here, the windows represent all the windows in a vehicle such as a windshield, side windows, and rear window. The heat transfer through a window is treated such as a roof with a single layer, the material property difference only exists. So, the heat balance equations do not repeat herein. On the other hand, the transmitted irradiation through the windows provides a dominant effect on the cabin temperature by heating the interior structures so this effect is provided as follows.

Figure C.2. Heat transfer through a window (Ko et al., 2021b).

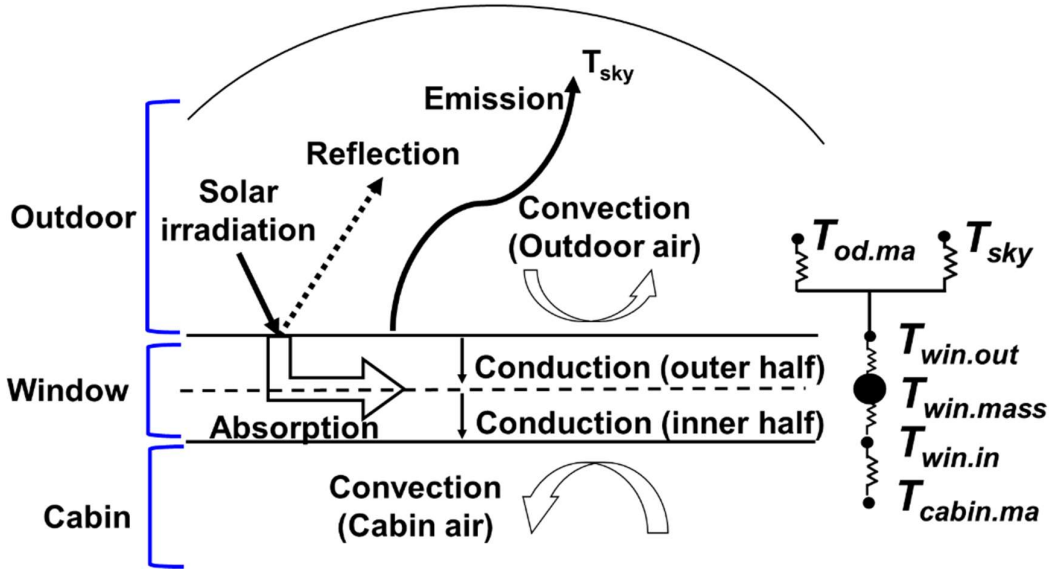

Figure C.3 shows the heat transfer between the body and cabin air. The transmitted irradiation through the windows provides a dominant effect on the cabin temperature by heating the interior structures. Part of the transmitted irradiation is absorbed into the vehicle body then, the body rejects this absorbed heat to the cabin air.

Figure C.3. Heat transfer between the body and cabin air (Ko et al., 2021b).

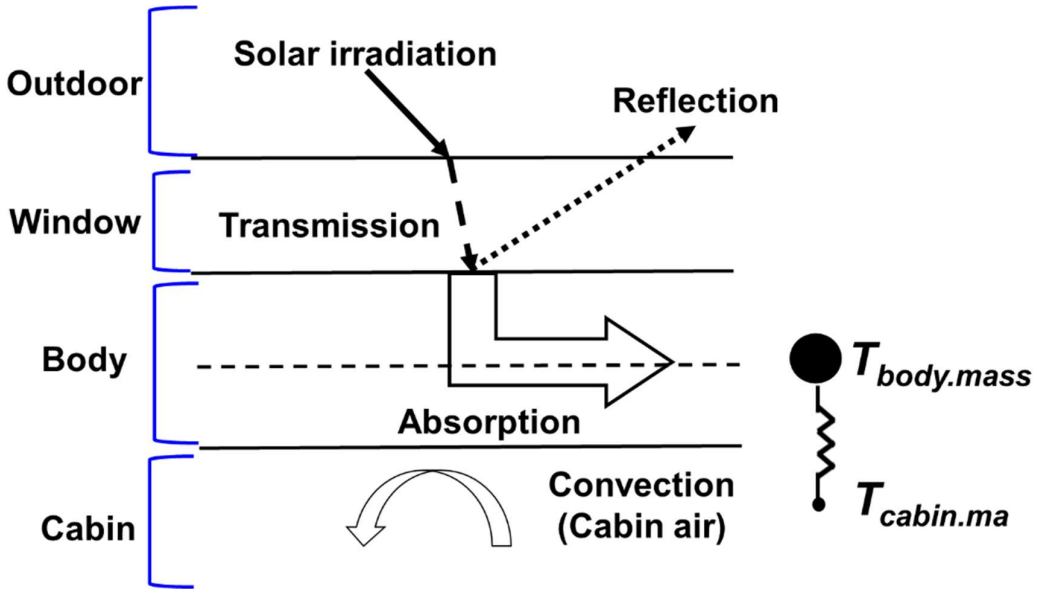

Thermal modeling of the vehicle body was conducted with the following assumptions (Ko et al., 2021b):

1. The transmitted irradiation through all windows is absorbed into the body or is reflected from the body.
2. The reflected irradiation does not affect the cabin thermal load, and it is rejected to the outdoor.
3. Concerning the heat transfer rate calculation, the body is treated as a vertical plate with a given equivalent heat transfer area.

The heat balance equation is given as follows:

$$\left(V\rho C_P \frac{dT}{dt}\right)_{body} = \alpha^*_{body} \sum_{win}[A(G_s\tau)] + \dot{Q}_{conv.body}, \qquad \text{(C18)}$$

where τ represents transmissivity. The convection heat transfer rate of cabin air ($\dot{Q}_{conv.body}$) is calculated as follows:

$$\dot{Q}_{conv.body} = h_{body} A_{body} \left(T_{body.mass} - T_{cabin.ma}\right). \quad \text{(C19)}$$

Correlations used for the Nusselt number calculation are tabulated in Table C.1. The average Nusselt number for free convection in an inclined plane is calculated using vertical plate correlation (Churchill & Chu, 1975), but the gravitational acceleration (g) is replaced by $g\cos\theta$ in computing the Rayleigh number (Rich, 1953).

Table C.1. Correlations for average Nusselt number calculations (Ko et al., 2021b).

Reference	**Applicable condition**
Incropera et al. (2007)	Forced convection in a flat plate
Lloyd and Moran (1974)	Free convection in a horizontal plane for the upper surface of a hot plate
Lloyd and Moran (1974)	Free convection in a horizontal plane for the lower surface of a cold plate
Radziemska and Lewandowski (2001)	Free convection in a horizontal plane for the lower surface of a hot plate or the upper surface of a cold plate
Churchill and Chu (1975)	Free convection in a vertical plate